

https://dspace.org/

Searches for dark matter through new collider topologies

van der Schyf, Hannah

2023
https://hdl.handle.net/10539/35728

Downloaded from a DSpace repository. https://dspace.org/

University of the Witwatersrand, Johannesburg
Faculty of Science
School of Physics

Searches for dark matter through new collider topologies

MSc Dissertation

Hannah van der Schyf Student number: 1586749
Supervisor: Prof. Deepak Kar

31 January 2023



UNIVERSITY OF THE
WITWATERSRAND,
JOHANNESBURG

Declaration

I, Hannah van der Schyf (Student number: 1586749) am a registered student for the degree of Master of science (Physics) in the academic year 2022. I hereby declare the following:

- I am aware that plagiarism (the use of someone else's work without their permission and/or without acknowledging the original source) is wrong.

- I confirm that ALL the work submitted for assessment for the above course is my own unaided work except where I have explicitly indicated otherwise.

- I have followed the required conventions in referencing the thoughts and ideas of others.

- I understand that the University of the Witwatersrand may take disciplinary action against me if there is a belief that this in not my own unaided work or that I have failed to acknowledge the source of the ideas or words in my writing.



Hannah van der Schyf

31-01-2023

Abstract

This dissertation explores dark matter searches through new collider topologies using jets. A exploratory study, conducted in 2021, of dark photons in a search for dark matter is presented. A dark photon may be detected through its kinetic mixing with the classical photon, which then couples weakly to electrically charged particles, allowing a non-gravitational window into the detection of dark matter. We will be considering the hypothetical Maverick top quark, in Ref [1], decaying to a Standard Model (SM) top quark and dark photon. The dark photon will decay exclusively to a lepton pair, for a dark photon mass up to 200 MeV the decay is completely to an electron and positron pair. We have focused on the hadronic decay of the top quark which gives a final state consisting of a heavy top quark jet. The search is for a large radius jet in the mass range of the top quark and a small radius jet close to the electron. We show that for a set of kinematic selections, almost all background can be eliminated, leaving enough signal events up to top partner mass of about 3.5 TeV for the search to be viable at the LHC Run 2. As well, a search is presented, conducted in 2022, for semi-visible jets arising from dark matter, using Run 2 data recorded with the ATLAS detector at the LHC with a center-of-mass energy of 13 TeV. For this search the hidden sector is hypothesized to couple to the SM via a heavy leptophobic Z' mediator by a resonant production $q\bar{q} \to Z' \to \chi\chi$. Semi-visible jets present an unusual topology, where the visible states in the shower are SM hadrons and the strongly coupled hidden sector containing dark quarks resulting in dark hadrons. This gives a final state consisting of a jet aligned with missing transverse energy due a mixture of stable, invisible dark hadrons and visible hadrons from an unstable subset of dark hadrons that promptly decay to SM particles. The resonant production and decay of such a mediator will result in a dijet system of semi visible jets, a signature ignored by most dark matter searches. Finally a brief project investigating track reconstruction using quantum computing for LUXE is considered. The LUXE experiment is a new experiment in planning at DESY Hamburg which will investigate the non-perturbative QED regime. A study is presented to explore the potential of quantum computers to reconstruct positron trajectories from detector energy deposits. The reconstruction problem is formulated with a quadratic unconstrained binary optimisation and is a simple example of only 7 qubits. The results from quantum simulations are discussed and compared to results from a real IBM quantum device.

Acknowledgements

First and foremost, many thanks to my supervisor Prof. Deepak Kar, as I could not have undertaken this journey without him. I have learnt a great deal from him and developed many skills that will always be convenient and advantageous to have in any path I take. I am also grateful to have had Sukanya Sinha, who has also provided me with a considerable amount of guidance and assistance throughout my studies.

I would also like to extend thanks to the IThemba LABS SA-CERN programme excellence scholarship. Providing me with funding and securing my studies, allowing for comfortable postgraduate student experience. As, without their support my MSc work would have been excruciatingly difficult.

Finally, and most importantly, I am deeply grateful for the love and patience of my friends and family. Without their unceasing support from an undergraduate level into my postgrad none of this would have been possible. The continuous support of my Mother and Uncle, as well as the unwavering confidence my Grandmother had in me, kept me motivated and inspired, especially through difficult times.

Publications

The work presented in this dissertation has also been presented and published in a peer-reviewed journal article and has been accepted in conference proceedings.

- du Plessis, K., Flores, M.M., Kar, D., Sinha, S. and van der Schyf, H., 2022. Hitting two BSM particles with one lepton-jet: search for a top partner decaying to a dark photon, resulting in a lepton-jet. https://scipost.org/SciPostPhys.13.2.018

- van der Schyf, Search for resonant production of strongly-coupled dark matter in proton-proton collisions, in The Proceedings of SAIP2022, the 66th Annual Conference of the South African Institute of Physics, edited by Prof. Aletta Prinsloo, (UJ), pp. 212 - 217. ISBN: 978-0-6397-4426-1. Available online at http://events.saip.org.za

Contents

Declaration i

Abstract iii

Acknowledgements v

Publications vi

List of Figures x

List of Tables xii

1 Introduction 1

1.1 The Standard Model of particle physics . . . 1

1.1.1 Fermions . . . 2

1.1.2 Bosons . . . 4

1.2 Gauge theories and the Standard Model . . . 6

1.3 The Standard Model's missing pieces . . . 12

1.4 Collider Objects and variables . . . 13

1.4.1 Luminosity . . . 14

1.4.2 Co-ordinates . . . 15

1.4.3 Transverse momentum and missing energy . . . 16

1.4.4 Invariant mass . . . 17

1.4.5 Jets . . . 17

1.5 Beyond the Standard Model: Dark matter . . . 18

1.5.1 Particle candidates . . . 21

1.5.2 Indirect detection . . . 22

1.5.3 Direct detection . . . 23

1.5.4 Collider searches . . . 23

2 Dark matter searches through a dark photon and heavy-top quark partner 25

2.1 Dark photons . . . 25

2.1.1 Dark photon production modes . . . 26

2.1.2 Dark photon decays and detection . . . 30

2.2 Production and decay of the maverick top quark . . . 32

2.3 Signal Model . . . 34
2.3.1 Event Generation . . . 36
2.4 Analysis strategy . . . 37
2.4.1 Overview . . . 37
2.4.2 Substructure Variables . . . 38
2.4.3 Analysis of dark photon with the heavy-top quark decaying hadronically 42
2.5 Results . . . 46
2.6 Conclusion . . . 48

3 Dark Matter searches using semi-visible jets 49
3.1 QCD-like dark sector . . . 49
3.1.1 Semi-visible jets . . . 51
3.1.2 Hidden Valley models . . . 52
3.2 Signal model . . . 56
3.3 ATLAS Detector . . . 58
3.4 Analysis strategy . . . 58
3.4.1 Signal characteristics . . . 58
3.5 Background . . . 61
3.5.1 Substructure variables . . . 61
3.5.2 Kinematic variable distributions for signal against background . . . 67
3.6 Conclusion . . . 70

4 Track Reconstruction using Quantum computing for LUXE 71
4.1 Introduction . . . 71
4.2 Quantum Computing . . . 73
4.3 The building blocks of track candidates . . . 77
4.4 Quantum Computing for track selection . . . 78
4.5 Results . . . 80
4.6 Conclusion . . . 81

References 82

List of Figures

1.1 Standard model summary . . . 2
1.2 Fermion generation mass differences . . . 3
1.3 Colour charges . . . 3
1.4 Spontaneous symmetry breaking rod analogy . . . 7
1.5 Mexican hat potential . . . 9
1.6 General detector co-ordinate system . . . 15
1.7 Pseudorapidity values . . . 16
1.8 Bounds on generic thermal WIMP window . . . 22
2.1 Dark matter annihilation Feynman diagram . . . 26
2.2 Feynman diagrams showing dark photon emitted from an electron . . . 27
2.3 QED Bethe-Heitler Feynman diagram . . . 27
2.4 QED radiative Feynman diagram . . . 28
2.5 Annihilation dark photon production Feynman diagram . . . 28
2.6 Compton-like scattering Feynman diagram . . . 29
2.7 Neutral meson decay Feynman diagram . . . 29
2.8 Drell Yan dark photon production Feynman diagram . . . 30
2.9 Standard VLT production modes . . . 33
2.10 Representative Feynman diagrams for VLT decays . . . 33
2.11 Branching ratios of γ_d as a function of its mass M_{γ_d} . . . 34
2.12 Production and decay of VLT . . . 35
2.13 Dark photon signal topology . . . 36
2.14 Plot showing τ_{32} and τ_{21} for dark photon searches . . . 39
2.15 Plot showing ECF2 and ECF3 for dark photon searches . . . 40
2.16 Plot showing C_2 and D_2 for dark photon searches . . . 41
2.17 LHA substructure variable for dark photon searches . . . 42
2.18 Number of b-jets for dark photon searches . . . 42
2.19 ΔR between leading electron and the closest J_4 . . . 43
2.20 Mass distributions for lepton jet and top jet . . . 44
2.21 p_T distributions for lepton jet and top jet . . . 45

2.22 $\Delta\phi$ between the lepton jet and top jet and VLT invariant mass 45
2.23 m/p_T ratio and VLT reconstructed mass 46
2.24 Integrated luminosity as a function of VLT mass 47
3.1 Jet topology for different r_{inv} 50
3.2 Jet evolution with respect to r_{inv} and decay distance 56
3.3 Feynman diagram of the leading-order resonant production 56
3.4 Svj kinematic distributions 59
3.5 Anti-svj kinematic distributions 60
3.6 Invariant mass distributions 61
3.7 ECF1 distribution for svj and anti-svj 62
3.8 ECF2 and ECF3 distribution for svj and anti-svj 62
3.9 C_2 and D_2 distribution for svj and anti-svj 63
3.10 τ_1 and τ_2 distribution for svj and anti-svj 63
3.11 τ_3 and τ_{21} for svj 64
3.12 τ_{32} distribution for svj and anti-svj 64
3.13 E3 distribution for svj 65
3.14 sd_{12} and sd_{23} distributions for anti-svj 66
3.15 Q_W distribution for svj 67
3.16 Invariant mass distributions 67
3.17 MET and leading jet p_T and number of jets 68
3.18 MET and leading jet p_T normalised 69
3.19 Invariant mass distributions normalised 69
4.1 Non-linear Compton scattering and Breit-Wheeler pair production 71
4.2 Schematic layout of LUXE 72
4.3 Bit and qubit representations 73
4.4 Representation of the classical AND gate 74
4.5 Representation of the quantum CNOT gate 74
4.6 Quantum circuit example 76
4.7 Formation of doublets 77
4.8 Diagram of VQE algorithm 79
4.9 Circuit representation of RY and CZ gate 79
4.10 Simulation comparisons 80
4.11 Efficiency rate 81

List of Tables

1 Signal efficiency 46
2 12 fundamental Hidden Valley particles 53

1 Introduction

1.1 The Standard Model of particle physics

The study of particle physics is focused on our understanding of elementary particles and the means by which they interact. The Standard Model of particle physics describes the fundamental particles and their interactions, and has so far been highly consistent with experimental data. This sophisticated model gives a complex explanation of 17 fundamental particles in nature, from the vector (g, γ, W, Z) and scalar (H) bosons to the three generation fermions (quarks and leptons) [2].

The Standard Model was constructed in stages throughout the 20^{th} century, dating back to 1954. It began with C. N. Yang, S. Weinberg and R. Mills [3], who extended the concept of gauge theory for Abelian groups to non-Abelian groups to provide an explanation for strong interactions. In 1957 C. Wu demonstrated that parity was not conserved for weak interactions and in 1961 S.Glashow combined the electromagnetic force and weak nuclear force [4]. The SM also explains the existence of particles due to the Higgs mechanism, where by spontaneously broken symmetry associated with the scalar field, or Higgs field, results in the appearance of mass terms for certain gauge bosons and fermions. The Higgs mechanism was originally proposed by P. Higgs, R. Brout, F. Englert, G. S. Guralnik, C. R. Hagen, and T. W. B. Kibble in 1964 [5, 6, 7] and later incorporated into S. Glashow's electroweak interaction in 1967, giving it its modern form.

The different particles of the SM are summarised in Figure 1.1, in this model, matter is made up of two types of particles, fermions and bosons. Fermions contribute to the formation of matter as we know, and have half integer spin, obeying the principles of Fermi-Dirac statistics. Bosons contribute to the mediating forces which control the interactions between fermions, they have integer spin and obey the principles of Bose-Einstein statistics. It is also required in the theory that every particle have an associated anti-particle. These anti-particles have the opposite charge of their counter part but are identical in every other quantum property. There are some cases where a particle may be its own anti-particle, these are labeled as Majorana fermions.

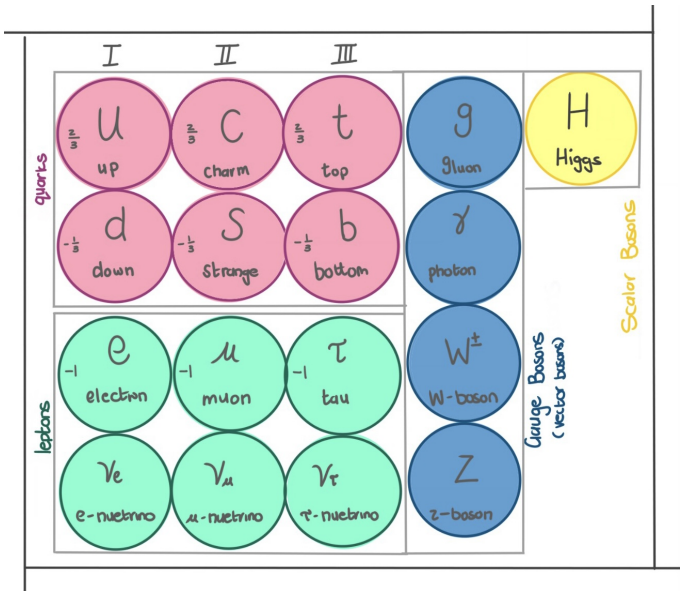


Figure 1.1: Summary of SM, the pink and turquoise circles show the fermions and represent the three generations of quarks and leptons. The blue circles represent the gauge boson where g is the gluon, γ is the photon and W and Z are the W and Z boson. The yellow circle is the scalar Higgs boson.

1.1.1 Fermions

Fermions are divided into three generations of quarks and leptons, where each generation has a mass significantly higher than the previous generation but other quantum properties remain the same. How these masses differ can be seen in Figure 1.2. As well, each generation consists of a pair of quarks and a pair of leptons, along with each particle's associated anti-particle. The pair of quarks in each generation are referred to as *up-type*, which has a positive electric charge, and *down-type*, which has a negative electric charge. This type description originates from the original naming convention of the first generation up and down quarks. The *up-type* quarks and their associated anti-quarks have an electric charge of $\frac{2}{3}$ and $-\frac{2}{3}$ respectively. Where as the *down-type* quarks and associated anti-quarks have an electric charge off $-\frac{1}{3}$ and $\frac{1}{3}$ respectively.

Quarks also possess another charge, termed colour charge, according to quantum chromodynamics (QCD). There are three types of colour charges, which every quark or anti-quark carries, red (r), green (g) and blue (b), which then have associated anti-colour charges, anti-red ($\bar{r}$), anti-green ($\bar{g}$) and anti-blue ($\bar{b}$), shown in Figure 1.3. Quarks cannot exist as isolated particles, due to the colour confinement effect [8], they combine and form hadrons which are colour neutral states.

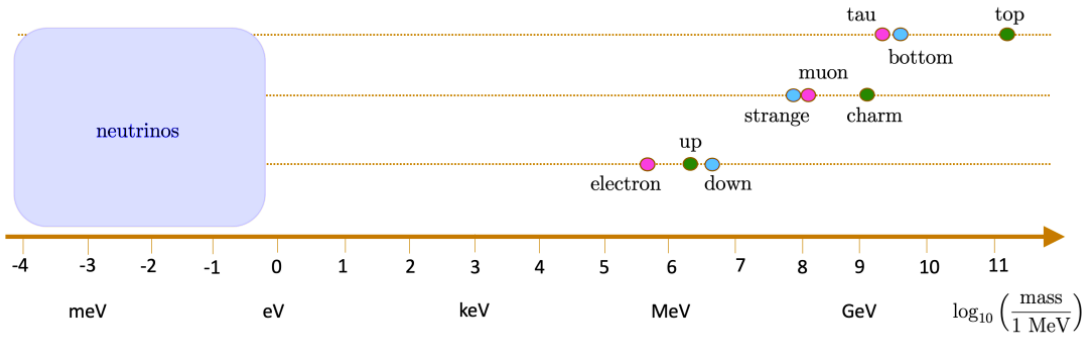


Figure 1.2: Figure showing the mass differences between generations for quarks and leptons.

There are two types of hadrons, baryons and mesons, and are classified depending on whether the hadron is formed of three quarks or a quark -anti-quark pair. The probability of particles coupling via strong interactions is orders of magnitudes larger than them coupling via weak interactions. However, the strong force has a restriction, which is approximately the size of a proton ($\sim 10^{-15}$m), resulting to colour confinement constraints.

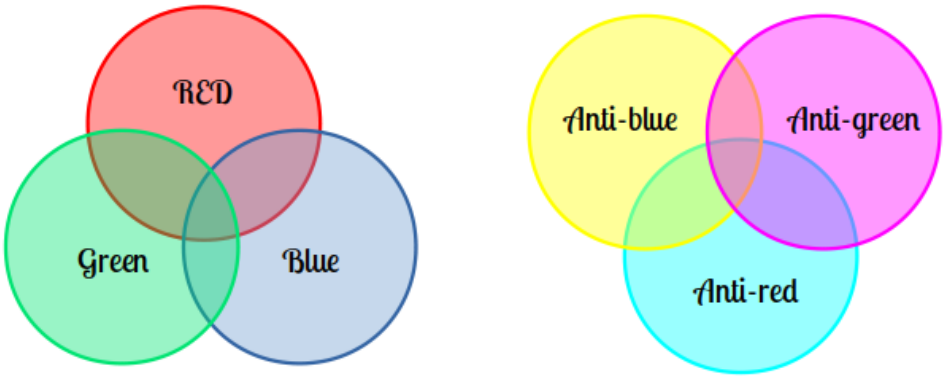


Figure 1.3: The quark colour charges, (red, green, blue) and anti-quark colour charges (anti-red, anti-green, anti-blue) which combine to be colourless.

The pair of leptons in each generation exist as charged leptons or anti-leptons carrying an electric charge of 1 or -1 respectively and a neutrino and anti-neutrino which are neutral under electromagnetism. Leptons also carry iso-spin, allowing them to interact with themselves as well as other particles via the electromagnetic (EM) and weak forces respectively. For charged leptons, as with the quarks, the masses increase with generation, however neutrinos are a more tricky subject. Traditionally the SM considers them to be massless, however experimentally they have been observed to have a non-zero, but minuscule mass [9] as we have observed neutrinos to oscillate.

We know they must have mass because of special relativity, as neutrinos can oscillate between different flavours. A neutrino created with a specific lepton flavour can later be measured to have a different flavour and if neutrinos were massless they would travel at the speed of light. However, if this were the case, from our reference frame, they would not have time to oscillate, thus we would not observe them oscillate, as such they must have mass. Fermions also have the property of being left or right-handed, referred to as the helicity, however, since fermions are massive we consider the chirality. The chirality of a particle is more conceptual, it is determined by how the particle transforms in a left or right-handed representation of the Poincaré group [10]. Chirality is related to helicity, however, for particles with mass, chirality and helicity must be distinguished. This is because massive particles do not travel at the speed of light, thus it is possible for an observer to be in a reference frame moving faster than the spinning particle. This results in the appearance of the particle moving backwards and the helicity will be reversed. Thus helicity can be thought of as "apparent" chirality, that is helicity is a constant motion but is not Lorentz invariant, where as chiralty is not a constant motion but is Lorentz invariant. The helicity is right-handed for $+1/2$ spin and left-handed for $-1/2$ spin. For the fermions it is convenient to define the helicity projectors as [11],

$$L_h \equiv \frac{1}{2}(1-\gamma^5) \qquad , \qquad R_h \equiv \frac{1}{2}(1+\gamma^5) \tag{1.1}$$

where, $\gamma^5 = i\gamma^0\gamma^1\gamma^2\gamma^3$ is the fifth Dirac matrix, which is generally used to project a Dirac field to its left/right-handed components, where $\gamma^\mu = \gamma^0, \gamma^1, \gamma^2, \gamma^3$ are the four contravariant gamma matrices. It is interesting to note that while all other fermions have been observed to have both left and right-handed chirality, although the existence of right-handed neutrinos is theoretically well motivated [12] only left-handed neutrinos have been observed. One explanation is that right-handed neutrinos may be inert, they do not interact, requiring an additional neutrino mass-generation mechanism to the standard model.

1.1.2 Bosons

The SM bosons account for the different fundamental forces, they are classified as either a gauge or scalar boson. The scalar bosons have a spin of 0 and the gauge bosons have spin 1 and are the force carriers which mediate interactions between particles. There are four gauge bosons, the photon (γ), the gluon (g) and the W and Z boson ($W^\pm, Z$), and only one scalar boson, the Higgs (H). The photon, γ, mediates the EM force and is a massless gauge boson, coupling to all fermions, both quarks and leptons, however it has no EM charge itself.

The gluon, g, is also a massless gauge boson which carries colour charge. The gluon mediates the strong force and couples to itself and quarks since they contain colour charge. Thus gluons not only mediate but also participate in strong interactions, which gives rise to the formation of three/four-gluon vertices. From QCD there are eight independent colour combinations which are possible for gluons, these are given as:

$$\frac{(r\bar{b}+\bar{r}b)}{\sqrt{2}} \qquad -i\frac{(r\bar{b}-\bar{r}b)}{\sqrt{2}}$$

$$\frac{(r\bar{g}+\bar{r}g)}{\sqrt{2}} \qquad -i\frac{(r\bar{g}-\bar{r}g)}{\sqrt{2}}$$

$$\frac{(b\bar{g}+\bar{b}g)}{\sqrt{2}} \qquad -i\frac{(b\bar{g}-\bar{b}g)}{\sqrt{2}}$$

$$\frac{(r\bar{r}-\bar{b}b)}{\sqrt{2}} \qquad \frac{(r\bar{r}-\bar{b}b-2g\bar{g})}{\sqrt{6}}$$

The $W^{\pm}$ and Z^0 gauge bosons are the mediators of the weak force, and unlike photons and gluons, posses masses of about 80 and 90 GeV respectively. The Z^0 boson can mediate the weak neutral force and is its own anti-particle as it has a zero EM charge. Since the Z^0 boson is EM neutral it couples to fermions in the same manner as the photon however it also couples to neutrinos. The W^+ boson has an EM charge of 1 with its anti-particle W^- having a charge of -1. The $W^{\pm}$ boson can mediate the generation of flavour changing weak processes.

The Higgs boson is the only known scalar boson, it is responsible for imparting mass to the Z^0 and $W^{\pm}$ bosons and other fermions and has a zero EM charge. SM particles acquire mass by interacting with the Higgs field, where the greater the mass of the particle the stronger it couples with the Higgs boson. The Higgs boson only interacts with massive SM particles.

1.2 Gauge theories and the Standard Model

The SM is a quantum field theory, and the particles may be represented as excitations of quantum fields. The SM is a spontaneously broken non-abelian gauge theory and it contains elementary scalars, spin one gauge bosons and fermions. In general, spin-0 and spin-1/2 fields (which may be charged or neutral depending on the underlying symmetry group) are referred to as matter fields. Whereas, the spin-1 gauge bosons are referred to as gauge fields.

Lagrangian densities are functions of fields and their derivatives, and are used to explain these quantum fields of the SM and their interactions, where the interactions in SM are described by gauge theories. The Lagrangian density is invariant under a set of transformations, these give rise to the symmetries of the theory. These transformations are represented by matrices and are built by the generators of an associated symmetry group.

The SM groups are $SU(3)_C \times SU(2)_L \times U(1)_Y$, which represent the fundamental forces, electromagnetic $U(1)_Y$, weak-nuclear $SU(2)_L$ and the strong nuclear force $SU(3)_C$. For $U(1)_Y$ there is only one generator which is the photon, for $SU(2)_L$ there are $2^2 - 1 = 3$ generators which are the Z, W^+, W^- bosons, and for $SU(3)_C$ there are $3^2 - 1 = 8$ generators which are the 8 different gluons where QCD arises from the $SU(3)_C$ component. Quantum electrodynamics (QED) and weak interactions arise from the $SU(2)_L \times U(1)_Y$ component and contain $(2^2 - 1) + 1 = 4$ generators (γ, Z, $W^{\pm}$).

Although symmetries are important in nature, symmetry breaking is even more important and the explicit symmetry breaking of a theory arises from external forces. In the case where an external force is the cause of symmetry breaking, the Lagrangian contains some symmetry breaking term which is derived from the equations of motion. However, there is also the case where no external force is required to trigger a symmetry break, this is spontaneous symmetry breaking (SSB). One way to understand the difference is by looking at a simple example taken from classical physics. Let us consider the rotational symmetry of a linear vertical rod shown in Figure 1.4.



(a) Unbroken symmetry, vertical rod is rotationally invariant

(b) Explicit symmetry breaking, rod bends due to force applied on the top.

(c) Spontaneous symmetry breaking, rod bends in an arbitrary direction due to force applied along its axis.

Figure 1.4: Spontaneous symmetry breaking demonstrated by a bending vertical rod.

If a force is applied on the top, perpendicular to its axis, the rod bends and rotational symmetry is lost. This is explicit symmetry breaking, where the external force directly affects and modifies the equations of motion. However if a compression force were to be applied on the top of the rod along the axis, the symmetric equilibrium becomes unstable. The rod then bends in a random fashion and an infinite number of equivalent lowest energy stable states appear, and rotational symmetry is lost.

The main take away in the SBB case, is that when some parameter reaches a critical value, under small perturbations, the lowest energy solution of the symmetry becomes unstable, and a new asymmetric lowest energy solution appears. The new lowest energy solutions are asymmetric, however they are still all related through the action of the symmetry transformations. Thus the equations of motion still obey the original symmetry even though the grounds states do not respect it as such SSB is also called "hidden symmetry".

SSB has substantial applications in gauge theories in particle physics, in an unbroken gauge theory, the gauge bosons must be massless. The only observed massless spin-1 particles are photons, and although gluons are massless, due to confinement they cannot be observed. However, if we consider gauge theory describing weak interactions, the symmetry must be broken in some way, as the Z and $W^{\pm}$ gauge bosons are massive. One way in which the symmetry could be broken is by simply adding explicit mass terms to the gauge bosons and violate gauge symmetry. However, such an explicit symmetry breaking would destroy renormalizability of the theory and the Lagrangian will no longer be gauge invariant.

Thus the phenomenon of SSB appears as a candidate, as we require another form of symmetry breaking which gives us the masses while keeping the theory renormalizable (which is attributed to the Higgs Mechanism). In fact, the Glashow-Weinberg-Salam theory of weak interactions is renormalizable and relies on $SU(2)_L \times U(1)_Y$ having SSB [13]. In 1971, it was specifically shown by G.'t Hooft that even in the presence of SSB, gauge theories are renormalizable [14], solidifying the importance of SSB in gauge theories.

Higgs mechanism on W and Z mass

It is important to understand how SM particles are imparted with mass, in order to understand this we need to consider the Higgs mechanism [11]. The SM Lagrangian is constructed from "sub"-Lagrangians given by,

$$\mathcal{L}_{SM} = \mathcal{L}_{gauge} + \mathcal{L}_{fermion} + \mathcal{L}_{Higgs} + \mathcal{L}_{Yukawa} \tag{1.2}$$

In 1967, Weinberg and Salam applied the Higgs mechanism to the $SU(2)_L \times U(1)_Y$ gauge theory [15]. Having three $SU(2)_L$ gauge bosons, W^i_μ where i =1,2,3 and one $U(1)_Y$ gauge boson, B_μ, where the kinetic terms are given by,

$$\mathcal{L}_{gauge} = -\frac{1}{4} W^i_{\mu\nu} W^{i\mu\nu} - \frac{1}{4} B_{\mu\nu} B^{\mu\nu} \tag{1.3}$$

where $W^i_{\mu\nu}$ is the gluonic field tensor given by, $W^i_{\mu\nu} = \partial_\mu W^i_\nu - \partial_\nu W^i_\mu + g\epsilon^{ijk} W^j_\mu W^k_\nu$, and $B^{\mu\nu}$ is the electromagnetic field-strength tensor given by, $B^{\mu\nu} = \partial^\mu B^\nu - \partial^\nu B^\mu$. A $SU(2)$ doublet of complex scalar fields is introduced,

$$\phi = \begin{pmatrix} \phi_1 + i\phi_2 \\ H^0 + i\phi_3 \end{pmatrix} = \begin{pmatrix} \phi^+ \\ \phi^0 \end{pmatrix} \tag{1.4}$$

which is the $SU(2)$ complex Higgs doublet, where $H^0 = H + v_{ev}/\sqrt{2}$ and the $SU(2) \times U(1)$, we introduce the Lagrangian,

$$\mathcal{L}_{scalar} = \partial_\mu \phi^\dagger \partial^\mu \phi - V(\phi) \tag{1.5}$$

and the most general renormalizable invariant scalar potential is given by,

$$V(\phi) = a^2 \phi^\dagger \phi + \lambda (\phi^\dagger \phi)^2 \tag{1.6}$$

where $\lambda > 0$ and $a^2 < 0$. λ is the term which gives quartic self-interactions between the scalar fields and to ensure vacuum stability, hence $\lambda > 0$. For $a^2 < 0$, the scalar field will develop a non-zero vacuum expectation value (VEV) leading to SSB. There are an infinite amount of degenerate minima rotated by the phase rotation. This leads to the potential taking the shape of a "sombrero", or "Mexican hat", given in Figure 1.5.

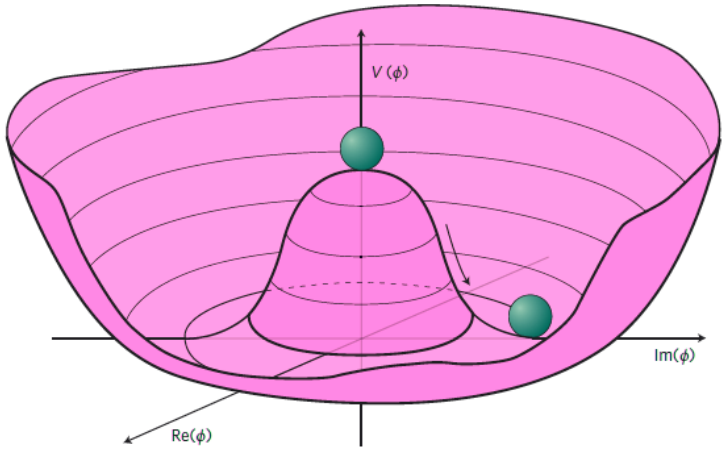


Figure 1.5: Shape of the potential of a complex scalar field, having an infinite number of degenerate minima rotated by the phase rotation, leading to SSB [16].

In order to maintain gauge invariance (the property where by a class of scalar and vector potentials related by gauge transformations describe the same electric and magnetic fields) under $SU(2)_L \times U(1)_Y$, the covariant derivative is introduced,

$$D_\mu = \partial_\mu + ig\frac{\tau_i}{2}W_\mu^i + i\frac{g'}{2}B_\mu Y \tag{1.7}$$

Where τ_i are the usual Pauli matrices [9], g and g' are the $SU(2)_L$ and $U(1)_Y$ gauge couplings respectively, and $Y = 1$. Now, minimizing the potential given in Equation 1.6, we then get,

$$\langle \phi^\dagger \phi \rangle = \frac{-a^2}{\lambda} \tag{1.8}$$

where the VEV is denoted by $\langle \phi^\dagger \phi \rangle$, through $SU(2) \times U(1)$ transformations and due to vacuum degeneracy, we are able to choose that,

$$\langle \phi \rangle = \frac{1}{\sqrt{2}} \begin{pmatrix} 0 \\ v_{ev} \end{pmatrix} \tag{1.9}$$

From the choice of H^0 the scalar doublet has $U(1)_Y$ hypercharge $Y_\phi = 1$, where only a neutral scalar field may gain a VEV in order to conserve electric charge.
Hence, we can interpret ϕ^0 as the neutral component of the doublet. EM is unbroken by the scalar VEV as the electromagnetic charge is $Q < \phi >= 0$. In order for the electric charge to be conserved, we want to preserve the exact electromagnetic symmetry, thus the breaking scheme of the original symmetry group is,

$$SU(2)_L \times U(1)_Y \to U(1)_{EM}. \tag{1.10}$$

Thus after SBB, the subgroup $U(1)_{em}$, having dimension 1, remains a symmetry of the vacuum and so in this case the corresponding gauge boson which is the photon, γ, remains massless. Now looking at the scalar Higgs part, the Lagrangian is given by,

$$\mathcal{L}_{Higgs} = (D_\mu \phi)^\dagger (D^\mu \phi) - V(\phi) \tag{1.11}$$

We introduce gauge fields, B_μ for $U(1)_Y$ and W_μ^i for $SU(2)_L$ in order to make the $SU(2)_L \times U(1)_Y$ symmetry local. In unitary gauge, in the spectrum after SSB takes place, only the physical Higgs scalar is present as there are no Goldstone bosons. Thus if we make a $SU(2)_L$ unitary gauge transformation, the scalar doublet is then,

$$\langle \phi \rangle = \frac{1}{\sqrt{2}} \begin{pmatrix} 0 \\ v_{ev} + H \\ . \end{pmatrix} \tag{1.12}$$

H is the real scalar Higgs boson having mass $m_H = \sqrt{2\lambda} v_{ev}$, and $v_{ev} = \sqrt{a^2/\lambda}$ is the VEV of the theory. The other three degrees of freedom (ϕ_1, ϕ_2, ϕ_3) are absorbed by the weak bosons and from the kinetic term of the Higgs potential, we get,

$$(D_\mu \phi)^\dagger (D^\mu \phi) \to \frac{1}{2}(0 \quad v) |\partial_\mu + ig\frac{\tau_i}{2} W_\mu^i + i\frac{g'}{2} B_\mu|^2 \begin{pmatrix} 0 \\ v_{ev} \end{pmatrix} \tag{1.13}$$

which can be solved to give,

$$(D_\mu \phi)^\dagger (D^\mu \phi) \to \frac{v_{ev}^2}{8} [g^2((W_\mu^1)^2 + (W_\mu^2)^2) + (gW_\mu^3 - g' B_\mu)^2] \tag{1.14}$$

The neutral and the two charged massless Goldstone degrees of freedom mix with the gauge fields corresponding to the broken generators of $SU(2)_L \times U(1)_Y$. In unitary gauge, they then become the longitudinal components of the Z and $W^\pm$ physical gauge bosons respectively.

The Z and $W^{\pm}$ bosons both acquire mass [9], having masses,

$$m_W^2 = \frac{v_{ev}^2 g^2}{4} \qquad m_Z^2 = \frac{v_{ev}^2 (g'^2 + g^2)}{4}. \tag{1.15}$$

Where the standard model predictions for W and Z mass are,

$$m_W \sim 80 \text{ GeV} \qquad \text{and} \qquad m_Z \sim 90 \text{ GeV} \tag{1.16}$$

Fermion mass and the Higgs field

The fermions of the SM get their masses through interactions between the Higgs field and the fermions. The charged lepton is massless since we have that, $m_l^{\bar{l}l} = m_l(\bar{l}_R l_L + \bar{l}_L l_R)$, which mixes the L and R components, breaking gauge invariance. One way to impart the leptons with mass in a gauge invariant way is through the Yukawa coupling of the leptons with the Higgs field. The Yukawa interaction is derived from a Lagrangian density containing an interaction term of a Dirac spinor with a Klein-Gordon (KG) particle. The Lagrangian is given by,

$$\mathcal{L}_{Yukawa} = \mathcal{L}_{Dirac} + \mathcal{L}_{KG} - g\bar{\psi}\psi\phi \tag{1.17}$$

which gives the Yukawa interactions,

$$\mathcal{L}_{Yukawa} = -\sigma_{d_{i,j}} \bar{q}_{L_i} \Phi d_{R_j} - \sigma_{u_{i.j}} \bar{q}_{L_i} \tilde{\Phi} u_{R_j} - \sigma_{l_{i,j}} \bar{l}_{L_i} \Phi e_{R_j} + h.c. \tag{1.18}$$

which respect the symmetries of the SM but generate fermion masses when electroweak symmetry breaking occurs. In the Lagrangian above, $\sigma_{d,u}$ are the 3×3 complex matrices, q_L (l_L) and u_R, d_R (e_R) are the quark (lepton) $SU(2)_L$ doublets and singlets respectively, $\tilde{\Phi} = i\tau^2 \Phi^*$ and h.c is the Hermitian conjugate. Let us consider the example of the electron and its neutrino, where the hyper charge in this case if $Y_L = -1$. The W boson only couples with left-handed fermions, this gives that the $SU(2)_L$ doublet is constructed as,

$$L_L = \begin{pmatrix} \nu_L \\ e_L \end{pmatrix} \tag{1.19}$$

It is known experimentally that the W boson has no interactions with right handed fields. This gives that the right handed electron must be a $SU(2)_L$ singlet, with $Y_R = -2$. Thus, with these hypercharges, the leptons couple, in a gauge invariant manner, to the $SU(2)_L \times U(1)_Y$ gauges fields,

$$\mathcal{L}_{lepton} = i\bar{e}_R \gamma^\mu (\partial_\mu + \frac{ig'}{2} Y_e B_\mu) e_R + i\bar{L}_L \gamma^\mu (\partial_\mu + \frac{ig'}{2} Y_l B_\mu + \frac{ig}{2} \tau_i W_\mu^i) L_L. \tag{1.20}$$

In a similar fashion, all fermions can be contained in the SM. Where a Dirac fermion mass term is given as follows,

$$\mathcal{L}_{mass} = -m(\bar{\psi}_L\psi_R + \bar{\psi}_R\psi_L). \tag{1.21}$$

As well the gauge invariant Yukawa coupling of the Higgs boson to the down and up quarks is given as,

$$\mathcal{L}_{d,u} = \sigma_d\bar{q}_L\Phi d_R + \sigma_u\bar{q}_L\tilde{\Phi}u_R + h.c \tag{1.22}$$

Once the Higgs field acquires a VEV, and after rotation to the fermion mass eigenstate basis, all fermions acquire a mass given by,

$$m_f = \frac{\sigma_f v_{ev}}{\sqrt{2}} \tag{1.23}$$

Although the mass term for the fermion may be generated through this procedure in a gauge invariant way. It is unable to specify the value of the mass since σ_f is arbitrary. However, we can see that the masses for the down and up-type quarks are then given by,

$$m_d = \frac{Y_d v_{ev}}{2} \qquad\qquad m_u = \frac{Y_u v_{ev}}{2} \tag{1.24}$$

It is important to note that the electroweak symmetry breaking mechanism does not provide any additional insight on the possible reason for the large variety of the fermion masses, referred to as the flavour hierarchy.

1.3 The Standard Model's missing pieces

Although the SM is the most successful theory of particle physics to date providing a very solid grounding on understanding how nature behaves, it is not a perfect theory. There are a few open questions which the SM is unable to resolve. Even though the discovery of the Higgs boson [17, 18] completed the SM, there is still an unexplained discrepancy between the electroweak scale ($\mathcal{O}(100$ GeV$)$) and the Planck scale ($\mathcal{O}(10^{19}$ GeV$)$), known as the hierarchy problem. One other such discrepancy is gravity, the SM is unable to explain gravity. The approach of simply adding a graviton to the SM does not generate what has been experimentally observed without making some undiscovered modifications to the SM. It is also widely considered that the SM is incompatible with general relativity, the most successful theory of gravity to date.

The SM is also unable to account for neutrino masses, traditionally the SM treats neutrinos as massless. However, it has been experimentally confirmed that neutrinos, although very small, do have mass, as explained in section 1.1. Mass terms for neutrinos may be added to the SM by hand, however this brings about new theoretical complications. For one, these mass terms would need to be extremely small, but it is not clear if neutrino masses would emerge in the same fashion as other fundamental particles.

The SM also does not fully explain baryon asymmetry. The universe is made mostly of matter, however according to the SM, matter and antimatter should have been created in equal amounts. This is provided the initial conditions of the universe did not involve disproportionate matter relative to antimatter. Yet, there is no mechanism in the Standard Model to sufficiently explain this asymmetry. This open question is termed charge-parity violation (CPV) [19]. The strong-CP problem [20] links to the query as to why CPV is not present in the strong-interactions sector as it naturally allows for this.

In the context of this dissertation, the biggest flaw in the SM, is its inability to account for dark matter (DM) or dark energy. From cosmological observations, the SM is only able to explain about 5% of the mass/energy in the universe. There are several astrophysical evidences which will be discussed in detail in the next section. Evidently, before the 1980's neutrinos were considered to be potential DM candidates as they have a non-luminous nature. It was then experimentally observed that neutrinos had the potential of forming superclusters at first and then breaking down and forming galaxies. However, this is contrary to astrophysical observations and thus this idea was discarded. Dark matter is an obscure substance which may be another undiscovered particle, which would mean the SM is yet to be complete.

1.4 Collider Objects and variables

Before moving on any further, it is important to discuss some important variables and objects used throughout this dissertation. Here I will introduce collider specific objects and variables such as jets and rapidity. As well as specify some terminology in context of colliders such as luminosity.

1.4.1 Luminosity

The luminosity, L, characterises an accelerator's performance, where σ is the cross section and the number of events per second is denoted R. Cross-section, σ, refers to the probability that a specific process will occur. The rate at which collisions occur is given in terms of the luminosity and cross-section,

$$R_{col} = L\sigma \tag{1.25}$$

Luminosity has the dimensions $\text{cm}^{-2}\text{s}^{-1}$, however is generally given by pb^{-1} or fb^{-1}. To understand the concept of luminosity, let us consider a proton-proton accelerator having N particles per beam. The number of collisions, N_{col}, in terms of the first beam area A_1, with n_1 particles per bunch, is the probability of a collision, $P_{col} = \sigma n_1/A_1$, multiplied by the number of ways a collision can happen. Namely the number of particles per bunch n_2 in the second beam is,

$$N_{col} = \frac{\sigma n_1 n_2}{A_1} \tag{1.26}$$

This is happening every time two bunches cross, thus multiplying N_{col} by the rate of the bunch crossing f, we have that the overall rate of collisions, given by,

$$R_{col} = \sigma f \frac{n_1 n_2}{A_1} \tag{1.27}$$

So from Equation 1.25, the luminosity is given by,

$$L = \frac{f n_1 n_2}{A_1} \tag{1.28}$$

This quantity is the instantaneous luminosity, it can be thought of as the "brightness" of the colliding particles, giving a measure of the collision rate. We see from Equation 1.28, reducing the cross section of the beam increases the luminosity, as well by increasing the number of particles in the beam or the revolution frequency. The integrated luminosity is simply defined at the instantaneous luminosity integrated over time. The luminosity relates to measurements of cross-sections, thus measuring the luminosity is important. There are dedicated instruments which can be used to measure it. Two examples in ATLAS are LUCID (LUminosity measurement using Cherenkov Integrating Detector)[21] and BCM (Beam Conditions Monitor) [22]. However, at the LHC the luminosity is more commonly measured indirectly, where the visible cross-section for a reference process is measured and then appropriately scaled.

1.4.2 Co-ordinates

The usual co-ordinates are cartesian (x, y, z) or spherical (r, θ, ϕ), shown in Figure 1.6. The positive x-axis lies along the incident proton beam direction, as the beams axis is uniquely defined. The origin of the co-ordinate system is chosen to be fixed where the beams collide, as this is in general a well defined point at the center of the detector. The angle ϕ is the azimuthal angle around the beam axis, and rather than using the polar angle θ, a new, Lorentz invariant, quantity is introduced, rapidity denoted by y, and is defined in terms of the particle kinematics such that,

$$y = \frac{1}{2} \ln \left(\frac{E + p_z}{E - p_z} \right) \tag{1.29}$$

where E is the energy and p_z is the z-component of the momentum of the particle considered. The detector geometry is cylindrical and the $y - \phi$ co-ordinates exploit the cylindrical symmetry far better as each detector element covers the same area in $y - \phi$ space.

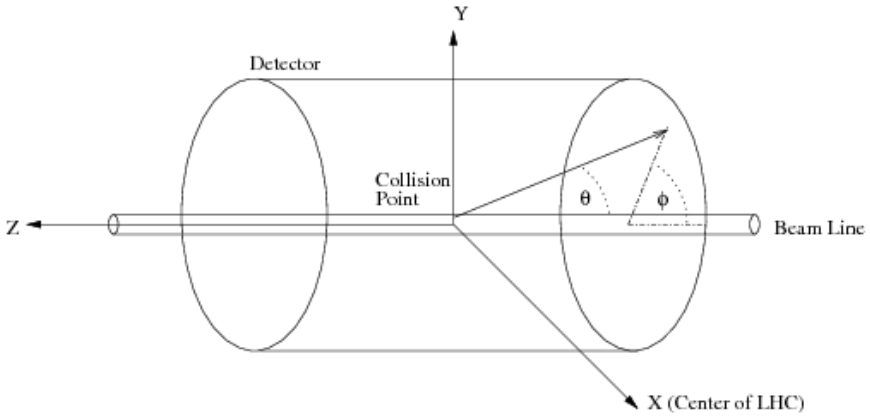


Figure 1.6: Illustration of general detector co-ordinate system [23].

However, for highly relativistic particles the rapidity can be difficult to measure and in general the z-component of the momentum is not measured as it is along the beam axis. Thus, to resolve this, another quantity is introduced, termed the pseudorapidity, denoted by η, given in Figure 1.7. The pseudorapidity is obtained through the polar angle θ as $\eta \equiv -\ln \tan \theta/2$. The factor of a half comes from the fact that it scales both angular co-ordinates in the same way.

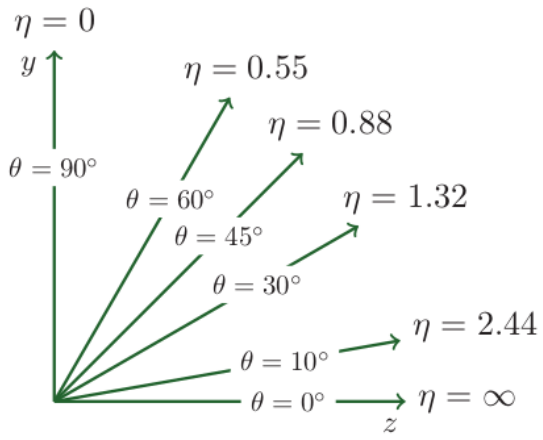


Figure 1.7: Pseudorapidity, η, defined to exploit cylindrical symmetry, the value of η increases as we move away from the center of the detector [24].

1.4.3 Transverse momentum and missing energy

The momentum of each particle produced may be decomposed into a component which is parallel (along the z-axis) and perpendicular (transverse, xy plane) to the beams. The transverse component of the momentum, denoted by p_T is given by, $p_T = \sqrt{p_x^2 + p_y^2}$, and is the component of the momentum in the transverse plane, it is used as only components along the x-y plane are measured. This in turn implies that, $p_x = p_T \cos\phi$ and $p_y = p_T \sin\phi$. In a similar fashion the transverse mass, which is also invariant under longitudinal boosts, is defined as $m_T \equiv \sqrt{m^2 + p_T^2}$. A collision is characterized by an initial total energy and momentum $(E_{in}, \vec{p}_{in})$ and in the final state with n particles we have the total energy and momentum given by,

$$E = \sum_i^n E_i \qquad \text{and} \qquad \vec{p} = \sum_i^n \vec{p}_i \tag{1.30}$$

However sometimes an experiment may measure that, $E < E_{in}$ and $\vec{p} \neq \vec{p}_{in}$. In this scenario, generally it means that one or more particles traversed the detector without being detected (but can also be due to detector effects). Typically this happens with neutral particles such as neutrons, π^0 and K_L^0, but mostly with neutrinos as the former may have long lifetimes and decay outside the detector. In order to quantify this process, the concept of missing transverse momentum or missing energy (MET) is introduced. MET is defined as the negative of the sum of scalar p_T of all other objects [24],

$$E_{MET} = \sqrt{(E_{in} - E)^2 - (\vec{p}_{in} - \vec{p})^2 c^2} \tag{1.31}$$

Since energy is not a vector, the term missing momentum is more appropriate however both terms are usually used interchangeably. One example of a scenario with missing energy is the decay of a W boson. A W^+ boson can be produced via the collision of a u-quark and anti-d-quark. The W^+ boson then decays to a neutrino-lepton pair, the muon is detected and its momentum can be measured. However, the neutrino escapes the detector without being detected, thus the total sum of the transverse momentum is not zero. Hence, the experimental signature of the neutrino in the experiment is the missing transverse momentum or MET.

1.4.4 Invariant mass

The invariant mass of an object or system of objects, is the total energy and momentum of that object that is the same in all reference frames. When a system as a whole is at rest the total energy of the system divided by c^2 is the invariant mass and if the system is a single particle, the invariant mass is simply the rest mass,

$$m^2c^4 = E^2 - \vec{p}^2c^2 \tag{1.32}$$

and for a system of N particles, the invariant mass m_i of the decaying particle is given by,

$$m_i^2c^4 = \left(\sum_i^N E_i\right)^2 - \left(\sum_i^N \vec{p}_i c\right)^2. \tag{1.33}$$

1.4.5 Jets

In the detector quarks which have colour charge can split into gluons which in turn can decay into quark-antiquark pairs leading to a cascade of particles similar to that of photons (gamma rays decay to an electron and positron pair, which in turn emit a gamma ray which then again decays to an electron positron pair and so on). This collection of quarks and gluons (referred to as partons) leads to colour neutral hadrons which are then detected by depositing energy in the detectors. The energy flow of a coloured parton can be approximated by the colour-neutral hadrons created from it, the collection of these collimated bunches of hadrons are referred to as jets, where essentially each jet is coming from a single parton. Jets are not fundamental objects, but rather a construction to capture hadrons originating from a single parton [24]. A generic jet forming algorithm can be represented as a mapping from a set of hadrons with four-momenta $\{p_1^h,\ p_2^h,\ ...p_N^h\}$, to a set of jets with four-momenta $\{p_1^j,\ p_2^j,\ ...p_M^j\}$, where in general $p^j = \sum_{i\in j} p_i^h$ and $N > M$.

Thus the jet axis is defined by the resultant vector sum of the input four-momenta. The jet algorithm determines which input objects go in which jets, such as energy deposits in calorimeter or tracks. A distance measurement R, the radius of the jet formed, is used and is equivalent to the opening angle in collider co-ordinates. In this dissertation the jet algorithm used is the anti-k_t algorithm [25], and is the most used jet algorithm at the LHC. It begins with the input object having the highest p_T, that jet then absorbs all softer input objects within an angular radius parameter, R_0. This forms cone-like jet shapes with a roughly circular cross sectional area given by πR_0^2. The constituents of a jet usually have zero or very small mass, the jet itself however, can have a non-negligible mass, which can be calculated from,

$$m_j^2 = \left(\sum_{i \in jet} E_i\right)^2 - \left(\sum_{i \in jet} \vec{p}_i\right)^2 . \tag{1.34}$$

Where E_i and $\vec{p}_i$ are the energy and momentum of the ith constituent of the jet, this is more notably important when dealing with jets created from heavy objects. Jets can also be b-tagged, this means the jets contain B mesons or originates from a b-quark. b-tagging is very important as it is useful to distinguish between many physical processes. A B-quark has a much longer lifetime compared to other quarks produced. Except for the top-quark, the bottom-quark is much heavier than all other quarks and when it decays, it produces more charged particles compared to other hadrons.

1.5 Beyond the Standard Model: Dark matter

It is well known that DM is an obscure and mysterious gravitational substance whose evidence is undeniable. It is supported by copious and consistent astrophysical and cosmological observations [26]. On large scales, the average DM density is around 6 times that of the baryon density [27]. However, on smaller scales, the distribution of DM is fairly anisotropic and hierarchical as it is comprised of clusters, galaxies and galactic sub structures (at least in the cold dark matter case [28]). The first indications of a non-luminous matter with densities much higher than radiating matter was in 1933. Astronomer F. Zwicky [29], studying the red-shifts of Coma galaxy clusters, noticed that there is a scatter in the apparent velocity of the eight galaxies within the cluster. This meant that the density of the cluster was higher than what is measured for only the visible matter. Giving to the early predictions of non-luminous matter and leading to a surge of experimental and theoretical studies.

Although there have been numerous studies on DM since then, there are a few major milestones which make the existence of dark matter indisputable. One such study alluding to the existence of DM pertains to the rotation curves of galaxies. In 1939 H. W. Babcock measured the rotation curve for the Andromeda Galaxy, and reported that the mass-luminosity ratio increases radially [30]. In the 1970's, V. Rubin [31] and A. Bosma [32], used optical images to study the rotation curves of spiral galaxies, since one may infer the mass distribution of a galaxy from its rotation curve.

It was then found that contrary to expectations, the rotation curves were almost flat and had no declination in a galaxy's outer reaches. Thus from Kepler's laws, in order to resolve this discrepancy, some non-luminous mass must be present, confirming the existence of Dark Matter. In the 1980's a stream of observations supported the presence of dark matter including gravitational lensing. Gravitational lensing is the observed distortion of background galaxies into arcs when their light passes through such a gravitational lens. Observations of areas around massive clusters of galaxies identified "warped" background galaxies, where their distortions reveal where the densest concentrations of mass lie. It was found that most of the mass of the clusters were not located at the source of the radiation emissions implying there is some non-visible matter present.

As well in the 1990's the modern paradigm of the hot big bang cosmology was established from experimental explorations of the cosmic microwave background (CMB). Where the CMB is a uniform electromagnetic radiation remnant from the early stages of the universe, also known as "relic radiation". It is estimated that the CMB originated about 4×10^5 years after the big bang dating back to the epoch of recombination (time when the first atoms formed), when the universe was a "soup" of hot, ionised gas. Before this epoch the photons from the CMB were tightly coupled to the baryons, recombination increased the range of these photons from short to long length scales. This lead to their decoupling and in turn they were freely available to travel through space.

The CMB photons retain information on the state of the universe during recombination, and thus, information on the general nature of matter in the early universe. Over time the presence of gravity increased the small fluctuations in the CMB, which led to the formation of currently observed galaxy clusters. The power spectrum of the CMB, which characterises the size of fluctuations as a function of angular scale, is determined by the hot gas oscillations in the early universe. The oscillation amplitude and resonant frequencies are dependent on the composition.

This power spectrum provides a strong handle to map the density of matter in the early universe. Latest studies [27] report the universe to be composed of 5% visible matter, 27% dark matter and 68% dark energy (the driving force of the universe's expansion). Over time there has been a growing interest in dark matter and and recent years have seen an increase in searches exploring the dark sector, yet there is still to be direct measurements of dark matter. There is no suitable particle in the standard model which fits the role of dark matter and making up 27% of the universe, the exploration of dark matter is a necessity in order to further our understanding of physics. In general most dark matter searches at the LHC are focused on Weakly Interacting Massive Particles (WIMPs).

In order to begin considering DM candidates, it is important to understand the amount of DM that is expected to have remained at this point in the lifetime of our universe, referred to as relic density. It is believed that the generation of DM in the early universe can progress from particle-antiparticle annihilation or through thermal or non-thermal production. There are two avenues considered when trying to understand the "particle" nature of DM. The first assumes that larger superclusters (halos) would form initially before later breaking down to smaller halos (galaxies). This however, is only possible if the DM component is relativistic (hot dark matter) during the beginning stages of the universe.

The second avenue follows the standard cosmological model. Although this is not in the scope of particle physics it is important to understand the nature of dark matter in the universe. This model which is successful in explaining observations for the CMB, thermal history as well as large scale structures of the universe. Here DM is considered to be non-relativistic (cold dark matter). In this case, DM is considered to be a pressure-less component of matter decoupled. The latter idea is more favoured as there is no reason to assume that DM's origins differ to that of neutrons, CMB photons, and other light elements from thermal decoupling. The former idea of hot DM would lead to a very different galactic structure, which is mismatched to current observations and is thus more largely disfavoured. If we consider the density parameter Ω_χ, which is the universe's energy content that a certain particle species χ (DM in this case) accounts for,

$$\Omega_\chi = \frac{\rho_\chi}{\rho_c}, \qquad \rho_c \equiv \frac{3H_0^2}{8\pi G}. \tag{1.35}$$

ρ_c is the critical density (density in which the universe is flat, ρ_χ is the energy density of the particle species, H_0 is Hubble's constant today and G is the gravitational constant.

The DM relic density can then be given by $\Omega_\chi h^2$, where $h = H_0/100$, and $\rho_\chi = m_\chi n_\chi$, where m_χ is the mass parameter associated to the DM mass and n_χ the number density. The number density is then defined as $n_\chi = Y s_0$, where Y corresponds to the DM yield today and s_0 is the entropy density today. Having $< \sigma v >$, which is the thermal average of the total annihilation cross-section multiplied by the particle velocity. We see that the smaller the annihilation rate, the larger the abundance of DM in the present universe, where the DM relic density is expressed as,

$$\Omega_\chi h^2 = \frac{m_\chi Y h^2}{\rho_c} \approx \frac{3 \times 10^{-27} \mathrm{cm}^3 s^{-1}}{< \sigma c >} \tag{1.36}$$

In the past decade the search for dark matter particles has become a major focus at the LHC, however there has still been no sign of these particles as of yet. The absence of results so far, may mean that if dark matter interacts with SM particles the interactions may be very weak and so the experimental signals are subtle. Combining this with the emergence of new dark matter models which mirror interactions of ordinary matter but have not yet been caught by existing models, may indicate a large class of non-standard dark matter signals may have been overlooked. There are several theories on the nature of dark matter which has led to many different search and detection methods for dark matter.

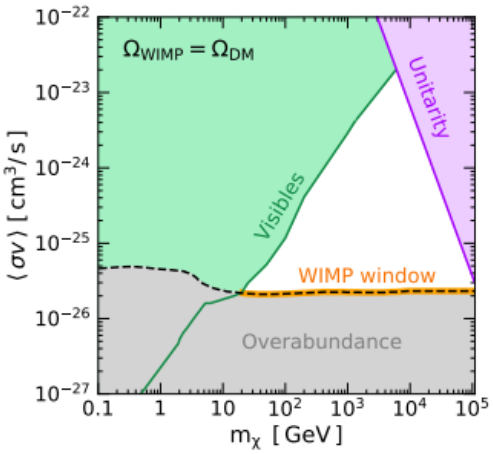
1.5.1 Particle candidates

Stable dark matter in nature is classified as cold dark matter, WIMPs (weakly interacting massive particles) [33] are one potential candidate for cold dark matter. This is dark matter which is stable and long-lived enough to initially form galaxies and then superclusters. WIMPs evolved from SUSY (supersymmetry) which is an extension of the standard model where there is an additional symmetry between fermions and bosons [34]. This extension tells us that for every fermion there is an associated superpartner boson and vice versa essentially doubling the number of particles. From SUSY there is a scheme of particles where several are potentially dark matter candidates. Some examples are the sneutrino (the superpartner of the neutrino), the gravitino (the superpartner of the graviton) and the neutralino (this is the superposition of neutral partners of the Higgs boson and other gauge bosons). These SUSY particle candidates may all be referred to as WIMPs. However WIMPs may also manifest themselves as the lightest excitations in theories which consider extra-dimensions of space, these are known as Kaluza-Klein particles [35]. Many BSM approaches proposed opt for the WIMP model as a potential explanation of DM, however there is no experimental evidence.

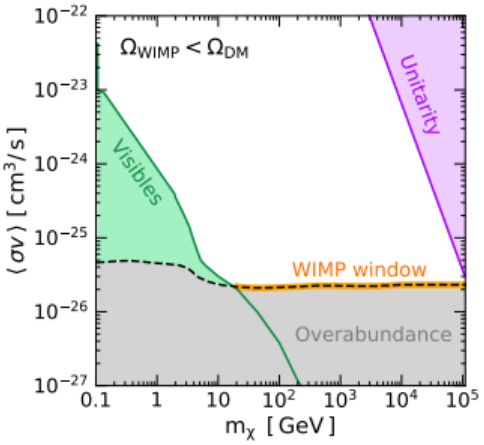
The main factor keeping the WIMP model under consideration, is the WIMP miracle. Where a particle having a weak coupling to the SM and a mass on the weak scale, naturally matches the relic density measured from the CMB [36] making it a "perfect" candidate.

1.5.2 Indirect detection

Indirect detection focuses on searching for products of DM interactions, which in particular, rather than giving DM particles, lead to SM particles. The annihilation cross-section is expected to be of the order 10^{-26} cm^{3}s^{-1}, from the measured cosmological DM density. Indirect detection experiments attempt to probe products emerging from DM particle annihilation. If DM is presumed unstable, it would then decay, producing decay products which are observable, there is a large number of experiments which have been created in order to try and detect these decay products. Some of these experiments use γ-rays (HESS [37], MAGIC [38]), neutrinos (IceCube [39], Baksan [40], ANTARES [41]), X-rays (NuSTAR [42], Suzaku [43]), cosmic rays (HAWC [44]) and some detectors in space (AMS [45], FermiLAT [46]) to name a few. These experiments, as well as others not mentioned, have so far been unable to provide conclusive evidence, however, they have been successful in reducing the parameter space for indirect detection methods. Several experiments are being upgraded, which would allow for higher indirect detection sensitivity searches, the current bounds on DM for indirect searches is shown in Figure 1.8.



(a) Bounds on generic thermal WIMP window assuming WIMP DM is 100% of all DM.



(b) Bounds on generic thermal WIMP window assuming sub-dominant WIMP content.

Figure 1.8: Current combined lower limit on dark matter for s-wave $2 \to 2$ annihilation, standard cosmological history [47].

1.5.3 Direct detection

There are several direct dark matter detection efforts such as CRESST-II [48], XENON10/XENON100 [49, 50] and DAMA/LIBRA [51]. These experiments are searching for dark matter in sub-MeV scale scattering events [52]. The central focus of this experiment comes from the idea that in the early universe dark matter was produced thermally and declined through annihilation to ordinary matter reaching stability. The aim is to attempt to record an event when a dark matter particle is scattered off of a target material, however these events are very rare. Direct detection methods are searching for dark matter signal excess over the background, however there have been no promising results as yet.

1.5.4 Collider searches

Searching for dark matter in accelerators can be quite an arduous task. In order to come up with collider testable scenarios it requires a combined effort of theorists and experimentalists. Naturally dark matter is not luminous and so in collider final states one would expect a lot of missing energy. In order to measure DM since it is not visible, let us consider the general design of a detector. Colliders have what is called a tracking system, this system measures the charged particles which are emerging from the interaction point in the collider. There are two calorimeters, the electromagnetic calorimeter and the hadronic calorimeter. The electromagnetic calorimeter measures energy deposits from electromagnetic particles such as electrons and photons. Whereas the hadronic calorimeter measures the energy deposited from charged and neutral hadrons which are coming from quarks (such as kaons and pions). Muons are very long lived and so are not detected by the electromagnetic calorimeter, instead there are tracking detectors which record the interactions of the muons in the detector.

Dark matter may present as missing energy in the detector, but it is not the only source of missing energy. Neutrinos are the only SM particles which do not interact with any of the detectors as they are both colour and charge neutral and interact only with the weak force, which is too faint for the detectors and so contributes to a missing energy signal. One search technique for dark matter involving a missing energy signature is guided by simplified models including a WIMP-like dark matter particle and a mediator particle which would be able to interact with the known ordinary matter. This mediator particle may be a known particle or unknown, hypothetical particle. These types of searches can be useful as they may be simple in general thus can be used as benchmarks between LHC results and those from non-collider dark matter experiments.

Another search method from simplified models is when the mediator is a hypothetical particle, instead of searching for the dark matter particle, the search is for the mediator through its decay into SM particles [53]. In addition to missing momentum from dark matter candidate particles, in general searches try look for at least one highly energetic object such as a jet or a photon. If a dark matter particle is produced with a photon or high-p_T jet then the final state signature will show only a photon or high-p_T jet with a large missing momentum.

The focus of this dissertation will be designing an analysis strategy, as well as performing a collider search for a non-standard dark matter signal search through unique collider topologies. Recent phenomenological papers have explored the possibility of accessing the dark sector with unique collider signatures which have never been considered. The base for the proposed study will be jets linked to the dark sector. Chapter 2 focuses on dark matter searches via a unique collider topology through a dark photon and hypothetical heavy-top quark. Chapter 3 considers a QCD-like dark sector investigating dark matter through unique jet like objects known referred to as semi-visible jets. Finally, Chapter 4 investigates using quantum computing to perform track reconstruction for LUXE, a new proposed collider.

2 Dark matter searches through a dark photon and heavy-top quark partner

2.1 Dark photons

A feasibility study of a possible search for a hypothetical particle connected to dark matter called a dark photon, was performed. A dark photon is a new gauge boson, it is dark as it arises from the symmetry of a hypothetical dark sector, composed of particles completely neutral under SM interactions [54]. Although this particle is dark it is an interesting and compelling particle to consider as it may be detected through kinetic mixing with the ordinary photon. The kinetic mixing of the dark photon and the visible photons lead to the dark photon very weakly coupling to electrically charged particles [55]. This kinetic mixing is always possible due to the field strengths of the two Abelian gauge fields which, when multiplied together give a dimension four operator, which means that the two gauge bosons can transition into each other as they propagate. This kinetic mixing thus provides a portal between the dark and visible sectors and it is this portal that makes the dark photon possible to detect in experiments. As such allowing for a non-gravitational window into the existence and detection of dark matter and giving a promising search scheme for dark matter.

There are two kinds of dark photons, the massive and the massless, whose properties and experimental signatures are quite distinct [55]. The massless dark photon does not couple directly to any of the SM currents but instead interacts with ordinary matter, however only through operators with dimensions greater than four. Unlike the massless dark photon the massive kind couples to ordinary matter through a current (having arbitrary charge), given by a renormalizable operator with dimension four. Because the massive dark photon couples with ordinary matter it is more readily accessible for collider searches and is the focus of this work. There are a number of ways massive dark photons may be produced [56]. The Lagrangian of the dark photon, γ_d, is given by [57],

$$\mathcal{L} = \mathcal{L}_{SM} - \frac{1}{4}(F'_{\mu\nu})^2 - \frac{\varepsilon}{2}F'_{\mu\nu}F_Y^{\mu\nu} + \frac{1}{2}m^2_{\gamma_d}(A'_\mu)^2. \tag{2.1}$$

Where $F'_{\mu\nu} \equiv \partial_\mu A'_\nu - \partial_\nu A'_\mu$ is the field strength tensor of the $U(1)'$ massive gauge field A'_μ, whose vector gauge boson is the dark photon γ_d. The kinetic mixing operator, ε, between $F'_{\mu\nu}$ and $F_Y^{\mu\nu}$ is dimensionless, where $\varepsilon \sim 10^{-2} - 10^{-8}$, and generated via loops of particles charged under $U(1)_Y$ and $U(1)'$.

2.1.1 Dark photon production modes

Dark matter annihilation

Dark photons may be produced via dark matter annihilation processes with two modes depending on the relative mass between the dark photon γ_d and the dark particle χ [56]. For the first scenario if $m_{\gamma_d} < 2m_\chi$, annihilation occurs via $\chi\chi \to \gamma_d\gamma_d$. However,for the alternative scenario where $m_{\gamma_d} > 2m_\chi$, we have "direct annihilation" $\chi\chi \to \gamma_d* \to$ SM SM, where in the s-channel the virtual dark photon γ_d* is exchanged and the final state is SM particles. The relevant Feynman diagrams for these processes can be seen in Figure 2.1.

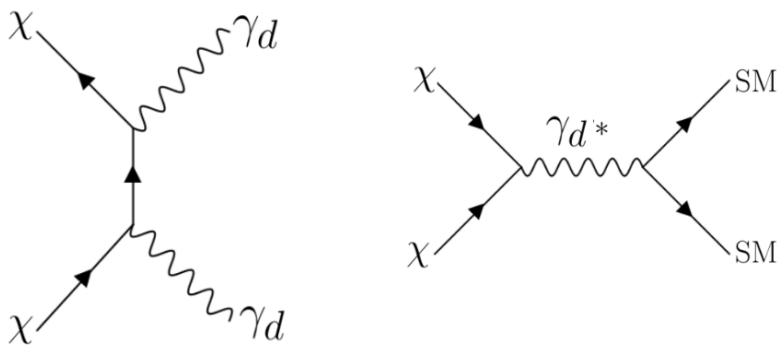


Figure 2.1: Feynman diagrams showing dark photon production via $\chi\chi \to \gamma_d\gamma_d$ (left) and the resonant production of SM particles $\chi\chi \to \gamma_d \to$ SM SM (right).

Electron Bremsstrahlung

High luminosity fixed target experiments can produce dark photons through radiative emission, electrons beams incident on a nuclei target of high atomic number (Z) may emit dark photons [56]. This process is referred to as γ_d-strahlung and is analogous to that of the SM photon bremsstrahlung, however the kinematics and rates differ due to the coupling and mass of the dark photon. The dark photon can be radiated from an electron in either the initial or final state as shown in Figure 2.2, but for both cases the decay is on shell and may travel some distance before decaying into two DM particles or leptons. The dark photon emitted by an electron energy angle distribution may be described by the Weiszsacker-Williams approximation [58].

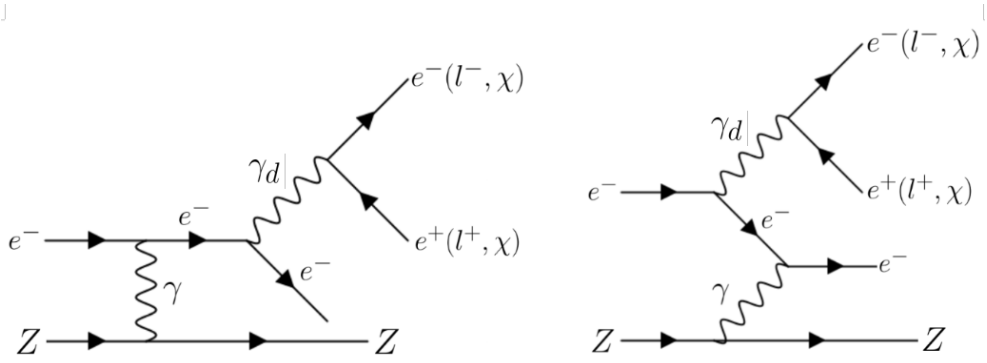


Figure 2.2: Feynman diagrams showing dark photon γ_d emitted from an electron in the final state (left) and initial state radiation (ISR) (right).

The QED Bethe-Heitler and radiative trident processes are also competing reactions to the γ_d-strahlung shown in Figure 2.3 and Figure 2.4, where the Bethe-Heitler is the dominant process. However in principle the separation of the two processes is possible since their kinematics differ. For the Bethe-Heitler case one of the leptons is boosted with the other being softer. For the "Bremsstrahlung" case the recoiling electron is soft, scattering at large angles and the dark photon decay products are highly forward boosted [56].

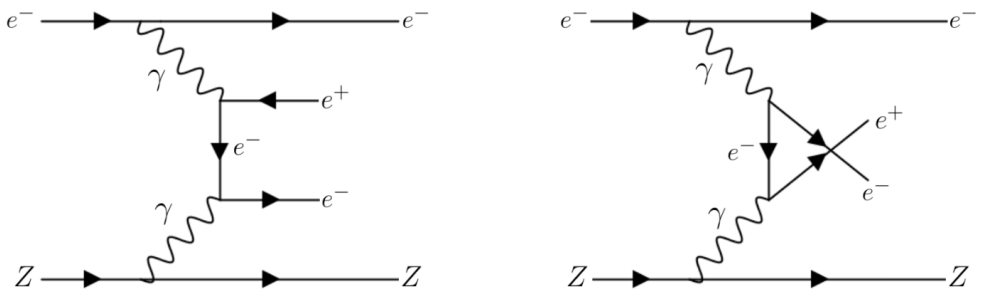


Figure 2.3: Feynman diagrams of the QED Bethe-Heitler (space-like) tridents reactions. It may appear as though the lower photon is radiated forwards in time from the Z boson upwards, however this is not the case, for this process the lower photon is radiated by the electron. In the diagram on the right the two final state electrons are swapped.

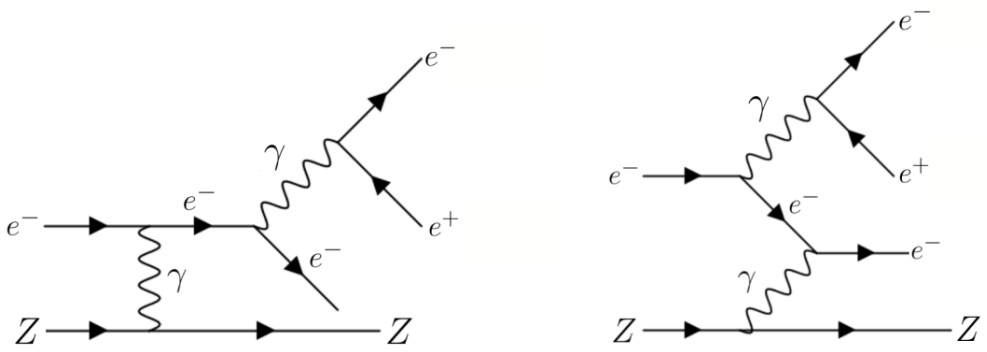


Figure 2.4: Feynman diagrams of the QED radiative (time-like) tridents reactions.

e^+e^- annihilation of bound electrons in atoms

The dark photon may be produced through the resonant $e^+e^- \to \gamma_d$ or non-resonant $e^+e^- \to \gamma_d\gamma$ positron-electron annihilation shown in Figure 2.5. If the center of mass energy $\sqrt{s}$ is of a few tens of MeV then the dominant production process is $(e^+e^- \to \gamma\gamma)$ electron-positron annihilation in a bound electron. Which gives a two photon production process, however, it is possible for the dark photon γ_d to replace one of the SM photons.

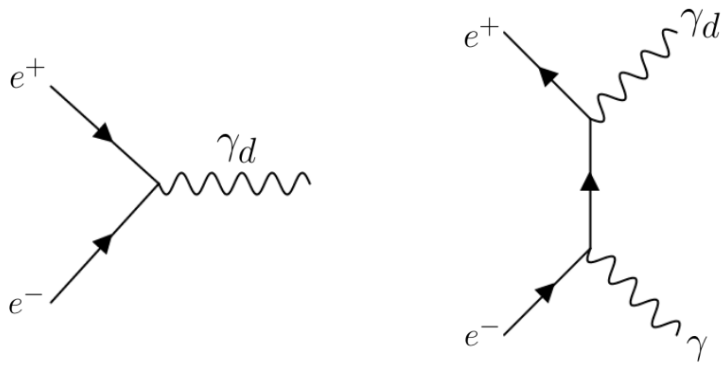


Figure 2.5: Feynman diagrams for the dark photon γ_d production via the resonant $e^+e^- \to \gamma_d$ (left) and non resonant $e^+e^- \to \gamma_d\gamma$ (right) electron-positron annihilation.

Compton-like scattering

A recent study for an alternative dark photon production method, is based on Compton-like emission [59], whereby reactions induced by photons on bound electrons in target atoms give to a dark photon $\gamma e^- \to \gamma_d e^-$ shown in Figure 2.6. This reaction may also be an effective strategy for the production of dark scalar mediators or axion-like pseudoscalars.

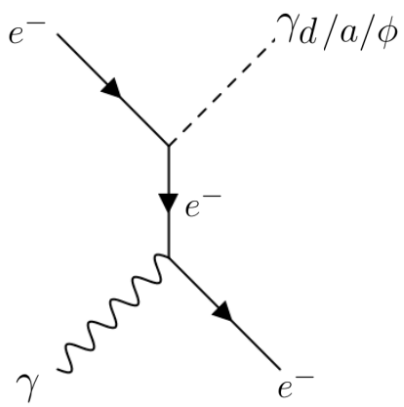


Figure 2.6: Feynman diagram showing alternative production of a dark photon through Compton-like scattering.

Meson decays

The production of the dark photon may happen through the decays of the charged and neutral pseudoscalar (P) and vector (V) mesons via $\pi^0 \to \gamma_d\gamma$ given by Figure 2.7, $V^\pm \to \pi^\pm\gamma_d$ and $P^\pm \to \pi^\pm\gamma_d$ [60]. The last process however is only possible when the dark photon γ_d is massive and the decay rate is proportional to the mass of the dark photon squared ($m^2_{\gamma_d}$).

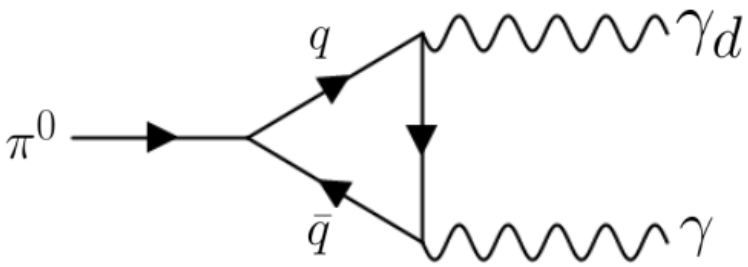


Figure 2.7: Feynman diagram showing neutral meson decay to dark photon and standard model photon.

Drell-Yan

In this process a quark and anti-quark annihilation from different hadrons produces the dark photon via $q\bar{q} \to \gamma_d$ [57] as shown in Figure 2.8. This dark photon can then also decay to a leptonic or hadronic pair. This process also provides a decay vertex and invariant mass measurement which some other production modes cannot.

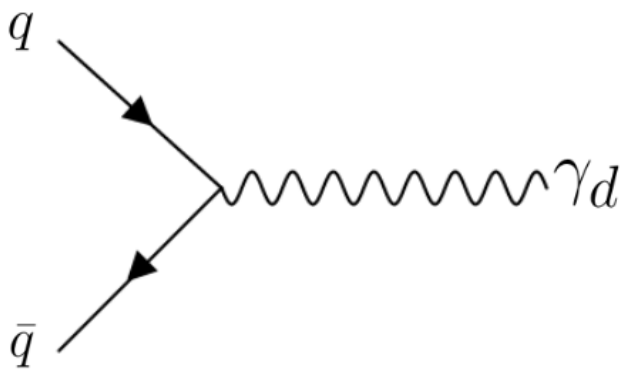


Figure 2.8: Feynman diagram showing Drell Yan production of a dark photon.

2.1.2 Dark photon decays and detection

If kinematically allowed, for example $m_{\gamma_d} > 2m_\chi$, it is expected that dark photons will predominantly decay to invisible dark sector final states. If there are no such decays allowed, then due to its suppressed coupling to the electromagnetic current, the dark photon will then decay to visible SM final states. There are three unknown parameters in the minimal dark photon model [61], ε the kinetic mixing strength, m_{γ_d} the mass of the dark photon and the decay fraction of the dark photon into invisible dark-sectors. Which in general is assumed to be either one or zero and is dependent on whether the final states are kinematically allowed for the invisible dark sector. The signatures for these two decays are marked quite differently. The decays of dark photons into DM particles of course will escape the detection of particle detectors but may be constructed by missing mass or missing momentum techniques. In principle the dark photon may decay into a mixed final state of SM and DM particles. This would benefit the identification from missing energy techniques which are highly sensitive to particles produced in the final state [56].

Visible Dark photon decays

In cases where dark photon decays to the invisible dark-sector are kinematically forbidden, the final states of the dark photon decay will be visible SM states. As well, if the kinetic mixing strength is given to be $\varepsilon \gtrsim \mathcal{O}(10^{-3}) \times (10\,\mathrm{MeV}/m_{\gamma_d})$, this will give to a prompt dark photon decay. However, the dark photon decay may be significantly far from the production point for smaller mixing strengths [61].

Prompt Dark photon decays

The natural width of the dark photon is negligible compared to the mass resolution of any experiment. If prompt dark photon decays produce a resonant peak structure in the invariant mass spectrum, then their backgrounds very seldom have sharp features and mostly produce spectra. Experimentally the focus is typically on leptonic decay channels e^+e^- or $\mu^+\mu^-$ as these are much easier to identify and trigger. However, the background processes for these states, which in most cases arise from $\gamma \to l^+l^-$, are experimentally indistinguishable from the signal and thus irreducible. Because the dark photons couple to the EM current, it is expected that the yield of γ_d is associated to the observed $\gamma \to l^+l^-$ yield by $n(\gamma_d \to l^+l^-) = \varepsilon^2 n(\gamma \to l^+l^-)\mathcal{F}(m_{\gamma_d})/2\Delta m$ with a small mass window Δm, and $\mathcal{F}$ is a known mass-dependent function [62].

Displaced Dark photon decays

Searches where the dark photon decay is displaced from the production point are able to largely overcome or even completely remove the background from prompt $\gamma \to l^+l^-$ decays. However, the dark photon lifetime scales as $[\varepsilon^2 m_{\gamma_d}]^{-1}$ and so this displaced decay signature may only be exploited for low masses and kinetic mixing strengths.

Invisible Dark photon decays

In the case where $m_{\gamma_d} > 2m_\chi$, the dark photon decay is predominantly invisible $\gamma_d \to \chi\bar{\chi}$ [61]. These can be searched for by either looking for an excess of events with a constant invariant mass which is formed from the imbalance of observed momentum and energy (missing energy), or through direct detection by searching for rare interactions of the dark-sector particles in a detector after the γ_d decay point.

Missing energy

Like many dark matter searches the missing energy method in experiments seeks to detect visible final state particles for individual interactions and search for an imbalance of energy and momentum. However neutrinos also give rise to missing energy signatures and there are substantial SM backgrounds from these processes. The initial state must also be accurately determined for these experiments, which is done by either directly measuring the energy and momentum of some initial state produced, or using information from the accelerator.

Direct detection

There are rare interactions of dark-sector particles in a detector downstream from the dark photon decay point which may be searched for. The dark photons are produced in the usual ways, which then decay to dark-sector particles through $\gamma_d \to \chi\bar{\chi}$. These dark particles may then be detected through scatterings of electrons and nuclei, from this scattering the dark particles emit a dark photon which in turn interacts with the detector particles due to its EM couplings, which lead to a detectable energy transfer.

2.2 Production and decay of the maverick top quark

We consider a new search strategy for a chimera-like scenario [63], where the dark photon arises from the decay of a hypothetical vector-like quark (VLQ) and not from standard SM particles. This hypothetical particle is the maverick top partner (abbreviated as VLT), which is a hypothetical heavy fourth generation quark [1]. The VLT is charged under both SM and a new gauge group $U(1)_d$, where the SM is neutral under $U(1)_d$.

The VLT may be produced through pair production ($T\bar{T}$), where T is the Maverick top quark, and single production (VLT produced in association with a jet ($T/\bar{T}+\text{jet}$)), shown in Figure 2.9. The pair production mode is induced by QCD interactions, giving that is relatively model independent as the production cross section is dependent only on the VLT mass M_{VLT}, the gauge coupling and its spin. However, the single production relies on the b-W-T coupling, where this coupling is proportional to the mixing angle $\sin\theta_L^t$. Thus the production cross section is suppressed for small θ_L^t and is proportional to $\sin^2\theta_L^t$. There is also a subdominant production $TW^- + \bar{T}W^+$, with an additional $SU(2)_L$ singlet scalar, a loop induced $T\bar{t} + \bar{T}t$ can be as large as the pair production [64].

At high masses, the single production has more importance, the gluon parton distribution function steeply drops and the $gg \to T\bar{T}$ is suppressed, as well the pair production is squeezed relative to single production. The single production can outperform the pair production in the case where the mixing angle is sizable $|\sin\theta_L^t| \gtrsim 0.1$ for a wide range of the VLT mass, M_{VLT}. But as the $t \to T$ mixing angle becomes significantly small, the single production vanishes, as this is required by perturbativity and the electroweak precision [1]. The search studied in this work focuses on single T production.

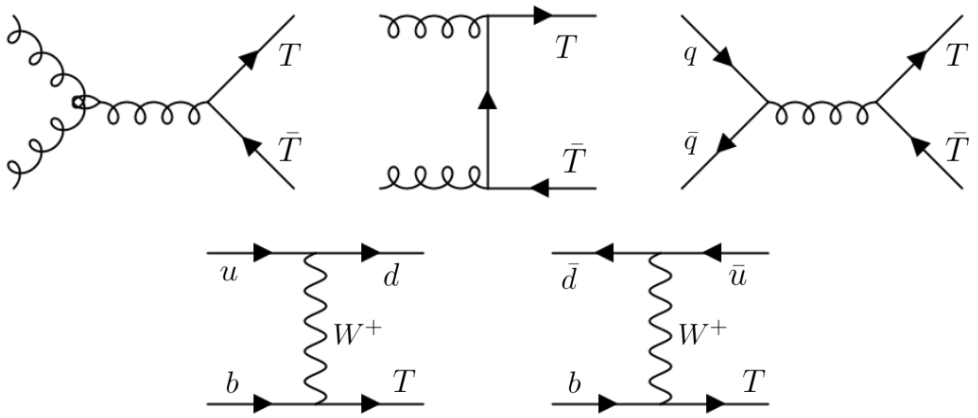


Figure 2.9: Standard VLT production modes for pair production (top) and single production with a jet (bottom) [1].

Traditional searches for the VLT have relied on $T \to tZ$, $T \to bW$ and $\bar{T}T \to th_1$. However, we consider a special production mechanism where the VLT decays to a SM top quark and dark photon, shown in the bottom left of Figure 2.10.

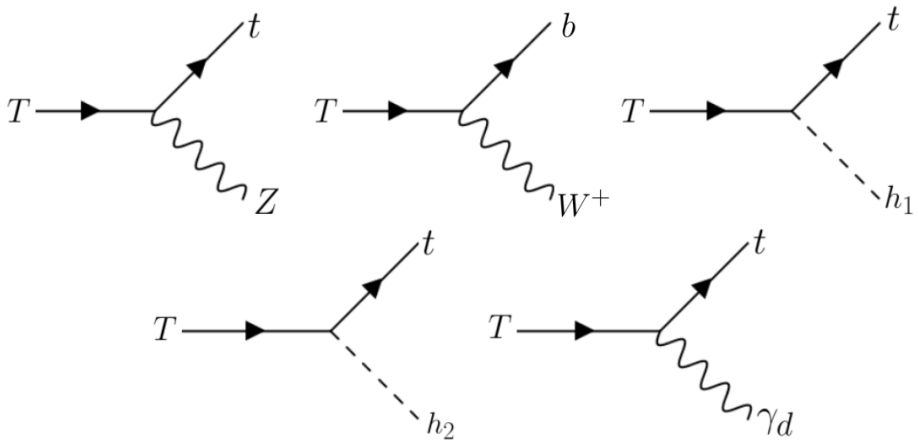


Figure 2.10: Representative Feynman diagrams for VLT decays to Zt, Wb, h_1t (top) and since T is charged under both the SM and $U(1)$, it can decay to h_1 and h_2. Where h_1 is the observed Higgs boson and h_2 is a new scalar boson.

2.3 Signal Model

The proposed model looks at the production of dark photons from the Maverick top quark with final states being an extremely high mass jet and a unique extremely low mass lepton jet [1]. While we typically look at jets from hadrons, two energetic and collimated photons or leptons can give rise to jet-like signatures in calorimeters as well [65, 66]. Dark photons can decay into such lepton jets, because the dark photon is light and boosted, the electron-positron pair produced when it decays will have very small opening angles. This makes the identification of individual electrons impossible and thus the signature will be a light but energetic jet containing both electron's energy deposits, which are the lepton jets [1].

This model probes the case where the maverick top quark decays to a SM top quark and a dark photon. As mentioned in section 2.1, we consider the case where the dark photon is massive, as well we look at the visible decay modes, where we require $m_{\gamma_d} > 2m_e \simeq 1$ MeV. As this will cause the decay to be into SM charged particles which leave a signature in detectors [63]. The dark photon produced decays to a lepton pair, however we choose to study the case where the dark photon decays only to an electron-positron pair as these final states are an unusual topology known as lepton jets which have been studied very little.

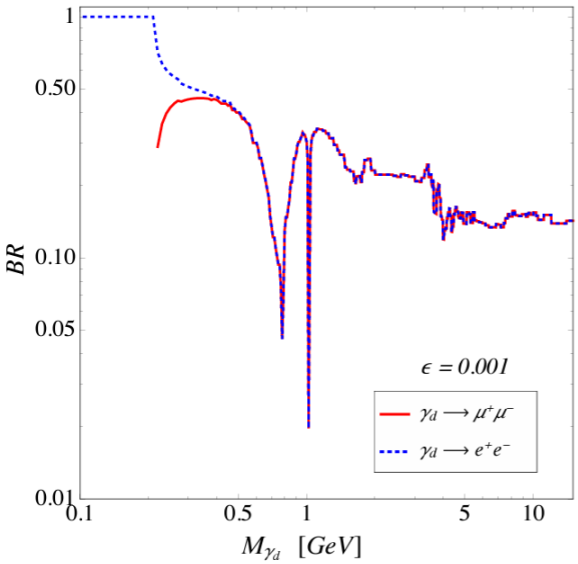


Figure 2.11: Branching ratios of γ_d as a function of its mass M_{γ_d}, into an electron-positron pair (e^-e^+) given by dotted blue line and muon-antimuon pair ($\mu^-\mu^+$) given by solid red line, where $\varepsilon = 0.001$ [1].

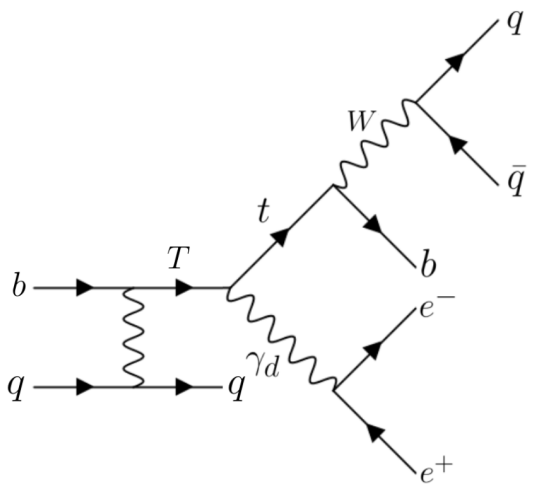


Figure 2.12: Feynman diagram showing the production and hadronic decay of VLT to a dark photon and top quark and the dark photon production from the VLT and its decay to a lepton jet.

For masses of γ_d below $\sim$ 200 MeV, the γ_d decay to muons is kinematically closed and the decay to an electron positron pair is dominant, thus the γ_d mass is constrained between 1 to 200 MeV. This ensures the branching ratio is 100% into the electron-positron pair and 0% for the muon-antimuon pair. The branching ratio dependence on the mass of the dark photon is shown in Figure 2.11 and the Feynman diagram for the signal is shown in Figure 2.12. Mass calibration for jets at such low values are unreliable in experiments, so exploiting the dark photons mass is infeasible. However the lepton jet produced from the dark photon is boosted and so the mass over transverse momentum ratio of these jets can be a useful and discriminating variable, even when taking into account the uncertainty of the measured mass value [63].

The standard jets from quarks and gluons, in general, have a higher mass compared to the hundreds of MeV in this signal. Experimentally, it is expected that the lepton jet will have a larger than usual fraction of energy deposited in the electromagnetic calorimeter, which may be exploited. The event will also contain a top quark decaying from the VLT and at least one more jet from the initial quark which is typically forward boosted. The topology of the event can be seen in Figure 2.13 from Ref [63]. The decay mode of the top quark determines the topology, there are two scenarios for these decay modes, the top quark decaying leptonically and hadronically separately. We consider the case in which the top quark decays hadronically. It is also important to note that in some events the initial quark produced along with the VLT may be a bottom quark and so it is expected that some events will have two b-tagged jets.

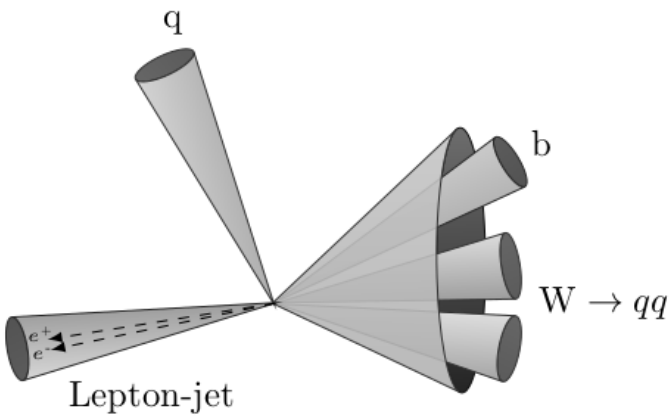


Figure 2.13: A diagram showing the final state configuration for a typical signal event in the hadronic channel. The large radius jet (J_{10}) originates from the top quark and includes three small radius jets (J_4) where one is b-tagged. One of the other two jets is the lepton jet candidate, which includes the electron-positron pair overlapping each other.

2.3.1 Event Generation

The signal events were generated using MadGraph5 interfaced with Pythia8 [67] (using the NN23LO1 parton distribution function set [68]) from the UFO [69] which is based on the maverick top partner model [1]. Pyhtia8 is a program used to simulate high-energy physics collisions categorized as a Monte Carlo Event generator. It is comprised of a coherent set of physics models for the evolution from a few-body hard process to a complex multi-hadronic final state [67]. It is used to model SM process outcomes in a detector and contains theory and models for a number of physics aspects, including hard and soft interactions, parton distributions, initial and final-state parton showers, multiparton interactions, fragmentation and decay.

For the maverick top model the free parameters are, the dark kinetic mixing parameter $\epsilon = 0.001$, the dark sector Higgs boson VEV, $v = 10$ GeV, the top-VLT mixing angle $\sin\theta_l^t = 0.1$, the dark Higgs boson mass $m_{H_d} = 10$ GeV, as well as the scalar mixing angle between the Higgs and dark Higgs boson given by $\sin\theta_S = 0.1$. The other two free parameters are the dark photon mass, m_{γ_d}, and the maverick top mass, M_{VLT}, where we varied the maverick top mass from 1 TeV to 5 TeV, having cross sections 47.6 fb and 0.0054 fb respectively, ensuring we remain at the phase space where it is produced singly.

The dark photon mass was chosen to be 100 MeV ensuring the branching ratio (BR) for e^+e^- is 1, as shown in Figure 2.11. For each signal mass, 100 000 events were generated and for each background process relevant, 1 million events were generated, all background processes were generated using PYTHIA8 [67]. A leading order generator is unable to model all the background accurately, however PYTHIA8 is adequate enough as our aim is to get the general characteristics of the background processes and determine ways to reduce them. All distributions shown are normalized using an integrated luminosity of 300 fb^{-1}, in correspondence with the projected integrated luminosity of combining LHC Run 2 and Run 3.

2.4 Analysis strategy

2.4.1 Overview

The main analysis strategy for this model is to search for the extremely high mass jet and a unique extremely low mass lepton jet, using model dependent events generated from PYTHIA8 and Rivet [70]. The main kinetic variables considered are the mass, the p_T and the invariant mass of the two jets of interest. Simulated events from MC generators are at particle level, so this makes it easier to resolve the required jets. From our model we know our final state objects are a massive jet originating from the top quark, a light lepton jet from the electron positron pair produced from the dark photon, and at least one additional jet. This means we can restrict our analysis to events with only 2 or less electrons and no muons.

For the jets, the jet clustering anti-k_T algorithm is used [25]. As mentioned in section 1.4.5, this is one of the most used jet algorithms as it starts off with the highest p_T input object and essentially absorbs softer input objects within a radius R_0. This leaves an approximately circular cone like jet object having area πR_0^2. Large radius jets have higher p_T, thus the massive top jet will use the anti-k_T algorithm where the radius parameter R_0 is 1.0 with $p_T > 150$ GeV and $|\eta| < 2$ which will be referred to as J_{10}. Since this is a particle level study without any pileup we have not implemented any grooming however applying soft-drop or standard trimming would have no effect on any conclusions made. For the light, small radius jets the radius parameter R_0 will be 0.4 with $p_T > 30$ GeV and $|\eta| < 4.4$, these will be referred to as J_4.

The massive top jet is a J_{10} and can simply be found by looking for the jet with the same mass as the top quark. Leptons are chosen to have $p_T > 25$ GeV and $|\eta| < 2.5$, are not originating from a hadronic decay and are dressed with photons within a radius of 0.1 (energies of all photons within a cone of $\Delta R = 0.1$ is added to the lepton). The missing transverse momentum is calculated as the negative four vector sum of all the visible particles. For this analysis the Rivet analysis toolkit [70] is used. The largest background contribution is from multijet processes, where a jet is mis-reconstructed as an electron, other significant background processes are semileptonic ($t\bar{t} \to l\nu q\bar{q}b\bar{b}$) and hadronic ($t\bar{t} \to q\bar{q}q\bar{q}b\bar{b}$) $t\bar{t}$. Other possible background processes are associated productions of $Z/W/\gamma$ with a top quark and jets, however their cross-sections are extremely small and as such are neglected.

2.4.2 Substructure Variables

Standard small radius jets are usually reconstructed with radius $R = 0.4$-0.6, however there are jets with even smaller radii, inside large radius jets, these are referred to as subjects or prongs. It is necessary to employ substructure techniques in this case as they are applicable for particles with high p_T. Although large radius jets in general originate from heavy resonances, they may also emerge from light quarks, gluons and charged leptons as in the case of our model. To characterise the large radius jet substructure and distinguish boosted objects from gluons or light quarks, tagging observables are constructed, often a combination of observables are used as taggers, but there are more complex algorithms [24]. One of these observables is N-subjettiness [71, 72], which categorises the amount of dominant directions of energy deposition inside the large radius jet, or how consistent it is with N or fewer subjets.

For example large radius jets from top quarks are expected to have at least three prongs, whereas large radius jets from the W, Z or Higgs bosons are expected to have at least two, and light quark/gluon large radius jets have no defined structure but most have only one prong. The τ_N variable is calculated using what is termed an exclusive jet algorithm, the constituents of the jet are clustered and require that exactly N subjets be found, the clustering stops at a specified number of jets and not at a predetermined jet radius. The variables τ_N are defined as the sum over all constituents k of the jet,

$$\tau_N = (1/d_0) \sum_{k=0}^{k=N} p_{T,k} \times \Delta R_{min,k}. \tag{2.2}$$

Where $\Delta R_{min,k}$ is the minimum distance of constituent k from the nearest subjet, the normalization factor d_0 is the sum of p_T of all constituents, multiplied by the jet radius which in turn ensures that $0 < \tau_N < 1$. Thus τ_N describes how well jets can be described as containing N or fewer subjets by assessing the degree to which constituents are aligned with the axes of the subjets for a given hypothesis N. The same argument holds for τ_{32} to identify three prong decay over two prong decay and τ_{21} to identify two prong decay over one prong decay. In this analysis we have considered τ_{32} and τ_{21} shown in Figure 2.14.

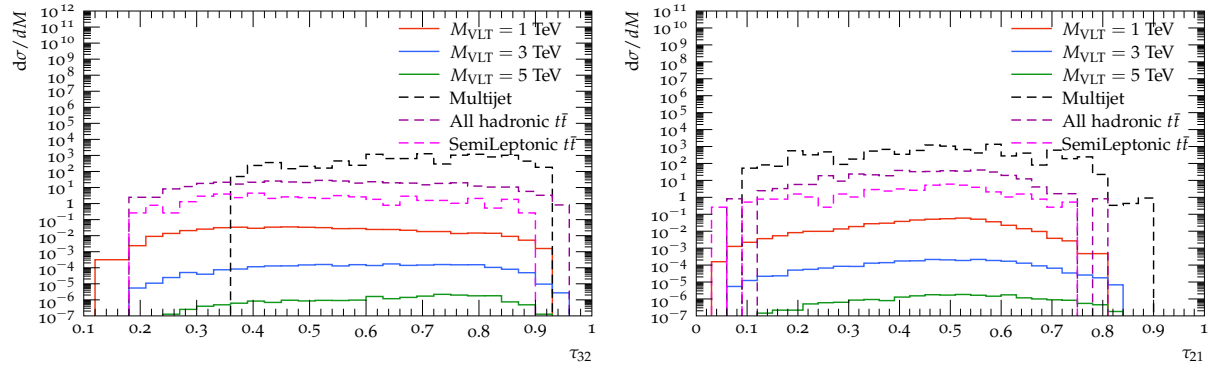


Figure 2.14: Plot showing τ_{32} (left) and τ_{21} (right) distributions for signal for the three masses considered, corresponding to VLT masses of 1, 3 and 5 TeV, with the dominant background processes shown.

Another algorithm which has been considered in order to characterise large radius jet substructure is energy correlation functions (ECF) [73, 74] shown in Figure 2.15. The angular distribution of subjets inside large radius jets is sensitive to how the jet was formed (the internal radiation structure). Using the jet constituents the relevant ECF are defined as follows,

$$\mathrm{ECF}(N,\beta) = \sum_{allN} \Big(\prod_{a=1}^{N} p_{T_a}\Big)\Big(\prod_{b=1}^{N-1}\prod_{c=b+1}^{N} R_{ib}R_{ic}\Big)^{\beta}. \tag{2.3}$$

The parameter β allows sensitivity to different angular scales, for this analysis ECF2 and ECF3 were examined which are defined by:

$$\mathrm{ECF}(2,\beta) = \sum_{i<j} p_{T_i}p_{T_j}(R_{ij})^{\beta} \tag{2.4}$$

$$\mathrm{ECF}(3,\beta) = \sum_{i<j<k} p_{T_i}p_{T_j}p_{T_k}(R_{ij}R^{jk}R^{ki})^{\beta} \tag{2.5}$$

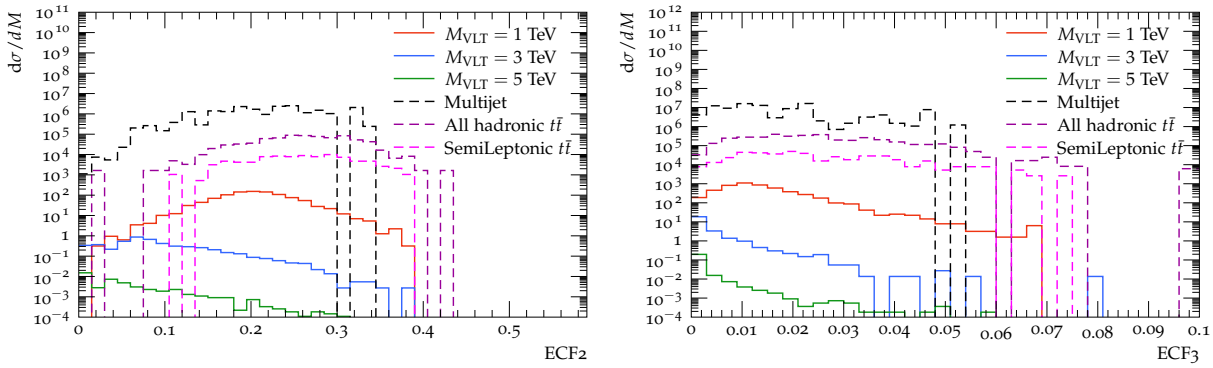


Figure 2.15: Plot showing ECF2 (left) and ECF3 (right) distributions for signal for the three masses considered, corresponding to VLT masses of 1, 3 and 5 TeV, with the dominant background processes shown.

Similar to the τ_N variables the ECF variables behave such as to identify the N-prong substructure and stops at the specified number of jets, if there are only N constituents, then ECF$(N+1)$ will tend to zero. A more general consideration is for N-prong substructure, ECF$(N+1) <$ ECF(N), thus we may define the ECF ratios as,

$$r_N = \text{ECF}(N+1)/\text{ECF}(N). \tag{2.6}$$

It has been found however that the double ratios of ECFs have more discriminating power which are defined by (for specified values of β):

$$C_N = r_N/r_{N-1} = \frac{\text{ECF}(N+1)\text{ECF}(N-1)}{\text{ECF}(N)^2} \tag{2.7}$$

The energy correlation double ration C_N distinguishes higher order radiation from leading order (LO) substructure. This means for a system of N subjets then the LO substructure will consist of N hard prongs. Thus if C_N is small then the higher order radiation in respect to the LO substructure is soft and collinear. However, if C_N is large, then this means the high order radiation with respect to the LO substructure is not strongly collimated and in fact there are more than N subjets in the system. This is advantageous as if C_N is small but C_{N-1} is large, then it is an indication the larger-radius jet will have at least N subjets.

However, the C_N variables are not lorentz boost-invariant, this is addressed by D_N observables. The constructions of C_N and D_N are what is referred to as power counting [75]. Where the ECF observables are used as a basis and constructed to amplify specific features of the large radius jet these substructure variables are shown in Figure 2.16.

The variable D_N is constructed as follows (for specified values of β):

$$D_N = \frac{\mathrm{ECF}(N+1)\mathrm{ECF}(N-1)^3}{\mathrm{ECF(N)}^3}. \tag{2.8}$$

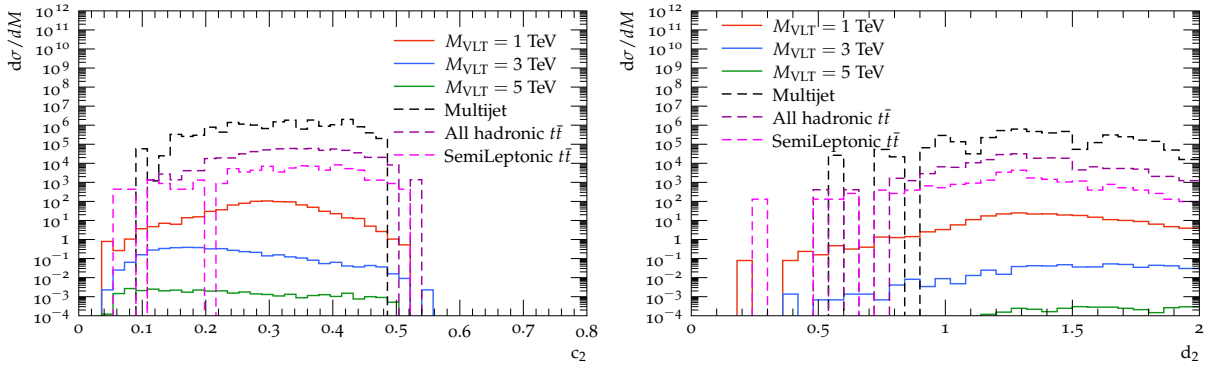


Figure 2.16: Plot showing C_2 (left) and D_2 (right) distributions for signal for the three masses considered, corresponding to VLT masses of 1, 3 and 5 TeV, with the dominant background processes shown.

The final substructure variable considered is the Les Houches Angularity (LHA) [76, 77], where the generalised angularities for a jet are defined by,

$$\lambda_\beta^\kappa = \sum_{i \in jet} z_i^\beta \theta_i^\kappa \tag{2.9}$$

z_i is the momentum fraction, and the (normalized) angle of the ith constituents of the jet is given by $\theta_i = \frac{R_i}{R_{jet}}$. The exponents κ and β are used to probe different aspects of the jet fragmentation. For $\kappa = 0$ and $\beta = 0$, (0,0), the multiplicity of the constituents are simply reduced, and $\kappa = 2$ and $\beta = 0$ is effectively the squared sum of the transverse momenta of the constituents which is referred to as p_T^D. As well, if we were to consider (1,1) and (1,2), these are analogous to jet shape observables such as mass or broadening. The LHA, shown in Figure 2.17 is the variant whereby $\kappa = 1$ and $\beta = 0.5$ (1,0.5).

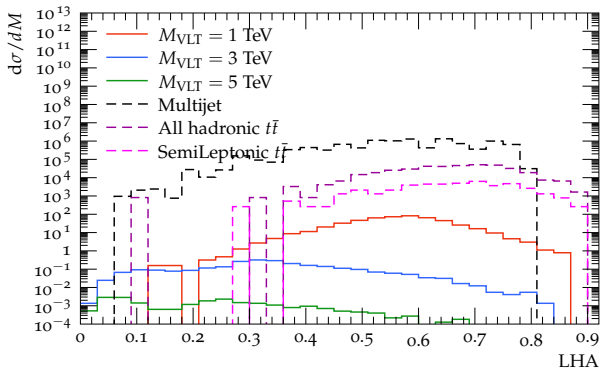


Figure 2.17: LHA distribution for signal for the three masses considered, corresponding to VLT masses of 1, 3 and 5 TeV, with the dominant background processes shown.

Considering all plots given, it is clear the substructure variables are not a feasible approach in significantly reducing the background contributions. Thus, other variables must be explored.

2.4.3 Analysis of dark photon with the heavy-top quark decaying hadronically

The signal topology is two electrons being identified as one, a low mass lepton jet and a boosted top quark resulting in a top jet and at least one other jet. The event selection is muons, at least one electron, at least three J_4s, and minimum one J_{10}. Where one of the J_4s needs to be the lepton jet candidate. The initial quark produced with the VLT may be b-tagged, and from Figure 2.18 we see that the b-jet multiplicity peaks around 2, thus at least one J_4 must be b-tagged.

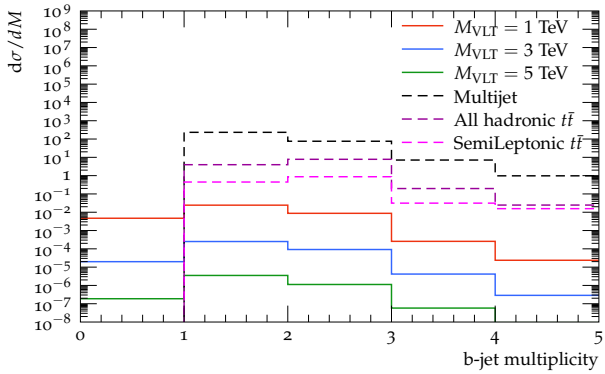


Figure 2.18: Number of b-jets for signal for the three masses considered, corresponding to VLT masses of 1, 3 and 5 TeV.

The lepton jet is the result of the electron-positron pair produced having an extremely small opening angle, this means we can find the light lepton jet as it must be the jet closest to the leading electron. Hence, the jet and leading electron with the smallest angular separation ($\Delta R = \sqrt{\Delta\eta^2 + \Delta\phi^2}$ where η is the pseudorapidity and ϕ is the azimuthal angle) must be the lepton jet. This is verified by checking the ΔR between the two electrons and between the leading electron and closest J_4, given by Figure 2.19.

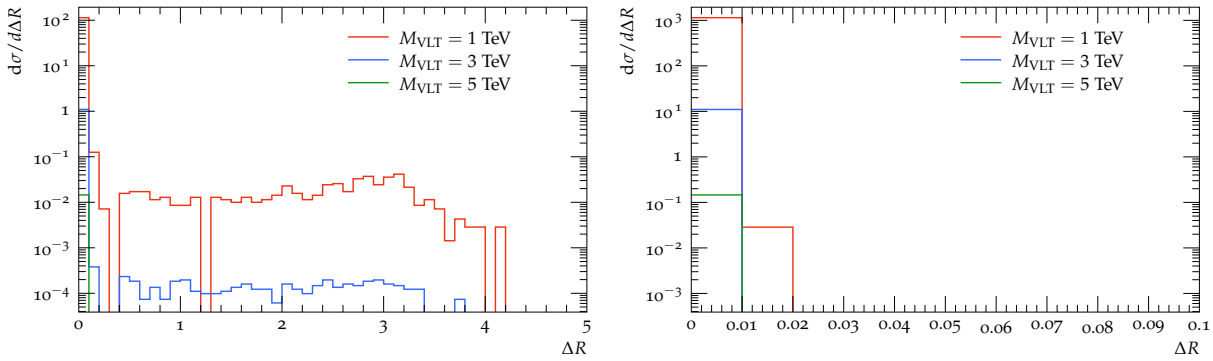


Figure 2.19: Distributions for ΔR between the leading electron and the closest J_4 (left) and ΔR between the two electrons originating from the dark photon (right) for the three masses considered, corresponding to VLT masses of 1, 3 and 5 TeV.

From Figure 2.19, we see the two electrons are extremely close, almost on top of eachother, as expected and there is a J_4 which is always collinear with them. We require only one electron instead of two as this ensures we are consistent with the experimental signature. However, since our study is at particle level this requirement is relaxed for multijet and hadronic $t\bar{t}$, as these reducible backgrounds come about from jets misidentified as electrons. Thus, at particle level there will be no electrons and as such there is no requirement on the number of electrons for these backgrounds.

To mimic this electron misidentification rate, the cross-sections have been scaled to 0.1, this conservative estimate is derived from Ref [78]. The highest mass J_{10} will be the top jet candidate with a top mass window requirement chosen generously to be between 125 and 225 GeV. It is also required that the J_{10} contains a b-tagged J_4 within $\Delta R < 1$. Since the multijet and hadronic $t\bar{t}$ events will not have a real electron but a jet misidentified as an electron, the lepton jet is chosen as the J_4 farthest from the top jet candidate as they are expected to be back to back. This is not always true for a small percent of cases from the dark photon mass distribution in Figure 2.20. The invariant mass of the VLT top partner is reconstructed from the four-momenta of the top jet and lepton jet candidates.

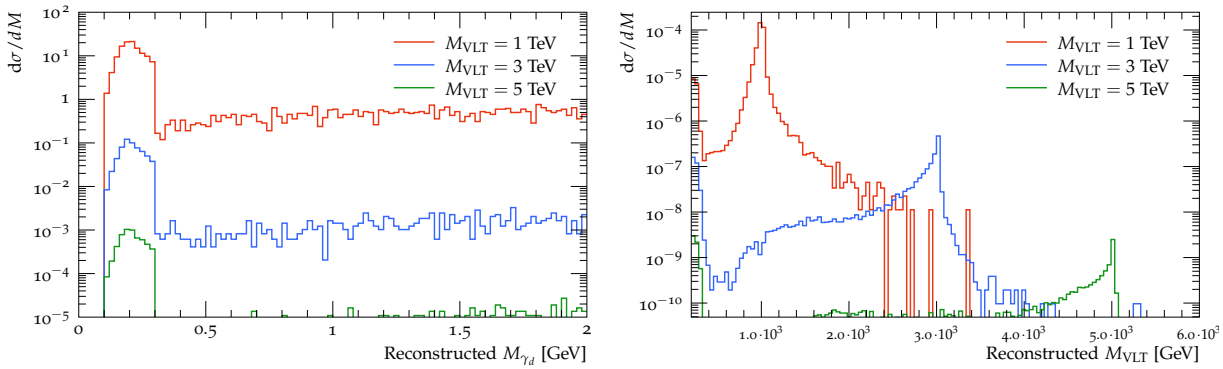


Figure 2.20: Distributions of the mass for the lepton jet candidate (left) and invariant mass of the lepton jet and top jet candidates (right) for the three masses considered, corresponding to VLT masses of 1, 3 and 5 TeV, with the dominant background processes shown.

The invariant mass of the heavy top-quark jet and the light lepton jet shown in Figure 2.20 have a peak around 1, 3 and 5 TeV respectively corresponding the the VLT masses considered, which can be recognized as the mass of the hypothetical Maverick top quark in the model. As well the light lepton jet mass distribution has a peak around 100 MeV which will be seen in the detector and is the mass of the dark photon jet in this model. Hence, from considering the mass plots, it can be seen that the Maverick top quark and the dark photon can be reconstructed with our analysis strategy. As well from the p_T and mass plots, in Figures 2.20 and 2.21 it is clear the Maverick top quark and dark photon are boosted as discussed. Although attempting to find the signal in a detector for a process such as this can be challenging a further strenuous task is finding this signal amidst a large background. As mentioned there will be background contributions from semileptonic and hadronic $t\bar{t}$, however the biggest challenge and largest background will be contributions from multijets.

Kinematic selections in order to reduce background contributions are made based on signal characteristics. In Figure 2.21 we see the lepton jet and top jet p_T distributions, from these plots, a minimum 200 GeV requirement is utilised. As well the lepton jet and top jet are expected to be more back to back in the azimuthal co-ordinate than most background processes and so based on Figure 3.4, $\Delta\phi$ between the lepton jet and top jet is required to be $\Delta\phi > 1.5$.

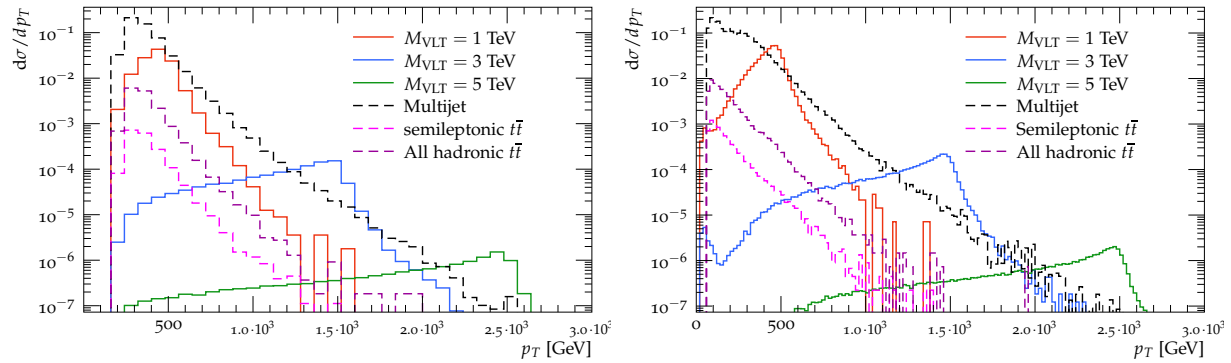


Figure 2.21: Distributions of the p_T for the top jet candidate (left) and the lepton jet (right) for the three masses considered, corresponding to VLT masses of 1, 3 and 5 TeV, with the dominant background processes shown.

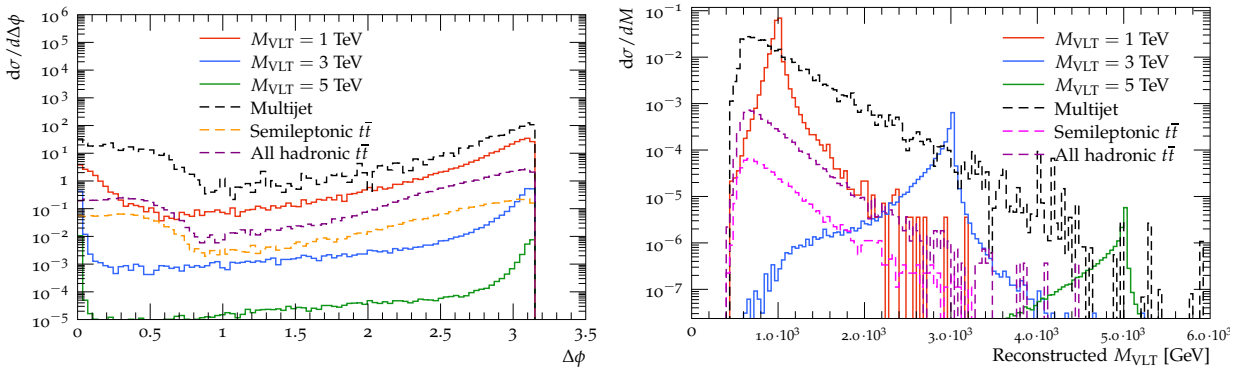


Figure 2.22: $\Delta\phi$ between the lepton jet and top jet (left) and the invariant mass of the VLT top partner is reconstructed from the four-momenta of the top jet and lepton jet candidates (right) for the three masses considered, corresponding to VLT masses of 1, 3 and 5 TeV, with the dominant background processes shown.

We see in Figure 2.22, showing the reconstructed VLT mass, that after all kinematic requirements mentioned above, a significant amount of background still remains. However, considering the mass over transverse momentum ratio, m/p_T, which is given in Figure 2.23, we can require the ratio to be less than 0.01.

2.5 Results

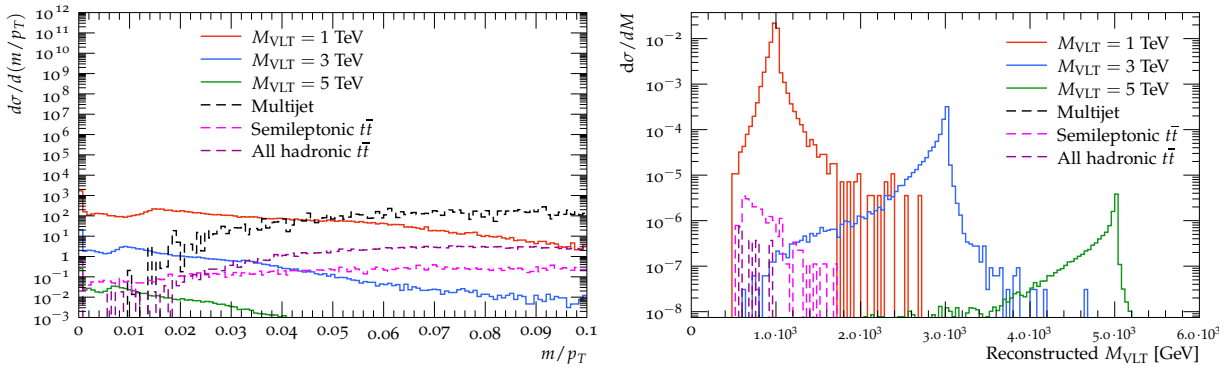


Figure 2.23: Distributions of the lepton jet candidate m/p_T ratio before applying $m/p_T > 0.01$ requirement (left) and VLT reconstructed mass after applying this requirement (right) for the three masses considered, corresponding to VLT masses of 1, 3 and 5 TeV, with the dominant background processes shown.

Looking at Figure 2.23 we see that applying the lepton $m/p_T > 0.01$ ratio requirement, significantly reduces the background, essentially keeping only signal. The effect of these kinematic requirements on the signal and background efficiency is given in detail, presented in table 1.

Requirement	Signal efficiency reduction for VLT mass in %:		
	1 TeV	3 TeV	5 TeV
Lepton multiplicity	97	98	98
J_4 and J_{10} multiplicity	93	94	92
Top mass window	75	79	71
b-jet multiplicity	68	75	68
Lepton jet p_T	64	73	67
Top jet p_T	64	73	67
b-jet containment	57	57	41
Lepton jet and top jet separation	56	56	40
Lepton jet m/p_T	17	29	27

Table 1: Effect on signal efficiency of kinematic requirements corresponding to VLT masses of 1, 3 and 5 TeV. The numbers represent the percentage of events remaining after each requirement, where individual requirements are mentioned in the text. For the lepton jet identification, there will always be a jet close to the lepton jet and opposite it.

Although the enforced requirements significantly reduce the signal, requiring that $m/p_T > 0.01$ substantially reduces the background as well, almost entirely making it a zero background search.

An interesting observation is that although the m/p_T requirement is less efficient for higher VLT masses, the signal efficiency is better for the intermediate VLT mass than the higher masses, this is because the jets are more boosted at higher VLT masses. Since the jets are more boosted this also means that the requirement, $\Delta\phi > 1.5$ between the lepton jet and top jet will also be less efficient at higher masses. For an integrated luminosity of 300 fb^{-1}, after all selections, we have 2380 signal events remaining for the 1 TeV VLT mass, 35 signal events for the 3 TeV mass and less than 1 event for the 5 TeV mass, thus the 5 TeV signal is inaccessible.

Of course this may be an idealistic assumption as it is a particle level study and mis-measurements and detector effects will result in a non-zero background. We know we can expect at least three signal events [79, 9]. Thus this allows an estimate of the integrated luminosity that would be needed as a function of the VLT mass, excluding the signal if no events are observed. Considering the minimum integrated luminosity needed in order to exclude VLT mass points shown in Figure 2.24, we see that LHC Run 2 data may already be sufficient enough to have the sensitivities needed up to a VLT mass of 3.5 TeV.

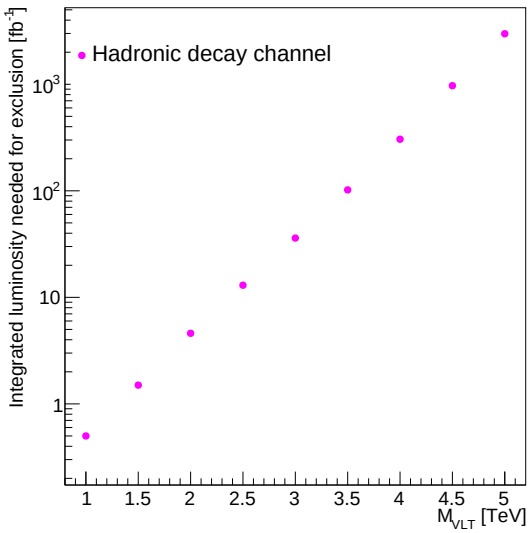


Figure 2.24: The minimum integrated luminosity needed in order to exclude VLT mass points, if no events are observed, be we can expect at least three signal events.

2.6 Conclusion

The hypothetical massive dark photon is considered, where a unique collider topology of a Maverick top partner model decaying to a dark photon. The final state is a boosted top quark, one other jet and a lepton jet, which have been studied sparingly at the LHC. A phenomenological study of the model has been explored. A search strategy has been proposed, a set of kinematic selections, based on signal characteristics, were applied. Although initial selections had little effect on reducing background, the discriminating m/p_T ratio was introduced, which greatly reduced the background while still leaving sufficient signal for VLT having masses 1 and 3 TeV. We see that estimating the minimum integrated luminosity which is needed to exclude VLT mass points, the search is viable up to a VLT mass of 3.5 TeV with current available LHC data.

3 Dark Matter searches using semi-visible jets

There are a number of considerations which may motivate the search for strongly-coupled dark sectors at the LHC. Because of baryon asymmetry, an abundance of visible matter arises, this may be the case for dark matter as well, where a similar mechanism may explain the abundance of dark matter observed in our universe [80]. Cosmological measurements of the dark matter density have been identified to be similar to visible matter, however, approximately five times larger [27]. This points to the idea that dark matter may consist of composite particles, and in some scales, the new confining force. This is referred to as dark QCD, which is a "simple imitation" of SM QCD [81] in the dark sector, which favours dark QCD scales of the order of 10 GeV and mediator masses in the TeV scale. In general terms, these models have the ability to produce the correct DM relic density [82].

3.1 QCD-like dark sector

It is assumed that the dark sector communicates with the SM via a so-called portal, the SM allows three renormalizable portals. In that, there are then three SM gauge singlet operators whose mass dimension is less than four. The dark sector can couple to the Higgs bi-linear $|H|^2$ [83], the neutrino via the singlet operator $H\,L$ (constructed from the Higgs and lepton doublets) [84], or to the field strength of the Hypercharge gauge boson $B_{\mu\nu}$ [85]. There has been focus on a new mediator particle, Z' [86], which may serve as a portal and mediate s-channel production. Via this portal dark sector particles may be produced at hadron colliders, as in a similar fashion of SM quarks, dark quarks may shower and hadronise to form dark jets. The properties of these dark jets are determined by the dynamics of the dark sector. In particular, the mass scale of the dark hadrons, the coupling strength and the ratio of unstable to stable dark hadrons inside the dark jets. The dark hadron final states may contain, to name a few, lepton jets, emerging jets or semi-visible jets depending on the lifetime of the dark hadrons. Assuming that the s-channel portal couples the dark sector to SM quarks, then the observables of interest are jets and MET aligned to these jets. Pairs of quarks can be produced via a heavy resonance Z', which also couples to SM quarks via [86],

$$\mathcal{L} \supset Z'_{\mu}(g_q \bar{q}_i \gamma^{\mu} q_i + g_{\chi} \bar{\chi}_{\alpha} \gamma^{\mu} \chi_{\alpha}). \tag{3.1}$$

q are SM fermions, χ are dark sector quarks and $g_{q,\chi}$ are the respective coupling constants.

The term $Z'\bar{q}\gamma g$ will later be called the SM current J_{SM}. Z' may also couple to various other SM particles, however, we limit ourselves to Z' coupled with quarks, focusing then on dark showers resulting in SM jets and MET signatures. Heavy resonances Z' can be produced at hadron colliders through Drell Yan processes, having a non-trivial branching ratio to decay to two dark quarks. These dark quarks then decay back to SM particles, which then shower and hadronise as usual. The main parameters governing these s-channel models are the Z' mass, denoted $m_{Z'}$, and its couplings to the visible and dark quarks g_q and g_χ, the characteristic scale of the dark hadrons m_χ, the fraction of stable hadrons aligned with the visible jet, and the dark sector shower. Where the dark sector shower is governed by the scale of the dark sector confinement, denoted Λ_d, and the number of dark colours and flavours. The Z' production cross-section is determined by the coupling to SM quarks and the other parameters determining the final state. The number of dark matter particles produced in the dark shower impacts the amount of missing transverse energy, this effect is parameterised by the fraction of stable and unstable invisible dark hadrons, given by $r_{inv} = N_{stable}/N_{total}$ [87, 86]. The value of this stable to unstable dark hadron fraction determines the dark jet signature, a schematic is shown in Figure 3.1.

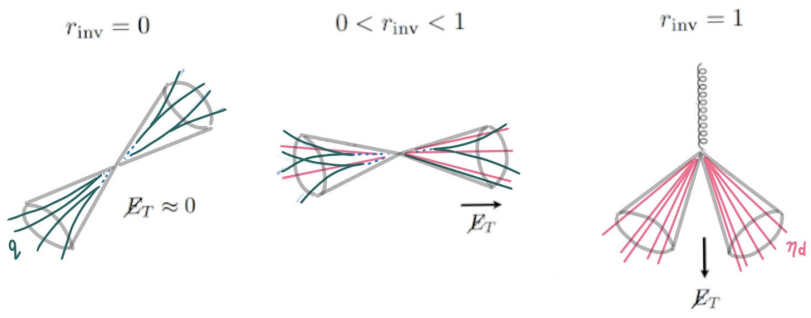


Figure 3.1: Diagram showing the jet topology and MET direction for different r_{inv} values, where the green lines are visible particles and the red are invisible.

There are two main strategies to search for these model signatures [88], which have a large dependence on the value of r_{inv}. For the case where r_{inv} is small a general bump hunt strategy can be employed as most of the final state associated with the resonance is visible. For larger intermediate values of r_{inv} it is ideal to perform a bump hunt using the scalar transverse mass variable, $\not{E}_T$, given by,

$$M_T^2 = M_{jj}^2 + 2(\sqrt{M_{jj}^2 + p_{Tjj}^2}\not{E}_T - \vec{p}_{Tjj} \cdot \not{E}_T). \tag{3.2}$$

When r_{inv} approaches one, the final states are majority missing energy and the "mono-jet" and MET search strategy is most sensitive, where the single jet arises from the ISR.

3.1.1 Semi-visible jets

A search for semi-visible jets is performed, where semi-visible jets (svj) [89, 88, 90] are jet-like objects, the visible states in the shower are Standard Model hadrons. In these scenarios it is assumed that the hidden sector contains some families of dark quarks where at energies below a dark-confinement scale, Λ_d, these dark quarks bind into dark hadrons [91]. A non-WIMP scenario leading to a unique collider signature has been proposed in Ref [88], these dark quarks decay and hadronise to stable and unstable quarks, the unstable quarks then decay to SM quarks. The total momentum of the dark matter will be correlated to the momentum of the visible states, this will lead to a signature with missing transverse energy MET aligned with a jet.

The dark sector contains many flavours of dark quarks $(\chi_1, \chi_2, \chi_3, ...)$ which form bound states referred to as dark hadrons, these dark hadrons may be stable or unstable. The unstable dark hadrons decay promptly to SM quarks, however the stable dark hadrons are the DM candidates and pass the detector without interacting. This leads to a collimated mixture of visible and invisible particles, which are termed as semi-visible jets. Thus, the signature will be a pair of jets where one of the jets is aligned to the MET, and the amount of missing transverse energy is expected to be moderate, because both of the jets contain visible particles, a portion of the transverse component of the overall MET will cancel out when the jets are produced back to back.

The parameter r_{inv} can have a value between 0 and 1 and since events containing jets aligned with missing transverse momentum are explicitly rejected from the signal regions of existing collider DM searches, a large portion of the parameter space of this model has not yet been covered. In particular events with intermediate values of r_{inv}. Current DM searches are more sensitive to dark sector models having an $r_{inv} \approx 1$ yielding events having high missing energy and some initial-state radiation [88]. Note that current dijet searches favour dark sector models having $r_{inv} \approx 0$, which yield events having two jets but low missing energy [92]. Thus this search supplements these efforts. Alternative scenarios for dark matter are Hidden Valley (HV) theories [90] which propose dark sectors with potentially multiple new particles and new forces which are decoupled from the SM except for the mediator particles. The dark sector may contain a new confining force analogous to that of QCD in the SM. These models are of interest as they are relatively unexplored experimentally but may present a range of novel kinematic signatures as they generate dark showers [93].

3.1.2 Hidden Valley models

The term "Hidden Valley" refers to the presence of a low mass "valley" having $d-$states (d-quarks and d-hadrons) which are only observed by passing over or through a mass barrier which separates the standard model sector from the hidden sector. The phenomenology of the HV arises due to the non-trivial dynamics of the hidden sector as well as the low mass of the d-particles. The d-hadron masses are determined by either the confinement scale Λ_d or the $d-$quark mass, depending on whichever is larger. The lower $d-$hadron mass bound however, is derived by requiring that it decay before Big-Bang Nucleosynthesis (BBN), thus the precise constraint is dependent on the operator mediating communication dimension between the standard model and hidden sector, but typically it will be sub-GeV.

The effects of a HV on our SM observable sector is determined crucially by the mediator nature [94, 90]. Due to the apparent large gap between the heavy mediators and the d-sector particle masses, this gives rise to a barrier between the HV and SM, which in order to produce these valley particles via SM processes, must be overcome. Integrating out the mediator, the generic form of the effective operator is given as follows:

$$g_d G_{\mathrm{SM}} \frac{\mathcal{O}_d \mathcal{O}_{\mathrm{SM}}}{M^k}, \tag{3.3}$$

where the mediator mass is given by M, the mediator couplings to the two sectors are g_d and g_{SM} and the power of suppression denoted by k is dependent on the mediator as well as the nature of the hidden sector. When the d-sector quarks are produced through the mediator, they confine into d-hadrons, in the case where the mediator mass is much larger than the d-hadrons, many d-hadrons are produced during d-sector hadronisation. If the hidden sector resonances are not too light and the mass gap not too low, the d-hadrons will then decay to combinations of leptons and quarks back through the mediator. When summed together, since the d-hadron itself carries no SM charges, these quarks and leptons are neutral under SM. This gives that the d-hadrons may decay to heavy quarks, light quark jets or neutral pairs of leptons, however, the decay to spin-one resonances tend to be equal among SM fermions [95].

Hidden gauge groups

It is assumed that the HV consists of a new gauge group G, which is presumed to be a $U(1)$ or $SU(N)$ group [96]. Since HV is a light hidden sector, the masses of its associated particles may be as low as 10 GeV, with the spectrum and dynamics of these particles depending on the gauge group G, along with their group representations, as well as their spin and number of particles contained in the theory. There are 12 fundamental charged particles under both the HV and SM symmetry groups. The hidden valley particles are essentially mirrored particles of the SM sector. These particles have a fundamental representation in HV colour symmetry and couple flavour-diagonally with the corresponding SM state, which we haven't detected yet as we haven't fully explored the full available phase space in existing searches. These particles, collectively referred to as F_d, are given below in table 2.

SM particle	Corresponding HV particle
d (down quark)	D_d
u (up quark)	U_d
s (strange quark)	S_d
c (charm quark)	C_d
b (bottom quark)	B_d
t (top quark)	T_d
e (electron)	E_d
d_ν (electron neutrino)	ν_{E_d}
μ (muon)	Mu_d
ν_μ (muon neutrino)	ν_{Mu_d}
τ (tau)	Tau_d
ν_τ (tau neutrino)	ν_{Tau_d}

Table 2: 12 fundamental HV particles charged under the HV and SM symmetry groups.

There is also a set of fundamental particles charged only under the new gauge group which are collectively referred to as q_d [96], it may be either a boson or fermion and is considered to be stable. In the case of abelian $U(1)$ gauge symmetry, there is a photon-like gauge boson, denoted by γ_d, which is radiated by the q_d such that $q_d \to q_d\gamma_d$. For unbroken $U(1)$ symmetry the invisible HV particles have no SM couplings and thus can only be detected through observations of missing transverse momentum. In order to have visible decays from the HV, this gauge group must be broken as otherwise q_d will not decay and subsequently neither will the radiated particles. From the broken gauge group, it can also be assumed that there is some kind of mixing between ordinary SM photon and γ_d, giving to a γ_d into fermion pairs with mass γ_d, similar to that of an off-shell photon, where the lifetime is dependent on the mixing angle.

Considering the case of a non-abelian $SU(N)$ gauge symmetry, the gauge bosons, now denoted by g_d, will self-interact, and in the case where $SU(N)$ symmetries remain unbroken, will give rise to massless gauge bosons where the interaction strength will not fall off at greater distances as well giving to a parton confinement analogous of that in QCD. In this scenario there will also be radiation with, $q_d \to q_d g_d$ as well $g_d \to g_d g_d$.

This confinement leads to the g_d and q_d hadronising to objects which are similar to mesons and hadrons. We can obtain the q'_ds and $\bar{q}'_d$ as depending on the mixing of states, they can remain stable or decay back to SM. If it is off-diagonal and flavour charged then the q'_ds may exist as invisible and stable states, however diagonal ones will contribute to the production of visible hadrons as they decay back to SM. Thus this model generates invisible particles, but some signals decay back to the standard model.

Hidden Valley shower

Pyhtia8, described in section 2.3.1, is useful tool and works well for SM processes, however we want to consider models with beyond the standard model (BSM) interpretations, which in many BSM models contain sectors of new matter content and gauge groups which at lower energy limits can decouple from SM.

Thus the Hidden Valley module of Pythia8 was designed to allow the study of a sector decoupled from the SM [95, 97]. It began with the simple motivation that, while maintaining cosmological bounds, one could began with a number of gauge groups and as energy is decreased break them down to fewer groups. The normal time-like QCD and QED showering has been extended by the HV sector as the HV module appears to give a fairly generic framework for the study of BSM models.

From the g_d and q_d production mechanisms mentioned in section 3.1.2, there are three alternative production mechanisms. There is the possibility of kinetic mixing terms, whereby we have $q\bar{q} \to \gamma \to \gamma_d \to q_d \bar{q}_d$. In the s-channel, a massive Z' may act as a mediator such that, $q\bar{q} \to Z' \to q_d \bar{q}_d$. The final possible production mode is the presence of a F_d, charged under both SM and HV symmetry groups, giving rise to a production scheme where by $gg \to F_d \bar{F}_d$. Where F_d can then subsequently decay to a q_d and SM particle, $F_d \to f q_d$.

As discussed from the broken $U(1)$ symmetry, the HV photon acquires mass and then decays to ordinary photons which create pairs of SM particles. However, for $SU(N)$ symmetry the HV photon hadronises in the hidden sector with full string fragmentation setup, producing 64 $q_d q_d$ mesons and up to 8 flavours of q_d, where the masses are assumed to be degenerate. Depending on the theory at hand, the user may specify the meson masses and decay mechanisms accordingly. The HV particles are permitted to radiate and from the production mechanisms mentioned, these HV particles are not produced in initial state radiation (ISR). The HV radiation is akin to that of QCD, as all the (anti)particles q_d and F_d have a single, negative, unit of HV charge. Thus, interleaving the showering mechanism for the three radiations, HV, QCD and QED. However, it is a challenge separating one kind of radiation from another as the emission arrangement is one common sequence of decreasing emission p_T scales.

Of course if the HV particles have no SM couplings they can only be detected through observations of missing transverse momentum as they are invisible. There are two possible ways of simulating scenarios whereby activity in the hidden sectors may flow through to the visible sector, constituting missing transverse momentum. The first scenario is the case of $U(1)$ symmetry breaking, where as mentioned the HV photon will acquire mass and since it has a small but non-zero mixing angle with the ordinary photon, through some mediator (for example, the Z') and subsequently decays back to SM particles. However, the q_d has no confinement in the $U(1)$ symmetry and thus remains undetected. The second scenario is a case already discussed in section 3.1.2 where the $SU(N)$ gauge group remains unbroken and the q'_ds and $\bar{q}'_d$ can exist as stable and invisible states or decay back to SM particles, contributing to the production of visible hadrons.

The Pythia8 HV module allows the existence of visible jets, even though the constituents came from the hidden sector, the final state is like that of an ordinary QCD jet. It allows invisible jets, where the HV particles only contribute to MET as they are completely stable. As well, it supports semi-visible jets, where we have a jet aligned with MET, as the unstable dark hadrons decay back to SM particles while the remaining are stable within collider time scales and traverse the detector. The Pythia8 HV module is a powerful tool and there are different possible final states which can arise from exploiting it, this is shown by figure 3.2.

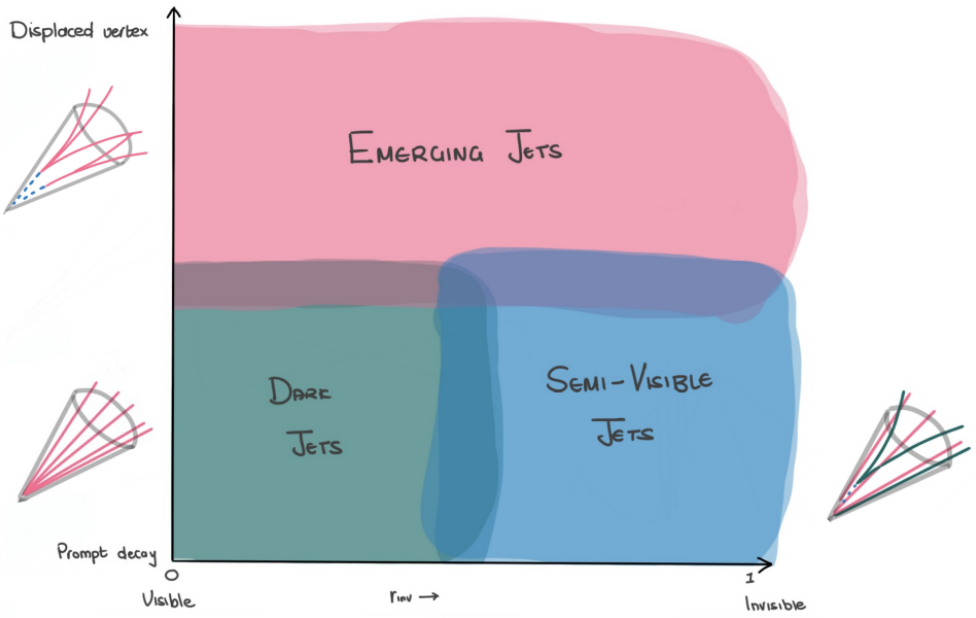


Figure 3.2: Diagram showing a basic classification of jets with respect to decay distance from vertex and different r_{inv} values.

3.2 Signal model

We consider the resonant production process where two quarks decay to a leptophobic Z' boson mediator giving two dark quarks, $q\bar{q} \to Z' \to \chi\bar{\chi}$ [87]. The leptophobic Z' boson mediator arises from a broken U(1) symmetry, with couplings to SM quarks g_q and dark quarks g_χ.

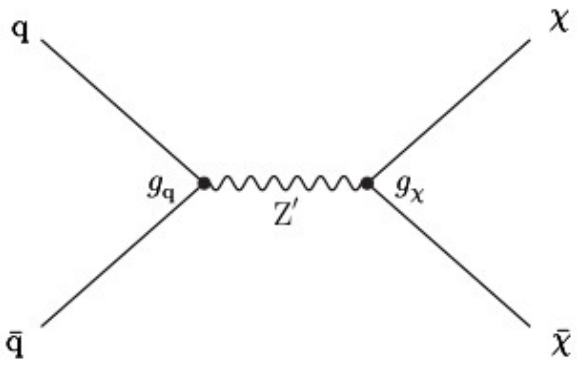


Figure 3.3: Feynman diagram of the leading-order resonant production of dark quarks through a Z' mediator, with relevant couplings to SM quarks (g_q) and dark quarks (g_χ) indicated at the vertices.

The leptophobic Z' gauge boson couples to the SM baryon current J^{μ}_{SM} and the dark quark current J^{μ}_{χ} [89]:

$$\mathcal{L} \supset \frac{1}{4} Z'^{\mu\nu} Z'_{\mu\nu} - \frac{1}{2} M^2_{Z'} Z'_{\mu} Z'^{\mu} - g_q^{SM} Z'_{\mu} J^{\mu}_{SM} - g_{\chi} Z'_{\mu} J^{\mu}_{\chi}. \tag{3.4}$$

The Z' gauge boson is responsible for linking the dark and visible sector, producing the Z' portal [98]. As mentioned, the Z' mediator arises from a U(1) symmetry breaking, and the simulated signal samples are passed through a hidden valley model, where by the one employed for this search is based on Ref [89, 90]. The SM jets then arise from a multi-step process, the dark quarks shower and hadronise in the dark sector and the unstable dark hadrons then decay promptly to SM quarks, and finally the SM quarks shower and hadronize visibly.

Since the SM quarks are much less massive than the dark hadrons, they are produced in the intermediate decay step with a much higher relative momentum because the SM particle showers to spread out. Thus the jets are expected to be wider than typical SM jets. The cross section $\sigma_{Z'}$ is determined by the mediator mass $m_{Z'}$ and the SM coupling g_q, but the branching fraction $\mathcal{B}_{dark} = \mathcal{B}(Z' \to \chi\bar{\chi})$ depends on both couplings g_q and g_{χ} [87], and the production rate is defined as $r_{Z'} = \sigma_{Z'}\mathcal{B}_{dark}$. For $\mathcal{B} \approx 100\%$, we assume $g_{\chi} \gg g_q$, where the dark gluon is the dark QCD force carrier, binding the dark quarks into dark hadrons. These may be vectors (ρ) or pseudoscalars (π). The stable dark hadrons are (π^{DM}_{dark}) and (ρ^{DM}_{dark}) and the unstable dark hardons are (π_{dark}) and (ρ_{dark}), respectively.

The dark hadrons are assumed to be degenerate in mass having a small scale m_{dark}. The dark QCD force coupling strength, α_{dark}, is an undetermined parameter which primarily influences the dark shower dynamics, where it modifies the transverse momentum p_T as well and multiplicity of the dark hadrons, as well as the width of the resulting particle shower. The invisible fraction r_{inv} is an adjustable parameter, where in previous theories the variation of this fraction has not been considered, making this the most novel parameter.

3.3 ATLAS Detector

The ATLAS experiment [99] at the LHC is a multipurpose detector with a forward-backward symmetrical cylindrical geometry and near 4π coverage in solid angle. It consists of electromagnetic and hadronic calorimeters, a muon spectrometer and a inner tracking detector which covers $|\eta| < 2.5$. The inner tracking consists of a silicon pixel detector, a transition radiation tracker (TRT) and a silicon micro-strip detector and is surrounded by a thin superconducting solenoid which provides a 2 T axial magnetic field. An insertable B-layer was installed before Run 2 [100, 101], a lead/liquid-argon (LAr) sampling calorimeter measures the energy and the position of electromagnetic showers in the central ($|\eta| < 1.475$) and end cap ($1.375 < |\eta| < 3.2$) regions with high granularity. LAr sampling calorimeters with copper and tungsten absorbers also measure hadronic showers in the end cap ($1.5 < |\eta| < 3.2$) and forward ($3.1 < |\eta| < 4.9$) regions, while a steel/scintillator-tile hadron calorimeter covers the central pseudorapidity range ($|\eta| < 1.7$). The muon spectrometer surrounds the calorimeters and consists of a system of precision tracking chambers ($|\eta| < 2.7$), fast tracking chambers for triggering ($|\eta| < 2.4$) and three large superconducting air-core toroidal magnets, each with eight coils. The field integral of the toroids ranges between 2.0 and 6.0 Tm across most of the detector. Reconstructed events are then selected by a two-level trigger system, the first is hardware based, using a subset of the detector in formation in order to accept events at a rate up to 100 kHz. The second level is implemented in software, an extensive software suite [102] is used in the reconstruction and analysis of both real and simulated data, in detector operations as well in the trigger and data acquisition systems of the experiment.

3.4 Analysis strategy

3.4.1 Signal characteristics

In this search a benchmark model, the leptophobic Z' boson having a mass of 1500 GeV, is chosen, the jets are reconstructed using the anti-k_t algorithm, with $R_0 = 1.0$. As this was the first analysis, only one benchmark point was used to set up the general search strategy, thus the fraction of stable versus invisible dark hadrons in this case is 0.3. The search used simulated samples incorporating the effect of ATLAS detector. The signal generation is done using MadGraph [103] for the matrix element, and Pythia8 [67] for shower and hadronisation using the hidden valley model, as it uses dark sector showering.

Events in the analysis are selected with an un-prescaled MET trigger, where MET $>$ 200 GeV. For our signal selection, since our final state consists of jets we require a lepton veto of no electrons or muons with transverse momentum $p_T > 7$ GeV, as the detector cannot distinguish at lower p_T values. The leading jet transverse momentum must be greater than 250 GeV, without this selection there are too many initial-state radiation jets polluting the topology. We will have a jet aligned with the MET, we require that the $\Delta\phi$ between the MET and the closest jet must be less than 2. As well, we require that the number of b-jets are less than 2 as this removes most hadronic $t\bar{t}$ background. The signal has two jets produced back to back, both containing invisible particles and the svj is chosen as the jet closest to the MET.

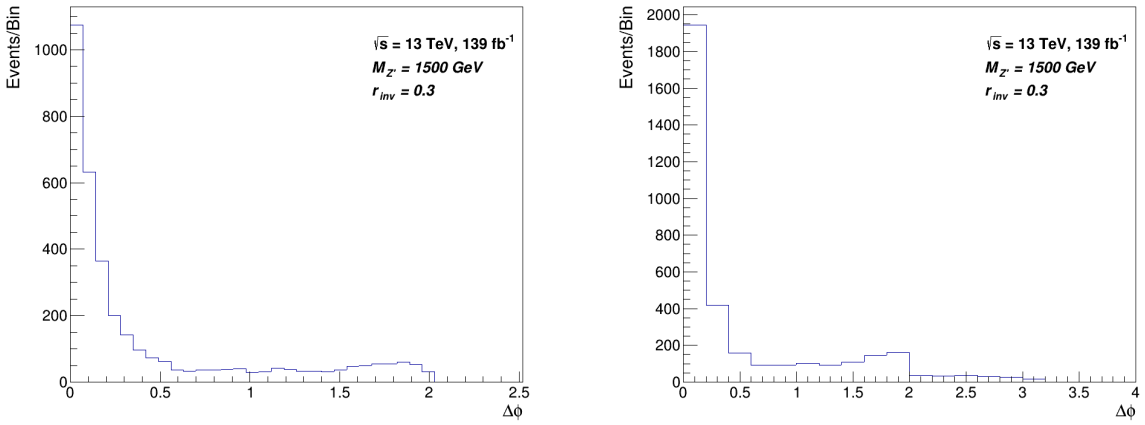


Figure 3.4: The distribution of the $\Delta\phi$ between the closest jet and MET (left) which selects the svj and $\Delta\phi$ between the subleading jet and MET (right).

We see that in most cases the subleading jet is tagged as the svj as expected, as shown in figure 3.4. This is due to the fact that by definition the subleading jet has a higher local MET, so the total MET is balanced with the MET from the leading jet and thus points in the same direction as the subleading jet. There is also an anti-svj (asvj), this is defined to be the jet produced back to the svj in the azimuthal co-ordinate, which is thus the jet farthest from the MET. Plotting the $\Delta\phi$ between the MET and the jet farthest from the MET, now we see that in most cases as well the leading jet is tagged as the asvj as shown in Figure 3.5.

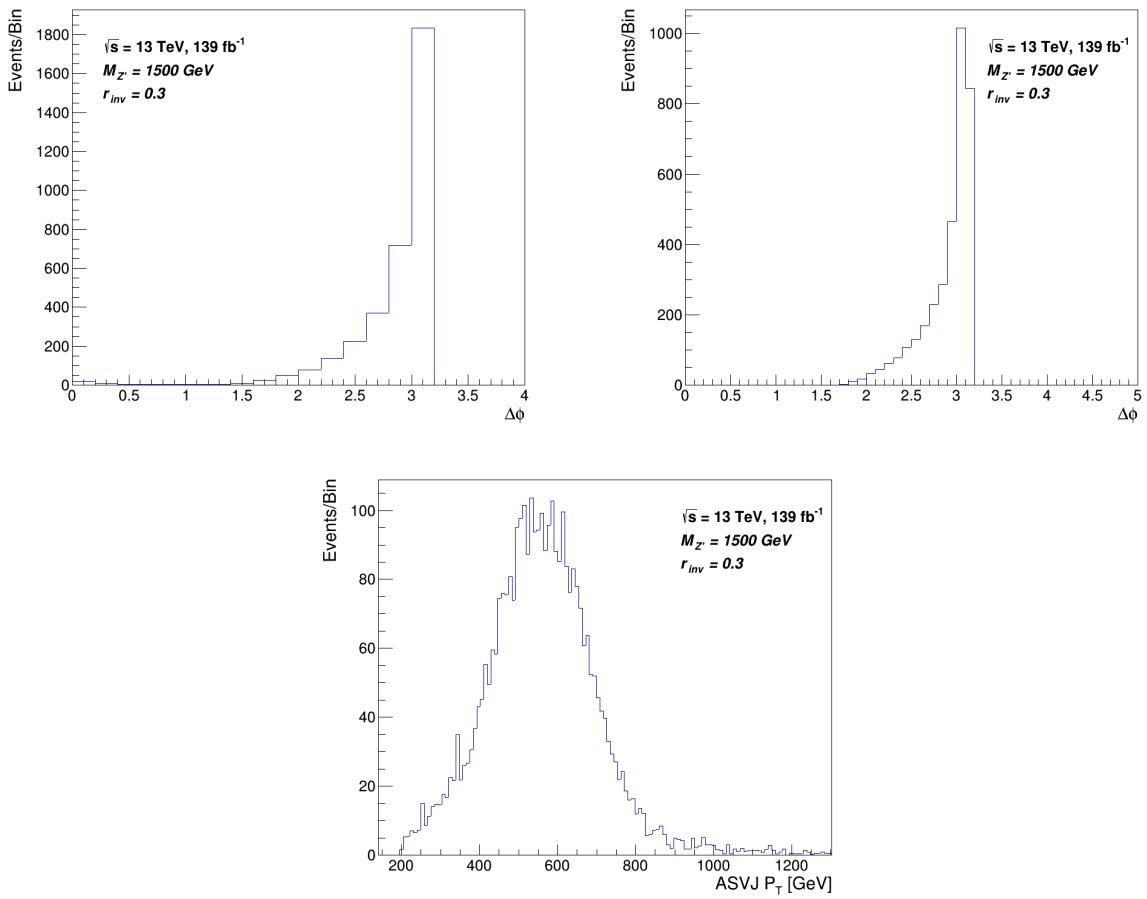


Figure 3.5: The distribution of the $\Delta\phi$ between the farthest jet and MET (left) which selects the asvj, $\Delta\phi$ between leading jet and MET (right) and the p_T of the asvj (bottom).

We want to construct the resonant mass peak accounting for the r_{inv}, Figure 3.6 is the invariant mass distribution of the svj and asvj without accounting for the invisible fraction. Since the invisible fraction is roughly a third of the final state, thus one may expect the invariant mass of the svj and asvj to peak about 1000 GeV.

However, the $r_{inv} = 0.3$ has fluctuations when the jets decay and thus it is not imposed on every jet, so we see that both the invariant mass of the svj and asvj and leading and subleading jets peak around 800 GeV and not 1000 GeV. It is clear that in most cases the svj and asvj are tagged as the subleading and leading jets, but we do not have all decay products enclosed in the $R_0 = 0.1$ jets.

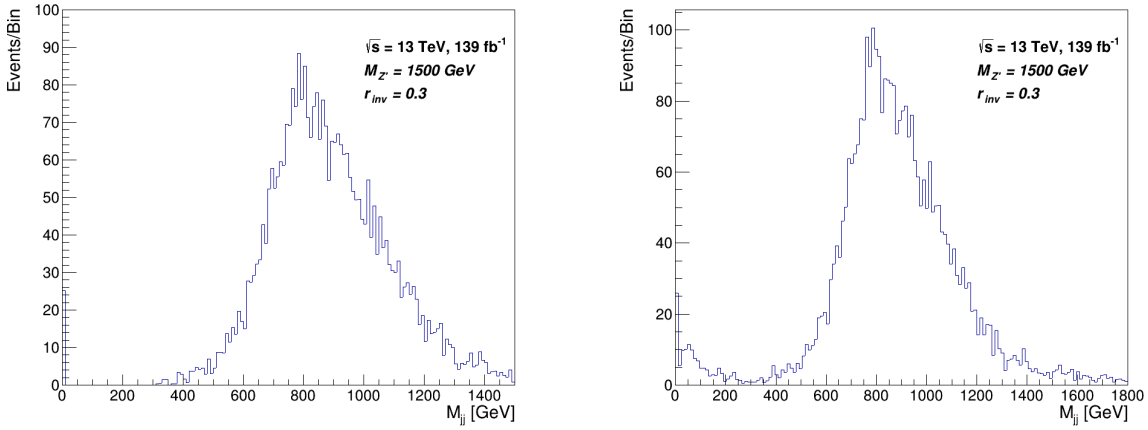


Figure 3.6: Invariant mass of leading and sub-leading jets (left) and svj and anti-svj (right)

3.5 Background

The largest background contribution is from multijet events, however finding discriminating variables to probe is the greatest challenge. The background was generated using a Monte-Carlo generator at Leading-Order (MC@LO) as matrix element, interfaced to Pythia8.

3.5.1 Substructure variables

When working with large radius jets, it is always useful to consider substructure variables as an option to discriminate signal against background. For this case the same variables described in section 2.4.2 are used. Both the svj and anti-svj were considered, however, in most cases the substructure variable distributions were nearly identical. For the cases where the distributions differed both the svj and anti-asvj distributions are given. In some cases the svj signal was much less than that of multijet and unusable, however since the anti-svj has a higher p_T in those distributions the signal visible and hence the asvj distributions were considered. The distributions for the substructure variables are shown in Figures 3.7 to 3.12.

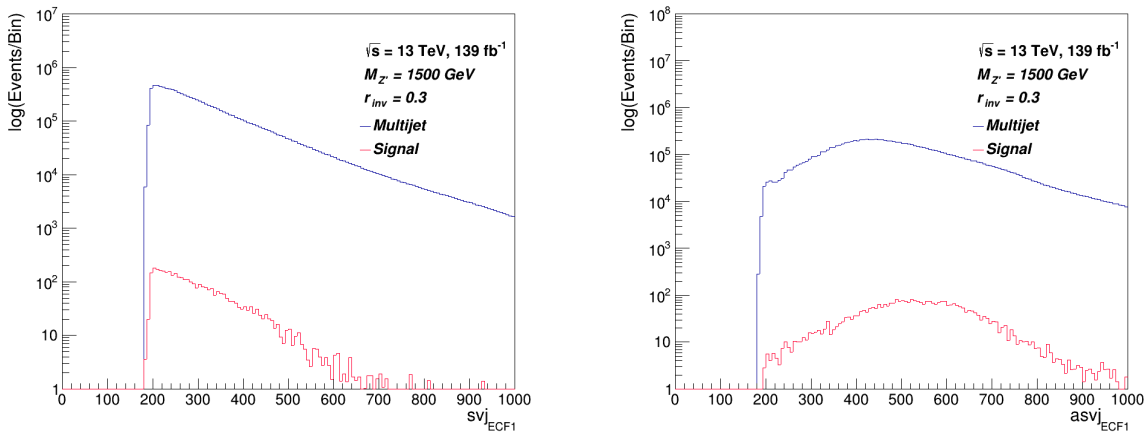


Figure 3.7: ECF1 for svj and anti-svj signal (left and right respectively) against multijet background.

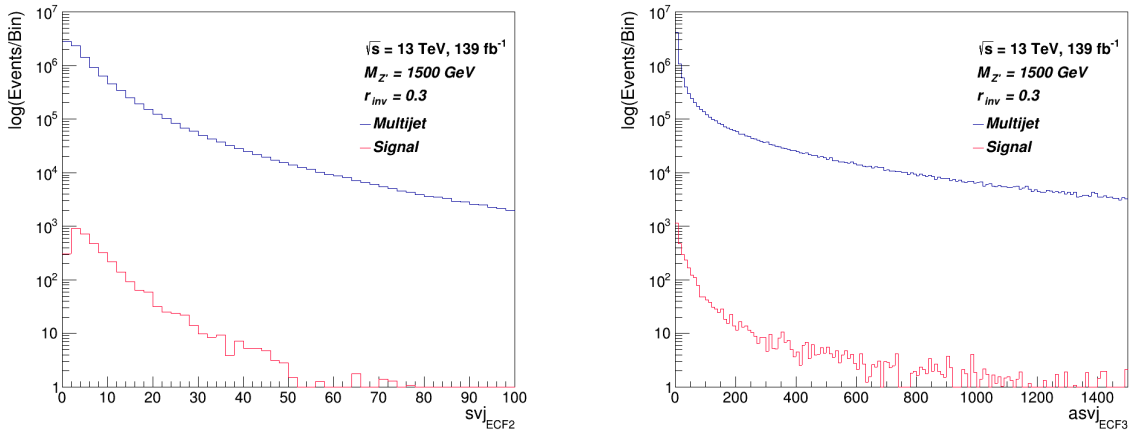


Figure 3.8: ECF2 distribution for svj (left) and ECF3 distribution for anti-svj (right) against multijet background.

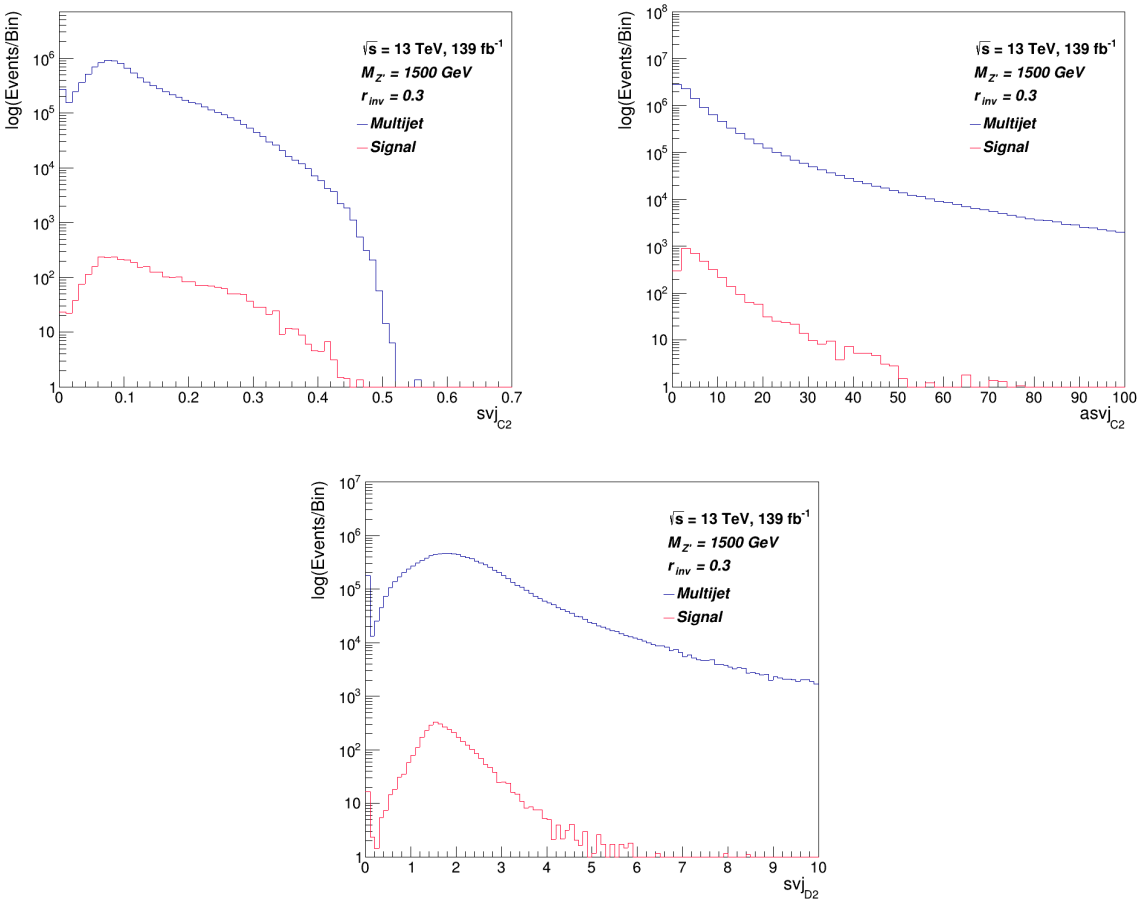


Figure 3.9: C2 distribution for svj and anti-svj (left and right respectively) and D2 distribution for svj against multijet background.

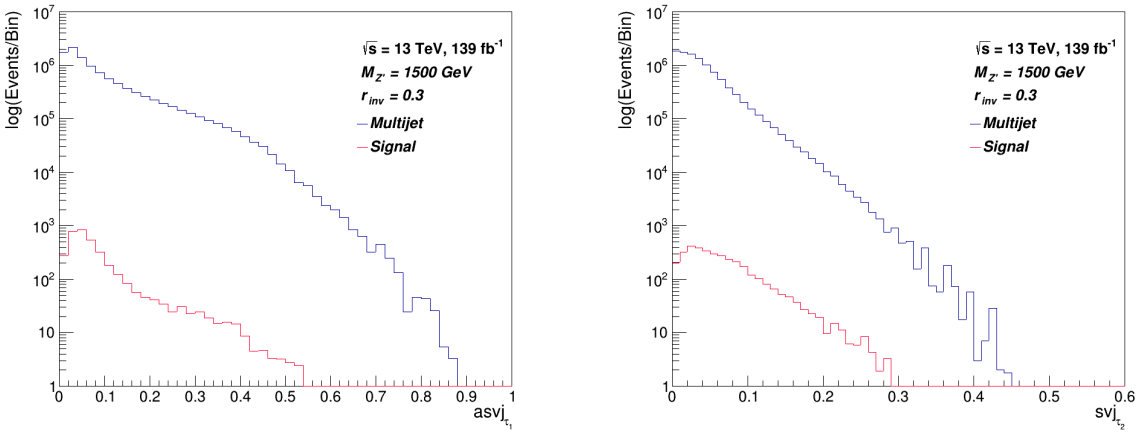


Figure 3.10: τ_1 (left) distribution for anti-svj and, τ_2 (right) distribution for svj against multijet background.

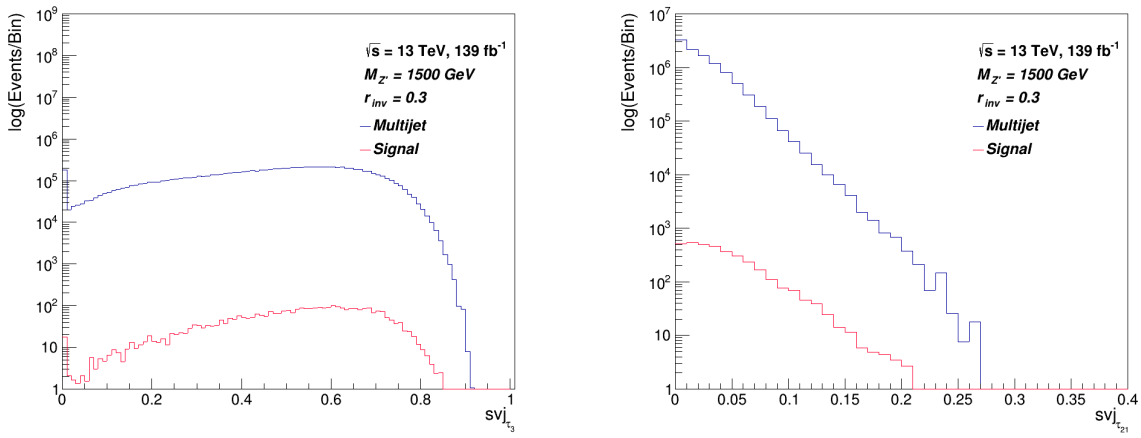


Figure 3.11: τ_3 and τ_{21} (left and right respectively) distribution for svj against multijet background.

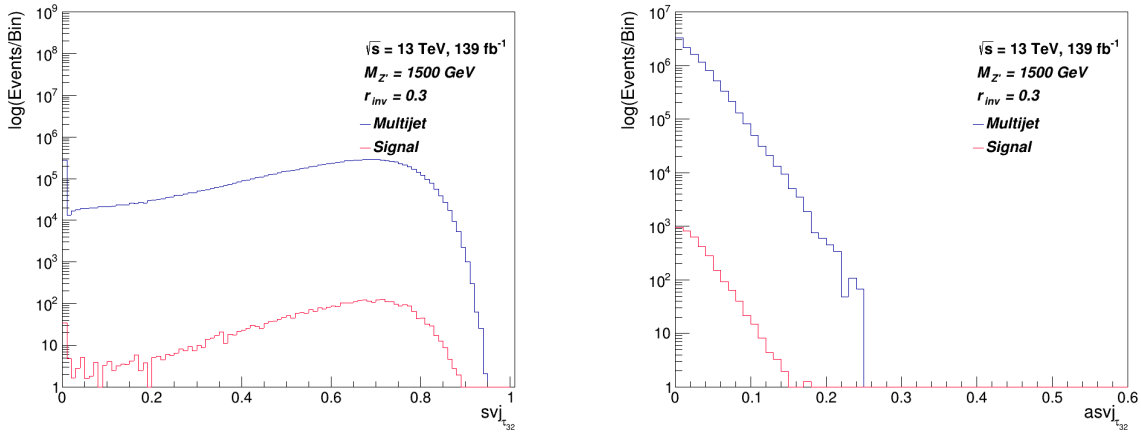


Figure 3.12: τ_{32} distribution for svj and anti-svj (left and right respectively) against multijet background.

The substructure variables considered above show no feasible approach to have a significant effect on reducing the background. Thus additional variables were also considered. The first is the three-point energy correlation ratio [75]. The notation is defined by E_n, differing from that of $ECF(n, \beta)$. Specifically the relationship is given by,

$$E_n^{(\beta)} = \frac{ECF(n, \beta)}{(ECF(1, \beta))^n}. \tag{3.5}$$

Which then gives that E_3 is defined as,

$$E_3^{(\beta)} = \frac{1}{p_{T,J}^3} \sum_{1 \leq i < j < k < \leq n_J} p_{T,i} p_{T,j} p_{T,k} R_{ij}^{\beta} R_{ik}^{\beta} R_{jk}^{\beta}. \tag{3.6}$$

Where, $p_{T,i}$ is the transverse momentum of particle i and $p_{T,J}$ is the transverse momentum of the jet with respect to the beam and n_J is the number of particles in the jet. R_{ij}, the boost invariant angle, given by $R_{ij}^2 = (\phi_i - \phi_j)^2 + (y_i - y_j)^2$, is the Euclidean distance in the azimuthal-rapidity plane, and angular exponent is greater than zero, $\beta > 0$, for infrared and collinear safety. Often the explicit dependence on β is omitted, giving that the n-point energy correlation ratio is simply denoted E_n. The energy correlation ratios are defined, such that in a configuration of n particles, $E_N \to 0$ in any of the soft or collinear limits. The three point energy correlation ratio is shown in Figure 3.13.

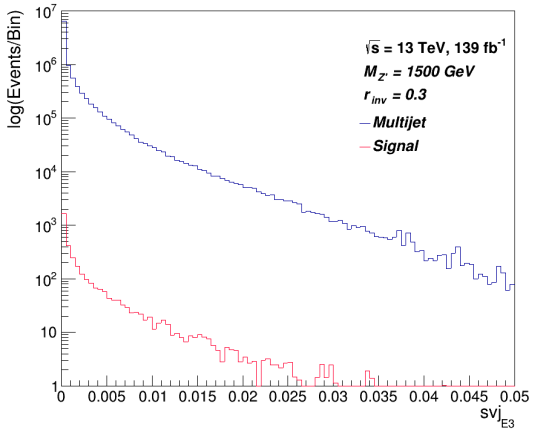


Figure 3.13: E3 substructure distribution for svj against multijet background.

The next substructure variable considered is the splitting scale. The distance measure between two inputs i and j, having energies, E_i and E_j respectively, separated by an angle θ_{ij}, is given by [24],

$$d_{ij} = \frac{2E_i E_j (1 - \cos\theta_{ij})}{Q^2}, \qquad d_{iB} = \frac{1}{p_{T,i}^2}. \tag{3.7}$$

The total energy of the final hadronic state is given by Q^2, this is essentially the invariant mass of the two particle system, scaled by the event energy. d_{ij} vanishes if either i or j are collinear ($\cos\theta_{ij} \to 1$), or soft ($E_i \to 0$ or $E_j \to 0$). However, particles down the beam-pipe are not measured and should not be included in the jets.

Hence, the distance measure must include a beam distance parameter d_{ib}, which is the distance measure between the beam direction (z-axis) and input i. Now, instead of using E and $\cos\theta_{ij}$ we simply use the longitudinally boost-invariant quantities p_T and ΔR, and so the distance measure is given by,

$$d_{ij} = min(p_{T,i}^{2\rho}, p_{T,j}^{2\rho})\frac{\Delta R_{ij}^2}{R_0^2}, \qquad d_{iB} = p_{T,i}^{2\rho} \tag{3.8}$$

The exponent ρ controls the merging or ordering depending on its chosen value and in the case of the anti-k_T algorithm is -1. Since the anti-k_T algorithm "abandons" the notion of imitating the parton shower, the distance measure between two penultimate ingredients is given by [104],

$$d_{ij} = min\left(\frac{1}{p^2T,i}, \frac{1}{p_{T,j}^2}\right)\frac{\Delta R_{ij}^2}{R^2}, \qquad d_{iB} = \frac{1}{p_{T,i}^2}. \tag{3.9}$$

This variable is generally referred to as the splitting scale sd_{ij}, where the subscripts denote the stage of clustering the distance measure corresponds to. The splitting scales sd_{12} and sd_{23} are shown in Figure 3.14

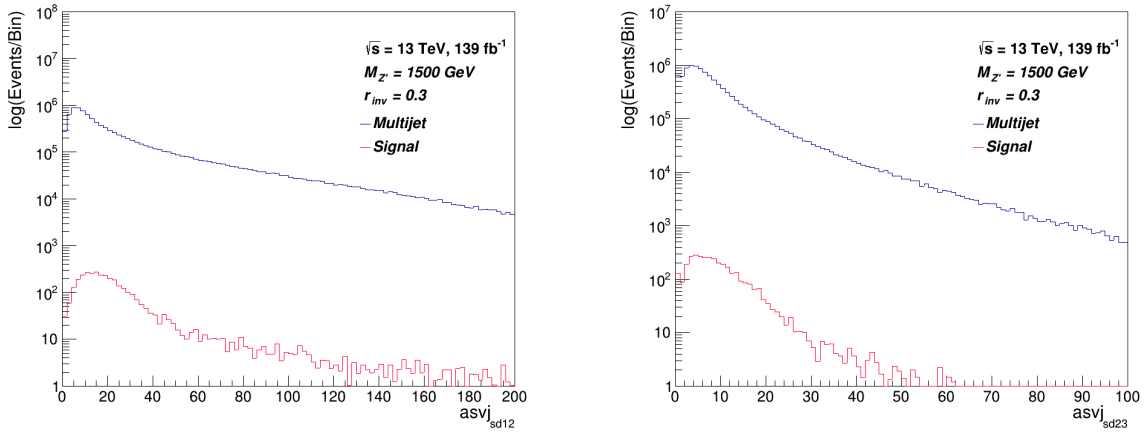


Figure 3.14: sd_{12} and sd_{23} distributions for anti-svj (left and right respectively) against multijet background.

The final additional substructure variable considered is the variable Q_W. It is the minimum pair invariant mass [104] of the three subjets identified at the splitting scale sd_{23}, given in Figure 3.15

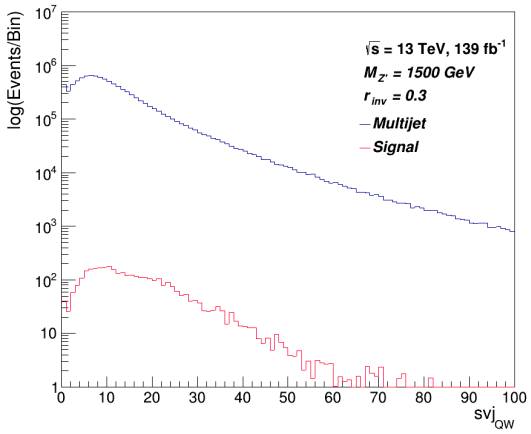


Figure 3.15: Q_W distribution for svj against multijet background.

As in the case of the initial substructure variables considered, the background and signal are far to similar and thus they are not useful variables in the sense of background optimisation. Thus some other variables must be considered and explored.

3.5.2 Kinematic variable distributions for signal against background

An initial look at background contributions investigates the largest background, which is multijet. We see that the background has an almost identical distribution for all variables currently considered, an example of some of these variables can be seen in Figures 3.16 and 3.17.

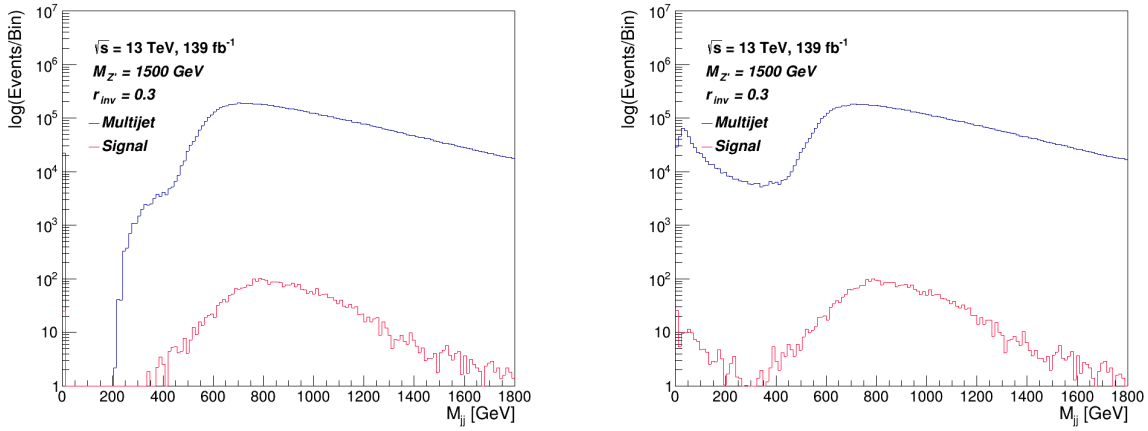


Figure 3.16: Invariant mass for signal against multijet for leading and sub-leading jet (left) and the svj and anti-svj (right).

The invariant mass background for the svj and asvj is interesting, it presents a sculpting shape, whereby the shape of the invariant mass distribution of the background follows that of the signal. However, it would be expected that the background shape would differ from the signal. One possibility for this may be due to the high p_T cut implemented on the leading jet of $p_T > 250$ GeV. Looking at the background against the signal it is clear that there were no discriminant variables found in this analysis which may reduce the background feasibly in order to conduct a realistic search for semi-visible jets.

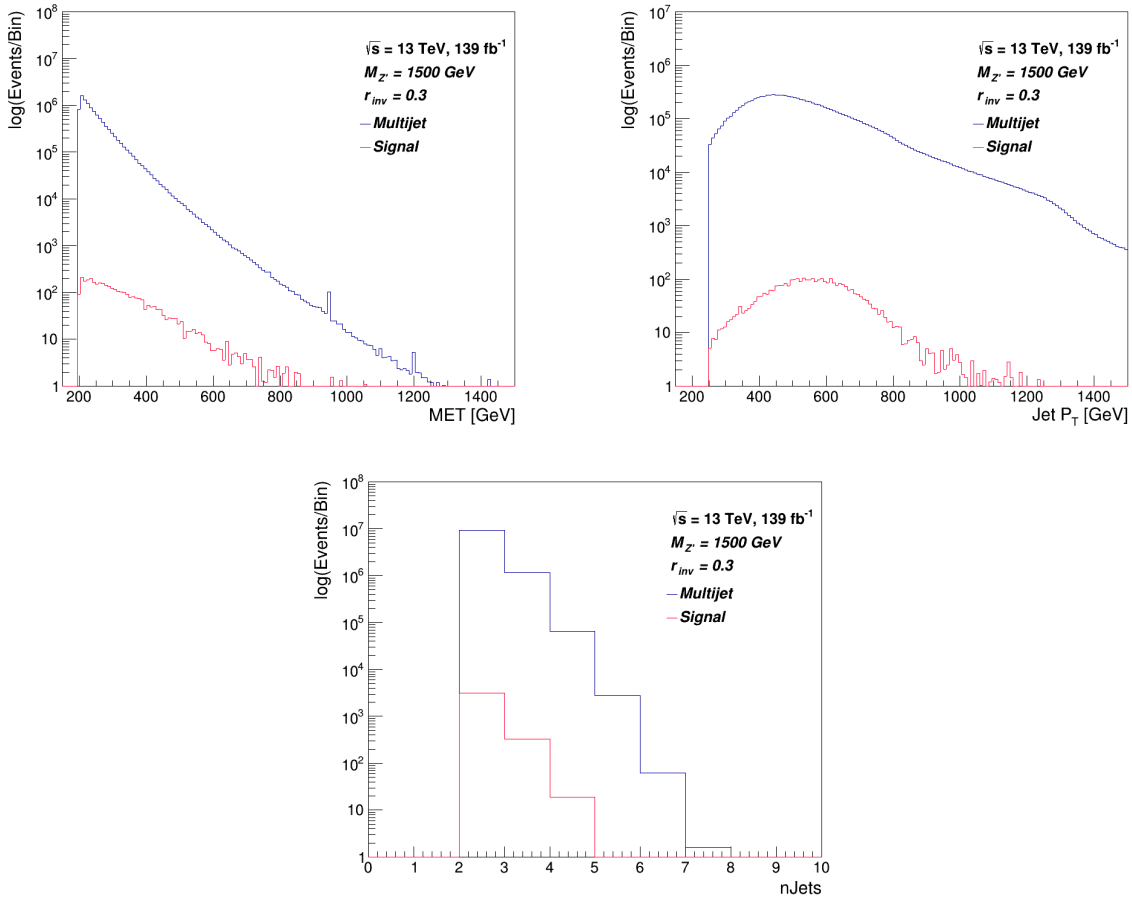


Figure 3.17: MET for signal against multijet (right), leading jet p_T for signal against multijet (left) and number of jets for signal against multijet (bottom).

From the above figures it is clear that the multijet is a substantial background which seems to in general have similar features to our signal. However, it also effective to compare the signal and background with a normalized area to consider the shapes of them both. The variables in which the shapes of the signal and background showed a more significant difference than compared to others are given in Figures 3.18 and 3.19.

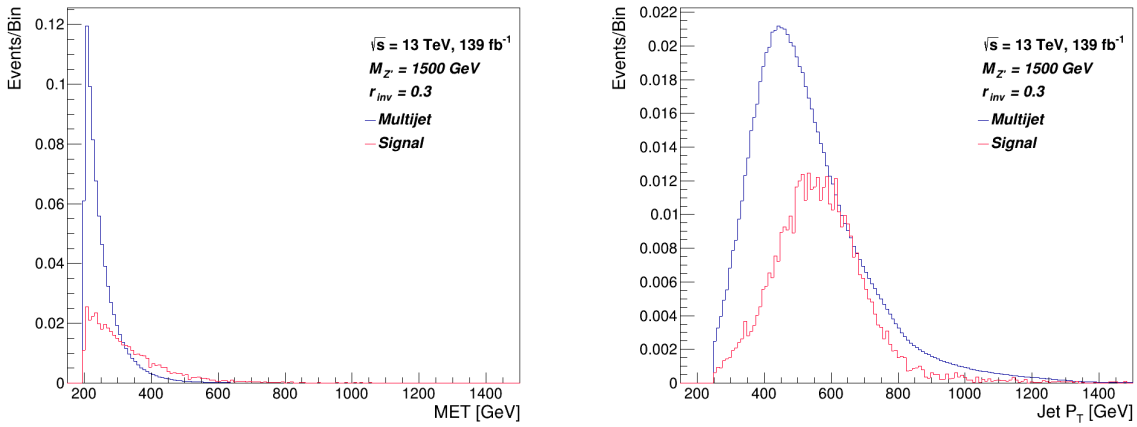


Figure 3.18: MET for signal against multijet (right), leading jet p_T for signal against multijet (left) area normalised.

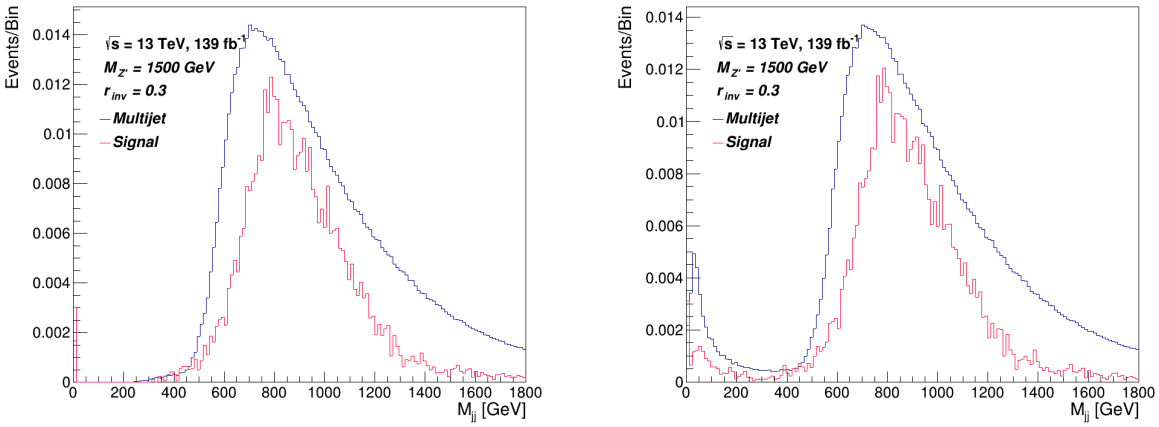


Figure 3.19: Invariant mass for signal against multijet for leading and sub-leading jet (left) and the svj and anti-svj (right) area normalised.

3.6 Conclusion

A study of semi-visible jet searches in a resonant production mode was presented. As a first look, it is clear that the physics is sensible. We see that we do have a dijet system and are able to select a svj and anti-svj, where it is clear that they are tagged as the sub-leading and leading jets respectively. As well we are able to reconstruct the svj and anti-asvj invariant mass, where the mass peak is close to what is expected with an r_{inv} of 0.3, with some discrepancy. An initial look at the largest background (multijet) is considered, and none of the variables considered give a viable scheme to reduce the background. This is an ongoing search in ATLAS and some new ideas are needed in terms of reducing and estimating the background. It is known that LO QCD multijet MC does not describe the data well. Thus the use of data driven background estimation methods will have to be accounted for as well. However, it can be seen that we are able to produce the signal model as we can reconstruct the svj and anti-svj.

4 Track Reconstruction using Quantum computing for LUXE

4.1 Introduction

The theory of Quantum electrodynamics (QED), describes the interactions of both light and matter with a structure encompassing quantum mechanics and special relativity. QED predictions are in line with precision measurements of the electrons magnetic moment as well as the fine structure constant with immense accuracy. This has been performed by testing the perturbative regime of QED, due to the small value of the fine structure constant these phenomena can be accurately described with perturbative methods. The Laser Und XFEL Experiment (LUXE) [105] will combine the high-quality and high-energy electron beam of the European XFEL (X-ray Free Electron Laser) with a powerful laser to explore the uncharted terrain of quantum electrodynamics, characterised by both high energy and high intensity in the non-perturbative regime.

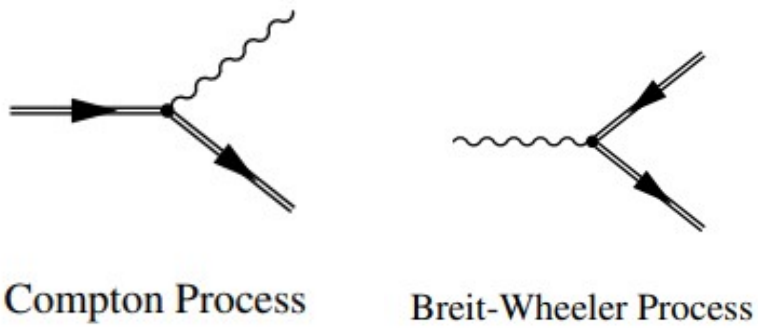


Figure 4.1: Feynman diagrams showing processes for the non-linear Compton scattering and Breit-Wheeler pair production in the non-perturbative regime from Ref [105].

The two processes of interest shown in Figure 4.1 [105] are nonlinear Compton scattering, where the photon is radiated from the electron in the laser field,

$$e^- + n\gamma_L \rightarrow e^- + \gamma \tag{4.1}$$

and the non-linear Breit-Wheeler pair creation, from the interaction of a photon (which may be from the Compton process) in the laser field.

$$\gamma + n\gamma_L \rightarrow e^+ + e^-. \tag{4.2}$$

Where n is the number of laser photons γ_L in the process. In the non-perturbative regime the Compton edge in the energy spectrum is shifted to higher energies, and it is predicted that the Breit-Wheeler pair production rate has a slower increase with increase in laser intensity than that of the perturbative regime. The laser field intensity ξ characterises these interactions and is defined as,

$$\xi = \sqrt{4\pi\alpha}\frac{\epsilon_L}{\omega_L m_e} = \frac{m_e \epsilon_L}{\omega_L \epsilon_{cr}} \tag{4.3}$$

where α is the fine structure constant, ϵ_L is the laser field strength, ω_L is the laser frequency, m_e is electron mass and ϵ_{cr} is the critical field strength also referred to as the Schwinger limit, a scale in QED where above this limit the electromagnetic field is expected to become non-linear. The experimental setup is shown in Figure 4.2 below, the electron beam is guided to the interaction point (IP), where it collides with the laser. The electrons and positrons produced in these interactions are then deflected and separated by a magnet and detected, the electron beam forward direction is in the z-plane.

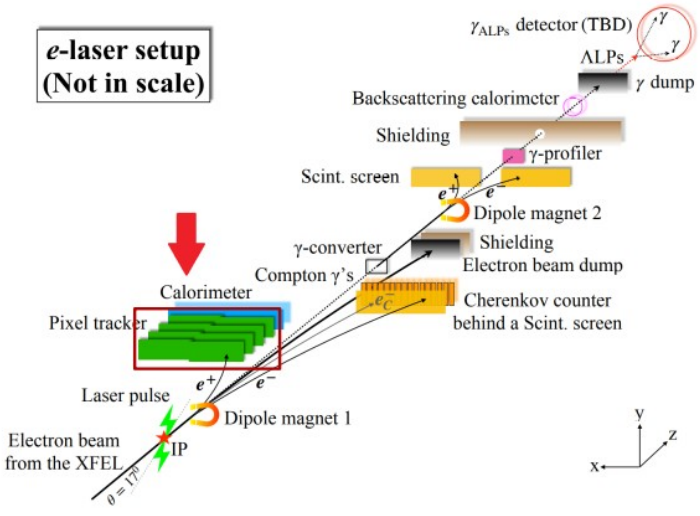


Figure 4.2: Schematic layout of LUXE for e-laser setup [105]

One of the main planned measurements at LUXE is the positron flux as a function of the laser field intensity ξ over a large range of ξ values. The positron flux is important for the Breit-Wheeler pair creation for the e-laser case to measure the rate of pair creation without a large electron beam background. The tracking study presented concerns only positrons which are detected using the four layer silicon pixel tracking detector. Two main tracking challenges are to maintain good linearity as well as keep a low background rate per bunch. As well, there can be up to one million positrons per bunch crossing which can be quite a demanding challenge for classical computers. To try and cope with this, the potential use of quantum computing is investigated.

4.2 Quantum Computing

Quantum computing is an exciting combination of quantum physics, computer science and information technology. Like a classical computer, quantum computers, in brief, can be described as a series of bits and gates. In classical computing bits are either 1's or 0's, however in quantum computing there are qubit states, with basis states,

$$|0\rangle = \begin{pmatrix} 1 \\ 0 \end{pmatrix} \qquad |1\rangle = \begin{pmatrix} 0 \\ 1 \end{pmatrix}$$

where qubit states may be the basis states or a linear combination $|\Phi\rangle = \alpha\,|0\rangle + \beta\,|1\rangle$, but classical bits are finite states of either 1 or 0. Qubits are a two-level quantum mechanical system which can be represented geometrically using a Bloch sphere [106] shown below in Figure 4.3.

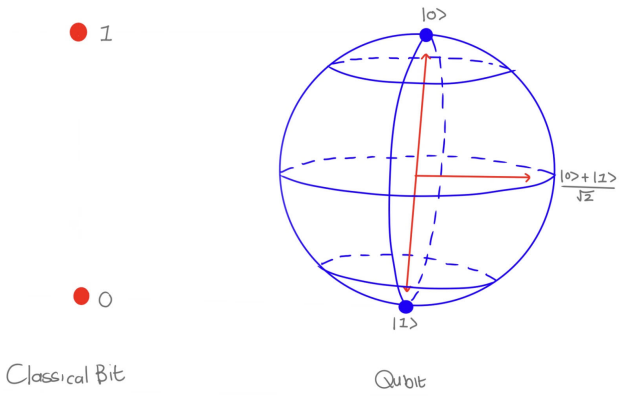


Figure 4.3: Classical bit representation (left) and Bloch sphere representation of the qubit (right).

In classical computing logic gates perform operations on a single bit or multiple bits to give a binary output. In quantum computing these are now quantum gates, however their operation and output can differ greatly from its classical counterpart. One way this difference can be shown is by considering a classical AND gate and the quantum CNOT gate (mathematically represented as CX), both are "multi-bit" operators however their operations and output differ.

Input		Output
A	B	A and B
0	0	0
0	1	0
1	0	0
1	1	1

Figure 4.4: Visual representation of the classical AND gate.

For the operation of a classical AND gate, for this gate we begin with two initial bits where both affect the output and the output is only a single bit. For this gate both initial bits must be one for the output to be one otherwise the output is zero as shown in Figure 4.4.

Input		Output	
X	Y	X	Y+X
|0>	|0>	|0>	|0>
|0>	|1>	|0>	|1>
|1>	|0>	|1>	|1>
|1>	|1>	|1>	|0>

Figure 4.5: visual representation of the quantum CNOT gate.

Unlike the classical AND gate the quantum CNOT gate takes in two inputs (X,Y) and gives two outputs (X,Y+X), the requirements also differ from that of the AND gate.

Now we have a control and target qubit and unlike before there is a requirement on only one of the qubits. If we consider Figure 4.5 our control qubit (X) affects the target qubit (Y). If (X) is in the basis state $|1\rangle$ the target qubit (Y) "flips" to the opposite state, so in this case if it is in state $|1\rangle$ it would flip to state $|0\rangle$ and vice versa as shown. Thus the control qubit (X) remains unchanged and the target qubit (Y) transforms to (Y+X).

It is important to note that only the target qubit is operated on and the control qubit remains unchanged. There are many useful quantum gates, some worth noting are the X, Y and Z gates also referred to as the Pauli gates, these are the three Pauli matrices which act on a single qubit. They can be represented as rotations in the x, y and z-plane of the Bloch sphere by π radians.

$$X = \begin{bmatrix} 0 & 1 \\ 1 & 0 \end{bmatrix} \qquad Y = \begin{bmatrix} 0 & -i \\ i & 0 \end{bmatrix} \qquad Z = \begin{bmatrix} 1 & 0 \\ 0 & -1 \end{bmatrix} \tag{4.4}$$

Another useful gate to mention is the Hadamard gate, this gate acts on a single qubit and maps the basis states $|0\rangle \mapsto \frac{|0\rangle+|1\rangle}{\sqrt{2}}$ and $|1\rangle \mapsto \frac{|0\rangle-|1\rangle}{\sqrt{2}}$, creating an equal superposition state if given a computational basis state. On the Bloch sphere the Hadamard gate performs a rotation of π about the $\frac{\hat{x}+\hat{z}}{\sqrt{2}}$ plane. The Hadamard matrix is more tricky, it is a $2^m \times 2^m$ matrix defined by,

$$H_m = \frac{1}{\sqrt{2}} \begin{bmatrix} H_{m-1} & H_{m-1} \\ H_{m-1} & -H_{m-1} \end{bmatrix}, \tag{4.5}$$

where $(H_m)_{i,j} = \frac{1}{2^{m/2}}(-1)^{i \cdot j}$, $i,\ j$ are the matrix indices and $(i \cdot j)$ is the bitwise dot product. This equation determines the Hadamard matrix for $m > 1$, for $m < 1$ the Hadamard matrix is simply $H_1 = [1]$.

One of the most important aspects of quantum computing is quantum entanglement. Quantum entanglement is the physical phenomenon that occurs when a group of particles are generated in a way such that the quantum state of each particle of the group cannot be described independently of the state of the others. The state of each particle cannot be described independently, however as a whole it is in a definite state, although parts of the system are not.

Without entanglement we are merely doing optimisation instead of utilising quantum mechanics to improve our processes and systems. We also want quantum entanglement as it may improve the processing speed of the quantum computation, if two qubits are entangled, when we operate on one qubit it will of course affect its entangled partner. It is important to note that although entanglement is useful and important in doing quantum computations, it also increases the noise which affects the final measurements of our system.

Quantum gates can be used to create quantum entangled states, the most optimal and maximally entangled states are Bell states. The Hadamard gate paired with a CNOT gate can create an entangled Bell state. For example, if we began with two qubits q_0 and q_1 both in the $|0\rangle$ basis state, if we were to apply a Hadamard gate to q_0 you would get the superposition state $\frac{|0\rangle+|1\rangle}{\sqrt{2}}$ so applying the CNOT gate this gives,

$$CX\,|q_0q_1\rangle = CX|\frac{|0\rangle+|1\rangle}{\sqrt{2}}(|0\rangle) = CX|\frac{1}{\sqrt{2}}(|00\rangle+|10\rangle) = \frac{1}{\sqrt{2}}(|00\rangle+|11\rangle) \tag{4.6}$$

This gives us the Bell state $|\Phi^+\rangle$ where the probability of the system being in state $|00\rangle$ and $|11\rangle$ are equal and all other states are zero. This calculation and operation can be tedious to show and so to represent the gates and operations acting on different qubits and qubit systems what is referred to as a quantum circuit is used.

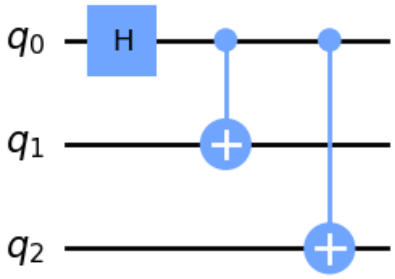


Figure 4.6: Quantum circuit for three qubits under Hadamard and CNOT gate operations

Figure 4.6 shows a quantum circuit, quantum circuits are simplified ways of representing all the operations in a quantum system. This quantum circuit shows three qubits q_0, q_1 and q_2. The blue square with the capital H represents a Hadamard gate and in this circuit the Hadamard gate is being applied to q_0. The blue dots connected to the blue circles with a plus inside represent CNOT gates where the blue dot is the control qubit and the blue circle with the plus is the target qubit.

4.3 The building blocks of track candidates

The building blocks of track candidates are doublets and triplets, defined as a set of two or three hits on consecutive layers respectively. Doublets are formed first, in the detector area there is no magnetic field, but the tracks are bent initially by a dipole magnet.

The bending radius of particle with charge e, energy E, and momentum p in a uniform magnetic field B is given by

$$\frac{1}{\rho} = \frac{eB}{pc} = \frac{eB}{\beta E}. \tag{4.7}$$

Where β is the relative velocity $\frac{v}{c}$ and c is the speed of light. Thus, tracks from positrons will form an angle with the beam-axis z dependent on their initial energy, so particles with higher energies will have a smaller bending radius than those of lower energies. Doublets are formed considering all hits on consecutive layers that pass a pre-selection, since there is no magnetic field in the detector area the positrons will have linear trajectories and so every doublet needs to fulfill the following requirement shown in Equation 4.8 and Figure 4.7, where c is constant.

$$\frac{dx}{x_0} \approx c \qquad \text{where,} \quad dx = x_2 - x_1. \tag{4.8}$$

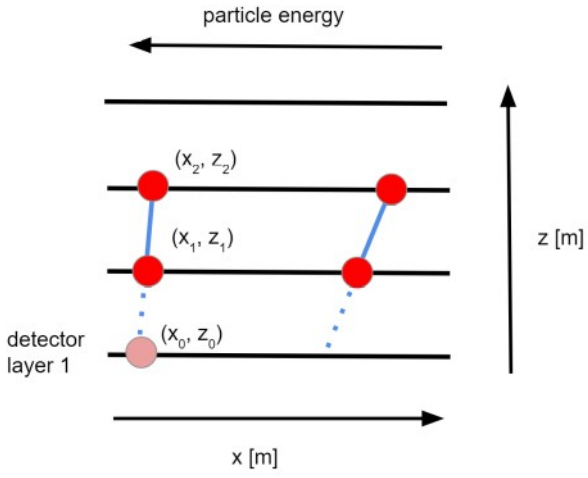


Figure 4.7: Formation of doublets and selection requirements.

However the positrons may interact with the detector material and the detector itself is not perfect and may not always make precise position measurements. Thus, we choose an interval $\frac{dx}{x_0} \in [c-\epsilon, c+\epsilon]$. The distribution of the number of correct doublets to fake doublets is given by a Gaussian distribution and the value of ϵ is chosen by taking five standard deviations of the distribution to remove majority of fake doublets without losing too many correct doublets.

Triplets are then formed from two corresponding doublets, again since tracks should be straight, we require that corresponding doublets have an angle between them close to π. Thus, we implement an interval for chosen triplets for the angle requirement $[\pi-\epsilon_t, \pi+\epsilon_t]$. The distribution for correct triplets to fake is also a Gaussian distribution and so ϵ_t is taken as five standard deviations as well. Once the triplets and doublets are selected, the optimal triplet pair candidates which can be combined to form track candidates are then found, this selection process is done using quantum computing.

4.4 Quantum Computing for track selection

The optimal pairs of triplets which can be combined to form tracks, are identified using a quadratic unconstrained binary optimisation (QUBO) [107], given by

$$O = \sum_{i}^{N} \sum_{j<i} b_{ij} T_i T_j + \sum_{i=1}^{N} a_i T_i \qquad T_i, T_j \in \{0, 1\} \tag{4.9}$$

The QUBO is a cost function mapping to a Hamiltonian with the objective of finding the ground state, as the minimum of the function corresponds to the optimal solution which is the ground state for the Hamiltonian. The linear term of the QUBO is a characteristic term and weighs the individual triplets by their quality which is quantified by the coefficient a_i. The quadratic term is a connectivity term expressing interactions between triplet pairs, where the compatibility is characterised by the coefficient b_{ij}.

$$b_{ij} = \begin{cases} 0, & \text{If no shared hit (triplets do not overlap)} \\ +1, & \text{If in conflict (triplets overlap but cannot form a track candidate)} \\ -S(T_i, T_j), & \text{If forming a track candidate (triplets fully overlap)} \end{cases}$$

The QUBO is then mapped to an Ising Hamiltonian and solved using the Variational Quantum Eigensolver (VQE). We use VQE as it is a quantum algorithm which is resistant to noise. VQE is a hybrid algorithm which uses classical optimization while finding the ground state using quantum computing.

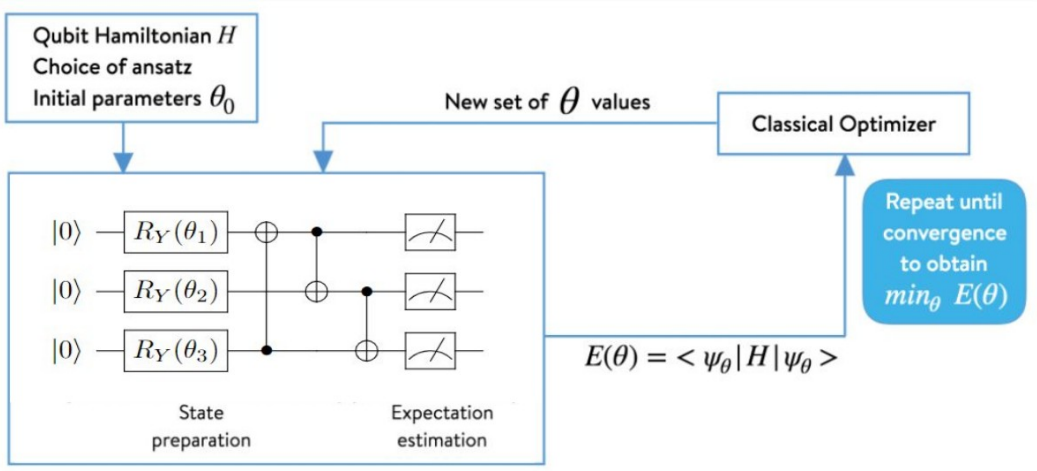


Figure 4.8: Diagram of VQE algorithm recreated from ref-[108]

Initial parameters are chosen classically and then put through the quantum algorithm where it performs an energy evaluation, the VQE then optimizes classically feeding in new parameters until it converges to obtain the minimum energy. The VQE is useful as it can find the ground state or at least get close to it, a task challenging for a classical computer to achieve [109]. However, since each triplet is mapped to a single qubit, we are limited on the number of qubits we have, as well we are limited on how many qubits IBM has available.

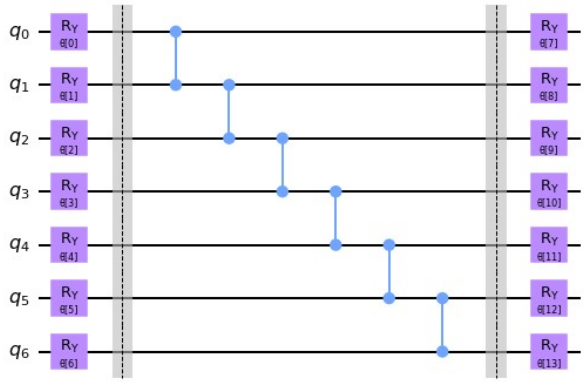


Figure 4.9: Circuit representation of RY and CZ gate for 7 qubit TwoLocal ansatz.

This study considered a simple tracking example to compare the pattern finding performance using Numpy Eigensolver (analytical solver), two quantum device simulators, where one is noise free and the another accounts for noise, and then a real quantum device provided by IBM, with the quantum devices using 7 qubits as the simple tracking example has 7 triplets.

The circuit is a TwoLocal ansatz [110], a parameterized circuit which consists of entanglement layers and alternating rotation layers. The rotation layers are simply single qubit gates which are applied to all qubits in the circuit. The entanglement layers use two-qubit gates to entangle qubits according to a user chosen strategy. The chosen strategy for the circuit is linear, where qubit i is entangled with qubit $i+1$, for all $i \in 0, 1, ..., n$, where n is the total number of qubits. The circuit consists of a RY rotation gate [111] (single-qubit rotation about the Y-axis) and a Controlled Z gate (CZ), with 512 shots which is the number of evaluations with a fixed set of parameters.

4.5 Results

The NumPyEigensolver (analytical solver) gives an exact solution used as a benchmark, which for our simple example is [0,0,0,1,1,1,1]. The ideal simulation, simulates a quantum device without noise whereas the fake device is modelled after a real quantum device accounting noise.

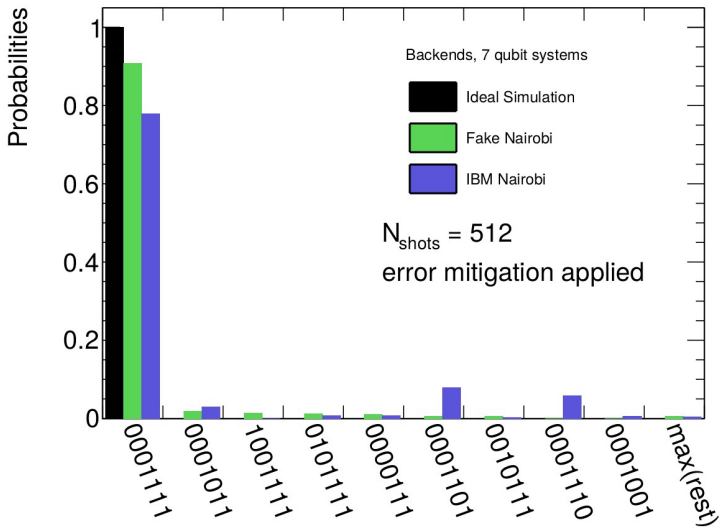


Figure 4.10: Comparison between ideal simulation, fake quantum device accounting for noise and the real quantum device.

The results for the chosen parameters are shown in Figure 4.10. We see that unlike the ideal simulation we do not get 100% accuracy for the state but a probability distribution due to noise. The fake device performs better than the real device, this indicates that it may be underestimating the amount of noise of the real device.

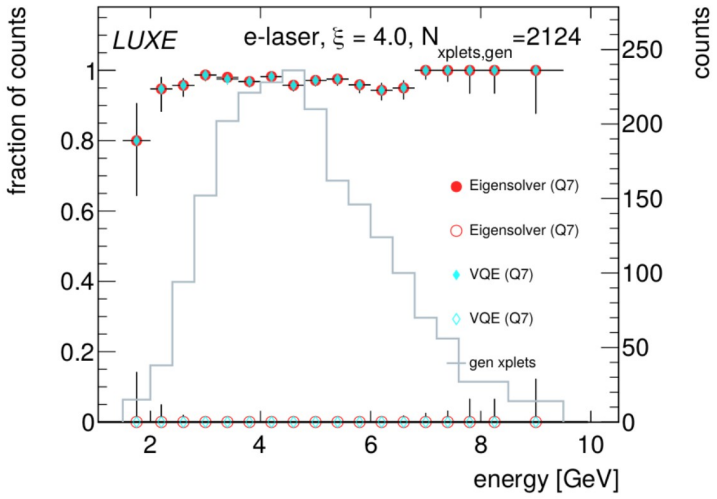


Figure 4.11: Efficiency rate of a track selected being a real track to a fake track against the particles true energy.

For a single bunch crossing consisting of about ∼2100 particles there are more than 5000 triplets, but since we have only 7 qubits, we partition these into parts of 7 and then solve them successively. Figure 4.11 shows the efficiency of the track chosen being the correct track compared to a fake track against the particles true energy. So we still get a very high number of correctly matched triplets (shaded in pointers) and a very low rate of fake triplets being matched (hollow pointers).

4.6 Conclusion

The results show that even for a simple example we don't get 100% accuracy when noise is accounted for. The fake device performed better than the real device and so the fake device underestimates the amount of noise of the real device. However, using a fake device is still sufficient as it gives a useful starting point to study quantum computing. It is also useful to start with the fake device as computations are much less time intensive. The IBM real device is open source and computations can sometimes take days to complete for even the most simple examples.

References

[1] J. H. Kim, S. D. Lane, H.-S. Lee, I. M. Lewis, and M. Sullivan, "Searching for dark photons with maverick top partners," *Physical Review D*, vol. 101, no. 3, p. 035041, 2020.

[2] S. Weinberg, "The making of the standard model," *The European Physical Journal C-Particles and Fields*, vol. 34, no. 1, pp. 5–13, 2004.

[3] C.-N. Yang and R. L. Mills, "Conservation of isotopic spin and isotopic gauge invariance," *Physical review*, vol. 96, no. 1, p. 191, 1954.

[4] S. Glashow, "Partial-symmetries of weak interactions, in nuclear physics," 1961.

[5] P. W. Higgs, "Broken symmetries and the masses of gauge bosons," *Physical Review Letters*, vol. 13, no. 16, p. 508, 1964.

[6] F. Englert and R. Brout, "Broken symmetry and the mass of gauge vector mesons," *Physical review letters*, vol. 13, no. 9, p. 321, 1964.

[7] G. S. Guralnik, C. R. Hagen, and T. W. Kibble, "Global conservation laws and massless particles," *Physical Review Letters*, vol. 13, no. 20, p. 585, 1964.

[8] K. G. Wilson, "Confinement of quarks," *Physical review D*, vol. 10, no. 8, p. 2445, 1974.

[9] P. D. Group, P. Zyla, R. Barnett, J. Beringer, O. Dahl, D. Dwyer, D. Groom, C.-J. Lin, K. Lugovsky, E. Pianori, *et al.*, "Review of particle physics," *Progress of Theoretical and Experimental Physics*, vol. 2020, no. 8, p. 083C01, 2020.

[10] Y. S. Kim and M. Noz, *Theory and applications of the Poincaré group*, vol. 17. Springer Science & Business Media, 1986.

[11] S. F. Novaes, "Standard model: An introduction," 2000.

[12] M. Drewes, "The phenomenology of right handed neutrinos," *International Journal of Modern Physics E*, vol. 22, no. 08, p. 1330019, 2013.

[13] S. Weinberg, "New approach to the renormalization group," *Physical Review D*, vol. 8, no. 10.

[14] M. Veltman *et al.*, "Regularization and renormalization of gauge fields," *Nuclear Physics B*, vol. 44, no. 1, pp. 189–213, 1972.

[15] S. Weinberg, "A model of leptons," *Physical review letters*, vol. 19, no. 21, p. 1264, 1967.

[16] J. Ellis, "Higgs Physics," pp. 117–168, 2015. 52 pages, 45 figures, Lectures presented at the ESHEP 2013 School of High-Energy Physics, to appear as part of the proceedings in a CERN Yellow Report.

[17] ATLAS Collaboration, "Observation of a new particle in the search for the standard model higgs boson with the atlas detector at the lhc," *Physics Letters B*, vol. 716, no. 1, pp. 1–29, 2012.

[18] CMS Collaboration, "Observation of a new boson at a mass of 125 gev with the cms experiment at the lhc," *Physics Letters B*, vol. 716, no. 1, pp. 30–61, 2012.

[19] A. D. Sakharov, "Violation of cp-invariance, c-asymmetry, and baryon asymmetry of the universe," in *In The Intermissions... Collected Works on Research into the Essentials of Theoretical Physics in Russian Federal Nuclear Center, Arzamas-16*, pp. 84–87, World Scientific, 1998.

[20] R. D. Peccei, "The strong cp problem and axions," in *Axions*, pp. 3–17, Springer, 2008.

[21] F. L. Manghi, "Lucid: The atlas luminosity detector," *PoS Proc. Sci*, p. 280, 2018.

[22] V. Cindro, D. Dobos, I. Dolenc, H. Frais-Kölbl, A. Gorišek, E. Griesmayer, H. Kagan, G. Kramberger, B. Macek, I. Mandić, *et al.*, "The atlas beam conditions monitor," *Journal of Instrumentation*, vol. 3, no. 02, p. P02004, 2008.

[23] M. Schott and M. Dunford, "Review of single vector boson production in pp collisions at $\sqrt{s} = 7$ TeV. Review of single vector boson production in pp collisions at $\sqrt{s} = 7$ TeV," *Eur. Phys. J. C*, vol. 74, 2014. Comments: 60 pages, 64 figures.

[24] D. Kar, *Experimental Particle Physics*. IOP Publishing Limited, 2019.

[25] C. Matteo, P. S. Gavin, and S. Gregory, "The anti-k t jet clustering algorithm," 2008.

[26] J. D. Jackson, H. E. Gove, and R. F. Schwitters, "Annual review of nuclear and particle science," *Ann. Rev. Nucl. Part. Sci.;(United States)*, vol. 34, 1984.

[27] P. Ade, N. Aghanim, M. Arnaud, M. Ashdown, J. Aumont, C. Baccigalupi, A. Banday, R. Barreiro, J. Bartlett, N. Bartolo, *et al.*, "Planck 2015 results-xxiv. cosmology from sunyaev-zeldovich cluster counts," *Astronomy & Astrophysics*, vol. 594, p. A24, 2016.

[28] J. F. Navarro, C. S. Frenk, and S. D. White, "A universal density profile from hierarchical clustering," *The Astrophysical Journal*, vol. 490, no. 2, p. 493, 1997.

[29] F. Zwicky, "Republication of: The redshift of extragalactic nebulae," *General Relativity and Gravitation*, vol. 41, no. 1, pp. 207–224, 2009.

[30] H. W. Babcock, "The rotation of the andromeda nebula," *Lick observatory bulletin*, vol. 19, pp. 41–51, 1939.

[31] V. C. Rubin and W. K. Ford Jr, "Rotation of the andromeda nebula from a spectroscopic survey of emission regions," *The Astrophysical Journal*, vol. 159, p. 379, 1970.

[32] A. Bosma, *The distribution and kinematics of neutral hydrogen in spiral galaxies of various morphological types*. PhD thesis, Rijksuniversiteit te Groningen., 1978.

[33] G. Steigman and M. S. Turner, "Cosmological constraints on the properties of weakly interacting massive particles," *Nuclear Physics B*, vol. 253, pp. 375–386, 1985.

[34] K. Griest, "The search for the dark matter: Wimps and machos," *arXiv preprint hep-ph/9303253*, 1993.

[35] E. W. Kolb and R. Slansky, "Dimensional reduction in the early universe: where have the massive particles gone?," *Physics Letters B*, vol. 135, no. 5-6, pp. 378–382, 1984.

[36] J. L. Feng, "Dark matter candidates from particle physics and methods of detection," *Annual Review of Astronomy and Astrophysics*, vol. 48, pp. 495–545, 2010.

[37] L. Rinchiuso, E. Moulin, C. Armand, V. Poireau, and H. Collaboration, "Dark matter search with hess towards ultra-faint dwarf nearby des satellites of the milky way," *arXiv preprint arXiv:1908.04311*, 2019.

[38] V. A. Acciari, S. Ansoldi, L. Antonelli, A. A. Engels, D. Baack, A. Babić, B. Banerjee, U. B. de Almeida, J. Barrio, J. B. González, *et al.*, "A search for dark matter in triangulum ii with the magic telescopes," *Physics of the Dark Universe*, vol. 28, p. 100529, 2020.

[39] M. Jeong, "A search for neutrinos from decaying dark matter in galaxy clusters and galaxies with icecube," *arXiv preprint arXiv:2107.11527*, 2021.

[40] V. Barinov, B. Cleveland, S. Danshin, H. Ejiri, S. Elliott, D. Frekers, V. Gavrin, V. Gorbachev, D. Gorbunov, W. Haxton, *et al.*, "Results from the baksan experiment on sterile transitions (best)," *Physical Review Letters*, vol. 128, no. 23, p. 232501, 2022.

[41] A. Albert, M. André, M. Anghinolfi, G. Anton, M. Ardid, J.-J. Aubert, J. Aublin, B. Baret, S. Basa, B. Belhorma, *et al.*, "Search for dark matter towards the galactic centre with 11 years of antares data," *Physics Letters B*, vol. 805, p. 135439, 2020.

[42] A. Neronov, D. Malyshev, and D. Eckert, "Decaying dark matter search with nustar deep sky observations," *Physical Review D*, vol. 94, no. 12, p. 123504, 2016.

[43] N. Sekiya, N. Y. Yamasaki, and K. Mitsuda, "A search for a kev signature of radiatively decaying dark matter with suzaku xis observations of the x-ray diffuse background," *Publications of the Astronomical Society of Japan*, vol. 68, no. SP1, 2016.

[44] A. Abeysekara, A. Albert, R. Alfaro, C. Alvarez, R. Arceo, J. Arteaga-Velázquez, D. A. Rojas, H. A. Solares, A. Becerril, E. Belmont-Moreno, *et al.*, "A search for dark matter in the galactic halo with hawc," *Journal of Cosmology and Astroparticle Physics*, vol. 2018, no. 02, p. 049, 2018.

[45] M. Aguilar, L. A. Cavasonza, G. Ambrosi, L. Arruda, N. Attig, F. Barao, L. Barrin, A. Bartoloni, S. Başeğmez-du Pree, J. Bates, *et al.*, "The alpha magnetic spectrometer (ams) on the international space station: Part ii—results from the first seven years," *Physics reports*, vol. 894, pp. 1–116, 2021.

[46] K. N. Abazajian, S. Horiuchi, M. Kaplinghat, R. E. Keeley, and O. Macias, "Strong constraints on thermal relic dark matter from fermi-lat observations of the galactic center," *Physical Review D*, vol. 102, no. 4, p. 043012, 2020.

[47] R. K. Leane, T. R. Slatyer, J. F. Beacom, and K. C. Ng, "Gev-scale thermal wimps: Not even slightly ruled out," *Physical Review D*, vol. 98, no. 2, p. 023016, 2018.

[48] G. Angloher, M. Bauer, I. Bavykina, A. Bento, A. Brown, C. Bucci, C. Ciemniak, C. Coppi, G. Deuter, F. von Feilitzsch, *et al.*, "Cresst," *EAS Publications Series*, vol. 36, pp. 231–236, 2009.

[49] E. Aprile, J. Angle, F. Arneodo, L. Baudis, A. Bernstein, A. Bolozdynya, P. Brusov, L. Coelho, C. Dahl, L. DeViveiros, *et al.*, "Design and performance of the xenon10 dark matter experiment," *Astroparticle Physics*, vol. 34, no. 9, pp. 679–698, 2011.

[50] E. Aprile, K. Arisaka, F. Arneodo, A. Askin, L. Baudis, A. Behrens, E. Brown, J. Cardoso, B. Choi, D. Cline, *et al.*, "The xenon100 dark matter experiment," *Astroparticle Physics*, vol. 35, no. 9, pp. 573–590, 2012.

[51] S. Baum, K. Freese, and C. Kelso, "Dark matter implications of dama/libra-phase2 results," *Physics Letters B*, vol. 789, pp. 262–269, 2019.

[52] J. Schieck, G. Angloher, A. Bento, C. Bucci, L. Canonica, X. Defay, A. Erb, N. F. Iachellini, P. Gorla, A. Guetlein, *et al.*, "Direct dark matter search with the cresst ii experiment," *arXiv preprint arXiv:1611.02113*, 2016.

[53] A. Boveia and C. Doglioni, "Dark matter searches at colliders," *arXiv preprint arXiv:1810.12238*, 2018.

[54] M. Fabbrichesi, E. Gabrielli, and G. Lanfranchi, *The Physics of the Dark Photon: A Primer*. Springer, 2021.

[55] R. Essig, J. A. Jaros, W. Wester, P. H. Adrian, S. Andreas, T. Averett, O. Baker, B. Batell, M. Battaglieri, J. Beacham, *et al.*, "Dark sectors and new, light, weakly-coupled particles," *arXiv preprint arXiv:1311.0029*, 2013.

[56] A. Filippi and M. De Napoli, "Searching in the dark: the hunt for the dark photon," *Reviews in Physics*, vol. 5, p. 100042, 2020.

[57] C. Ahdida, A. Akmete, R. Albanese, A. Alexandrov, A. Anokhina, S. Aoki, G. Arduini, E. Atkin, N. Azorskiy, J. Back, *et al.*, "Sensitivity of the ship experiment to dark photons decaying to a pair of charged particles," *The European Physical Journal C*, vol. 81, no. 5, pp. 1–17, 2021.

[58] Y. S. Tsai, "Axion bremsstrahlung by an electron beam," *Physical Review D*, vol. 34, no. 5, p. 1326, 1986.

[59] S. S. Chakrabarty and I. Jaeglé, "Search for dark photon, axion-like particles, dark scalar, or light dark matter in compton-like processes," *arXiv preprint arXiv:1903.06225*, 2019.

[60] M. Raggi and V. Kozhuharov, "Results and perspectives in dark photon physics," *La Rivista del Nuovo Cimento*, vol. 38, no. 10, pp. 449–505, 2015.

[61] M. Graham, C. Hearty, and M. Williams, "Searches for dark photons at accelerators," *arXiv preprint arXiv:2104.10280*, 2021.

[62] M. Pospelov and A. Ritz, "Astrophysical signatures of secluded dark matter," *Physics Letters B*, vol. 671, no. 3, pp. 391–397, 2009.

[63] K. du Plessis, M. Flores, D. Kar, S. Sinha, and H. van der Schyf, "Hitting two bsm particles with one lepton-jet: search for a top partner decaying to a dark photon, resulting in a lepton-jet," *SciPost Physics*, vol. 13, no. 2, p. 018, 2022.

[64] J. H. Kim and I. M. Lewis, "Loop induced single top partner production and decay at the lhc," *Journal of High Energy Physics*, vol. 2018, no. 5, pp. 1–56, 2018.

[65] C. Cheung, J. T. Ruderman, L.-T. Wang, and I. Yavin, "Lepton jets in (supersymmetric) electroweak processes," *Journal of High Energy Physics*, vol. 2010, no. 4, pp. 1–23, 2010.

[66] A. Falkowski, J. T. Ruderman, T. Volansky, and J. Zupan, "Hidden higgs decaying to lepton jets," *Journal of High Energy Physics*, vol. 2010, no. 5, pp. 1–39, 2010.

[67] T. Sjöstrand, S. Ask, J. R. Christiansen, R. Corke, N. Desai, P. Ilten, S. Mrenna, S. Prestel, C. O. Rasmussen, and P. Z. Skands, "An introduction to pythia 8.2," *Computer physics communications*, vol. 191, pp. 159–177, 2015.

[68] R. D. Ball, V. Bertone, S. Carrazza, L. Del Debbio, S. Forte, A. Guffanti, N. P. Hartland, J. Rojo, N. Collaboration, *et al.*, "Parton distributions with qed corrections," *Nuclear Physics B*, vol. 877, no. 2, pp. 290–320, 2013.

[69] A. Alloul, N. D. Christensen, C. Degrande, C. Duhr, and B. Fuks, "Feynrules 2.0—a complete toolbox for tree-level phenomenology," *Computer Physics Communications*, vol. 185, no. 8, pp. 2250–2300, 2014.

[70] C. Bierlich, A. Buckley, J. Butterworth, C. H. Christensen, L. Corpe, D. Grellscheid, J. F. Grosse-Oetringhaus, C. Gutschow, P. Karczmarczyk, J. Klein, *et al.*, "Robust independent validation of experiment and theory: Rivet version 3," *SciPost physics*, vol. 8, no. 2, p. 026, 2020.

[71] J. Thaler and K. Van Tilburg, "Identifying boosted objects with n-subjettiness," *Journal of High Energy Physics*, vol. 2011, no. 3, pp. 1–28, 2011.

[72] J. Thaler and K. Van Tilburg, "Maximizing boosted top identification by minimizing n-subjettiness," *Journal of High Energy Physics*, vol. 2012, no. 2, pp. 1–33, 2012.

[73] M. Jankowiak and A. J. Larkoski, "Angular scaling in jets," *Journal of High Energy Physics*, vol. 2012, no. 4, pp. 1–21, 2012.

[74] A. J. Larkoski, G. P. Salam, and J. Thaler, "Energy correlation functions for jet substructure," *Journal of High Energy Physics*, vol. 2013, no. 6, pp. 1–43, 2013.

[75] A. J. Larkoski, I. Moult, and D. Neill, "Power counting to better jet observables," *Journal of High Energy Physics*, vol. 2014, no. 12, pp. 1–41, 2014.

[76] A. J. Larkoski, J. Thaler, and W. J. Waalewijn, "Gaining (mutual) information about quark/gluon discrimination," *Journal of High Energy Physics*, vol. 2014, no. 11, pp. 1–56, 2014.

[77] P. Gras, S. Höche, D. Kar, A. Larkoski, L. Lönnblad, S. Plätzer, A. Siódmok, P. Skands, G. Soyez, and J. Thaler, "Systematics of quark/gluon tagging," *Journal of High Energy Physics*, vol. 2017, no. 7, pp. 1–50, 2017.

[78] Atlas Collaboration , "Electron efficiency measurements with the atlas detector using 2012 lhc proton-proton collision data," *arXiv preprint arXiv:1612.01456*, 2016.

[79] G. J. Feldman and R. D. Cousins, "Unified approach to the classical statistical analysis of small signals," *Physical review D*, vol. 57, no. 7, p. 3873, 1998.

[80] K. Petraki and R. R. Volkas, "Review of asymmetric dark matter," *International Journal of Modern Physics A*, vol. 28, no. 19, p. 1330028, 2013.

[81] Y. Bai and P. Schwaller, "Scale of dark qcd," *Physical Review D*, vol. 89, no. 6, p. 063522, 2014.

[82] H. Beauchesne, E. Bertuzzo, and G. Grilli di Cortona, "Dark matter in hidden valley models with stable and unstable light dark mesons," *Journal of High Energy Physics*, vol. 2019, no. 4, pp. 1–24, 2019.

[83] B. Patt and F. Wilczek, "Higgs-field portal into hidden sectors," *arXiv preprint hep-ph/0605188*, 2006.

[84] A. Falkowski, J. Juknevich, and J. Shelton, "Dark matter through the neutrino portal," *arXiv preprint arXiv:0908.1790*, 2009.

[85] B. Holdom, "Two u (1)'s and epsilon charge shifts," *Phys. Lett., B*, vol. 166, no. 2, pp. 196–198, 1986.

[86] G. Albouy, J. Barron, H. Beauchesne, E. Bernreuther, M. Bona, C. Cazzaniga, C. Cesarotti, T. Cohen, A. de Cosa, D. Curtin, *et al.*, "Theory, phenomenology, and experimental avenues for dark showers: a snowmass 2021 report," *arXiv preprint arXiv:2203.09503*, 2022.

[87] CMS collaboration, "Search for resonant production of strongly coupled dark matter in proton-proton collisions at 13 tev," *arXiv preprint arXiv:2112.11125*, 2021.

[88] T. Cohen, M. Lisanti, H. K. Lou, and S. Mishra-Sharma, "Lhc searches for dark sector showers," *Journal of High Energy Physics*, vol. 2017, no. 11, pp. 1–32, 2017.

[89] T. Cohen, M. Lisanti, and H. K. Lou, "Semivisible jets: dark matter undercover at the lhc," *Physical review letters*, vol. 115, no. 17, p. 171804, 2015.

[90] M. J. Strassler and K. M. Zurek, "Echoes of a hidden valley at hadron colliders," *Physics Letters B*, vol. 651, no. 5-6, pp. 374–379, 2007.

[91] D. Kar and S. Sinha, "Exploring jet substructure in semi-visible jets," *SciPost Physics*, vol. 10, no. 4, p. 084, 2021.

[92] CMS Collaboration, "Search for high mass dijet resonances with a new background prediction method in proton-proton collisions at s = 13 tev," *Journal of High Energy Physics*, vol. 2020, no. 5, pp. 1–45, 2020.

[93] J. Alimena, J. Beacham, M. Borsato, Y. Cheng, X. C. Vidal, G. Cottin, D. Curtin, A. De Roeck, N. Desai, J. A. Evans, *et al.*, "Searching for long-lived particles beyond the standard model at the large hadron collider," *Journal of Physics G: Nuclear and Particle Physics*, vol. 47, no. 9, p. 090501, 2020.

[94] M. J. Strassler, "Possible effects of a hidden valley on supersymmetric phenomenology," *arXiv preprint hep-ph/0607160*, 2006.

[95] T. Han, Z. Si, K. M. Zurek, and M. J. Strassler, "Phenomenology of hidden valleys at hadron colliders," *Journal of High Energy Physics*, vol. 2008, no. 07, p. 008, 2008.

[96] L. Carloni and T. Sjöstrand, "Visible effects of invisible hidden valley radiation," *Journal of High Energy Physics*, vol. 2010, no. 9, pp. 1–31, 2010.

[97] M. Svensson Seth, "A first study of hidden valley models at the lhc," 2011.

[98] A. Alves, S. Profumo, and F. S. Queiroz, "The dark z portal: direct, indirect and collider searches," *Journal of High Energy Physics*, vol. 2014, no. 4, pp. 1–29, 2014.

[99] ATLAS Collaboration, "The atlas experiment at the cern large hadron collider," *Journal of instrumentation*, vol. 3, no. S08003, 2008.

[100] ATLAS Collaboration, "Atlas insertable b-layer technical design report," tech. rep., ATLAS-TDR-019, 2010.

[101] ATLAS Collaboration, "Production and integration of the atlas insertable b-layer," *Journal of instrumentation*, vol. 13, no. 05, p. T05008, 2018.

[102] ATLAS collaboration, "The atlas collaboration software and firmware," tech. rep., ATL-SOFT-PUB-2021-001, 2021.

[103] J. Alwall, R. Frederix, S. Frixione, V. Hirschi, F. Maltoni, O. Mattelaer, H.-S. Shao, T. Stelzer, P. Torrielli, and M. Zaro, "The automated computation of tree-level and next-to-leading order differential cross sections, and their matching to parton shower simulations," *Journal of High Energy Physics*, vol. 2014, no. 7, pp. 1–157, 2014.

[104] J. Shelton, "Tasi lectures on jet substructure," *arXiv preprint arXiv:1302.0260*, 2013.

[105] H. Abramowicz, U. Acosta, M. Altarelli, R. Assmann, Z. Bai, T. Behnke, Y. Benhammou, T. Blackburn, S. Boogert, O. Borysov, *et al.*, "Conceptual design report for the luxe experiment," *The European Physical Journal Special Topics*, vol. 230, no. 11, pp. 2445–2560, 2021.

[106] F. Bloch, W. Hansen, and M. Packard, "Nuclear induction experiments\\phys," 1946.

[107] L. Funcke, T. Hartung, B. Heinemann, K. Jansen, A. Kropf, S. Kühn, F. Meloni, D. Spataro, C. Tüysüz, and Y. C. Yap, "Studying quantum algorithms for particle track reconstruction in the luxe experiment," *arXiv preprint arXiv:2202.06874*, 2022.

[108] J. Tilly, H. Chen, S. Cao, D. Picozzi, K. Setia, Y. Li, E. Grant, L. Wossnig, I. Rungger, G. H. Booth, *et al.*, "The variational quantum eigensolver: a review of methods and best practices," *Physics Reports*, vol. 986, pp. 1–128, 2022.

[109] "The variational quantum eigensolver (vqe)." http://openqemist.1qbit.com/docs/vqe. Accessed: 2022-09-05.

[110] "qiskit circuit library twolocal." https://qiskit.org/qiskit.circuit.library.TwoLocal.html. Accessed: 2022-09-05.

[111] "qiskit circuit library rygate." https://qiskit.org/qiskit.circuit.library.RYGate.html. Accessed: 2022-09-05.